Continuous wave Doppler-free spectroscopy on the $A\,^2\Sigma^+ \leftarrow X\,^2\Pi_{3/2}$ transition in thermal nitric oxide

Von der Fakultät Mathematik und Physik der Universität Stuttgart
zur Erlangung der Würde eines Doktors der Naturwissenschaften
(Dr. rer. nat.) genehmigte Abhandlung

vorgelegt von

Patrick Kaspar

aus Böblingen

Hauptberichter:	Prof. Dr. Tilman Pfau
Mitberichter:	Prof. Dr. Peter Michler
Prüfungsvorsitzender:	Prof. Dr. Hans-Peter Büchler
Tag der mündlichen Prüfung:	6. Dezember 2022

5. Physikalisches Institut
Universität Stuttgart
2022

It was my choice or chance or curse
To adopt the cause for better or worse
And with my worldly goods & wit
And soul & and body worship it.

(Edgar Allan Poe, “To Isaac Lea”)

Ehrenwörtliche Erklärung

Schriftliche Bestätigung der eigenständig erbrachten Leistung gemäß §6 Absatz 2 der Promotionsordnung der Universität Stuttgart

Die eingereichte Dissertation zum Thema

Continuous wave Doppler-free spectroscopy on the $A^2\Sigma^+ \leftarrow X^2\Pi_{3/2}$ transition in thermal nitric oxide

stellt meine eigenständig erbrachte Leistung dar.

Ich habe ausschließlich die angegebenen Quellen und Hilfsmittel benutzt. Wörtlich oder inhaltlich aus anderen Werken übernommene Angaben habe ich als solche kenntlich gemacht.

Die Richtigkeit der hier getätigten Angaben bestätige ich und versichere, nach bestem Wissen die Wahrheit erklärt zu haben.

Stuttgart den, ...

(Datum)

....

(Unterschrift Doktorand)

Erklärung zur Übereinstimmung der digitalen Version mit der vorgelegten Printversion der Dissertation

Hiermit erkläre ich, ... (Name, Vorname).

geboren am ....,

dass das von mir eingereichte pdf-Dokument zur Dissertation

mit dem Thema

Continuous wave Doppler-free spectroscopy on the $A^2\Sigma^+ \leftarrow X^2\Pi_{3/2}$ transition in thermal nitric oxide

in Inhalt und Wortlaut der ebenfalls eingereichten Printversion meiner Dissertationsschrift entspricht.

Stuttgart den, ...

(Datum)

....

(Unterschrift Doktorand)

Zusammenfassung

Im Rahmen dieser Arbeit wurde Dopplerfreie Sättigungsspektroskopie in Stickstoffmonoxid am $A\,^2\Sigma^+ \leftarrow X\,^2\Pi_{3/2}$ Übergang realisiert. Dieses hochauflösende Spektroskopieverfahren ermöglicht die direkte Auflösung von sogenannten “Lamb-dips”. Dies ist gleichbedeutend mit der direkten Auflösung der Hyperfeinstruktur des Moleküls. Der Frequenzabstand zwischen einzelnen Hyperfeinübergängen wurde ermittelt und ermöglichte hierdurch die Bestimmung der Hyperfeinkonstanten des $A\,^2\Sigma^+$ Zustandes von Stickstoffmonoxid. Der Vergleich der neu bestimmten Konstanten mit zuvor mit anderen spektroskopischen Techniken bestimmten Konstanten zeigt hervorragende Übereinstimmung. Des Weiteren wird die Rydberganregung von Stickstoffmonoxid mit einem dreiphotonigen Anregungsschema erläutert. Diese ist Kernbestandteil der Entwicklung eines Laborprototyps zur Erprobung eines neuartigen Sensorprinzips zum Nachweis von Stickstoffmonoxid.

In dieser Arbeit werden zu Beginn die theoretischen Grundlagen, die für das Verständnis der weiteren Arbeit notwendig sind, eingeführt. Dies umfasst die Beschreibung der Energiestruktur von zweiatomigen Molekülen. Diese kann in einen elektronischen Anteil sowie die Vibrations- und Rotationsenergien aufgeteilt werden. Im Anschluss daran werden die verschiedenen Kopplungsfälle für die Drehimpulse innerhalb des Moleküls behandelt. Hier beschränkt sich die Arbeit auf die relevanten drei Fälle, die als Hund’sche Fälle (a), (b) und (d) bezeichnet werden. Es folgt darauf eine kurze Einführung zur Parität molekularer Zustände in zweiatomigen Molekülen sowie ein Überblick über die verschiedenen Auswahlregeln für Dipolübergänge innerhalb des Moleküls. Die Beschreibung der eingangs erwähnten Hyperfeinstruktur erfolgt mittels eines effektiven Hamiltonoperators (effective Hamiltonian). Dieses Konzept wird zunächst kurz erläutert bevor dann die zugehörigen Matrixelemente für Fein- und Hyperfeinstruktur aufgeführt werden. Die theoretische Einführung endet mit einem kurzen Abschnitt zu Rydbergzuständen.

Als Nächstes wird das drei Photonen umfassende Anregungsschema für die Rydberganregung von Stickstoffmonoxid vorgestellt. Es basiert auf drei Übergängen. Zunächst werden die Atome vom $\mathrm{X}\,^2\Pi_{3/2}$ Zustand zum $\mathrm{A}\,^2\Sigma^+$ Zustand angeregt. Hierzu wird Licht mit einer Wellenlänge von 226 nm verwendet. Der nächste Übergang benötigt Licht bei 540 nm und regt den $\mathrm{H}\,^2\Sigma^+$ Zustand des Moleküls an. Von dort aus sind mit Wellenlängen zwischen 833 nm und 835 nm viele unterschiedliche Rydbergzustände erreichbar. Die detaillierte Struktur der Zustände $\mathrm{X}\,^2\Pi$, $\mathrm{A}\,^2\Sigma^+$ und $\mathrm{H}\,^2\Sigma^+$ wird daraufhin diskutiert. Anschließend folgt die Einführung der beiden verwendeten Spektroskopietechniken. Zunächst wird die optogalvanische Spektroskopie eingeführt. Diese Technik kann in drei Schritten erklärt werden. Als Erstes wird mit schmalbandigen Lasern nach dem vorgestellten dreiphotonigen Anregungsschema Stickstoffmonoxid in Rydbergzustände angeregt. Im zweiten Schritt sorgen Stöße der angeregten Moleküle mit einem Hintergrundgas, wie zum Beispiel Stickstoff, für die Ionisation der Rydbergmoleküle. Die dabei entstehenden freien Ladungen werden im dritten Schritt mittels einer Spannung, die an die sich in der Zelle befindlichen Elektroden angelegt wird, aus der Zelle abgezogen. Der resultierende Strom kann dann mittels eines Tranzimpedanzverstärkers verstärkt und in eine Spannung umgewandelt werden. Diese wird letztendlich gemessen. Darauffolgend wird Dopplerfreie Sättigungsspektroskopie erläutert. Diese Spektroskopiemethode basiert auf einer gegenläufigen Strahlkonfiguration. Dabei wird ein Laserstrahl mit Leistung nahe der Sättigungsintensität, der als “Pump” bezeichnet wird, gleichzeitig mit einem gegenläufigen zweiten Laserstrahl mit deutlich geringerer Leistung, der “Probe” genannt wird, durch das Medium geschickt. Der stärkere der beiden Laserstrahlen verringert dabei die Absorption des schwächeren Strahls, wenn beide Laser mit derselben Geschwindigkeitsklasse interagieren. Dies ermöglicht es, molekulare Übergänge aufzulösen, die sonst im Dopplerverbreiterten Linienprofil verborgen blieben. Des Weiteren werden im Zuge dieser Einführung sowohl “Crossover-Resonanzen” als auch verschiedene Verbreiterungsmechanismen kurz diskutiert.

Der Mittelteil der Arbeit ist technischer Natur. Hier werden zunächst kurz die verwendeten Lasersysteme beschrieben. Außerdem wird schematisch erklärt, wie diese mittels “Transfer-Cavities” und dem Pound-Drever-Hall Verfahren frequenzstabilisiert werden. Des Weiteren wird das im Rahmen dieser Arbeit entwickelte Gasmischsystem vorgestellt. Hierzu werden zunächst einige theoretische Konzepte in

Bezug auf die Berechnungen von Gasflüssen eingeführt. Diese waren für die Auslegung des Systems von Bedeutung. Im Anschluss werden Sicherheitsaspekte und die einzelnen Komponenten des Setups diskutiert. Die Mischanlage verwendet vier Massedurchflussregler, um Stickstoffmonoxid und Stickstoff miteinander zu mischen.

Im letzten Drittel dieser Arbeit werden die spektroskopischen Ergebnisse diskutiert. Zunächst wird der Messaufbau der optogalvanischen Spektroskopie erläutert. Es werden einzelne Spektren qualitativ diskutiert, die die gelungene Rydberganregung von Stickstoffmonoxid mittels des vorgestellten Anregungspfades belegen. Der Fokus dieses Teils der Arbeit liegt jedoch auf spektroskopischen Resultaten, die Mittels Dopplerfreier Sättigungsspektroskopie erzielt wurden. Hierzu wird zunächst der zugehörige Spektroskopieaufbau eingeführt und erläutert. Daran schließt sich ein Abschnitt an, der sich mit der Optimierung des entsprechenden Signals beschäftigt. Nachfolgend erfolgt die Diskussion der Hyperfeinspektren, die für verschiedene Gesamtdrehimpulsquantenzahlen J_X des Grundzustands, für den $\mathrm{P}_{12\mathrm{ee}}$ Zweig des Spektrums zwischen den Zuständen $\mathrm{X}\,^2\Pi_{3/2}$ und $\mathrm{A}\,^2\Sigma^+$ gemessen wurden. Im Zuge der Diskussion werden die Übergänge in den Spektren als $\Delta F = -1$ Übergänge identifiziert. Die Frequenzabstände zwischen den einzelnen Übergängen werden mittels eines Fits bestimmt und mit theoretischen Berechnungen verglichen, die mit der Software PGOPHER gemacht wurden. Mittels der Frequenzabstände werden dann im Anschluss die Hyperfeinkonstanten des $\mathrm{A}\,^2\Sigma^+$ Zustandes neu bestimmt und mit früheren Ergebnissen verglichen. Nachfolgend daran findet eine qualitative Diskussion eines Spektrums statt, welches bei einem um zwei Größenordnungen niedrigeren Druck gemessen wurde. Die darin auftretenden zusätzlichen Linien werden als “Crossover-Resonanzen” interpretiert. Jedoch stellt sich heraus, dass diese Interpretation der Daten nicht vollständig durch theoretische Berechnungen gestützt wird. Weitere Daten sind notwendig, um die korrekte Interpretation des Spektrums zu bewerkstelligen. Im letzten Teil der Diskussion wird auf die Linienbreiten der verschiedenen gemessenen Spektren eingegangen. Hier wird deutlich, dass eine weitere Verbesserung der Kontrolle über die Messparameter notwendig ist, um konkretere Aussagen über das Verhalten der Spektren zu machen. Im Anschluss werden mögliche weitere Messungen erläutert, die genaueren Einblick in die Eigenschaften der untersuchten Zustände geben könnten.

Die Arbeit endet mit einem Ausblick, der sowohl das Potential der Dopplerfreien Sättigungsspektroskopie an Molekülen als auch die Möglichkeiten zur Verbesserung des Spektroskopieaufbaus und des Gassensorprototyps beleuchtet.

Abstract

Within the scope of this thesis the realisation of Doppler-free saturated absorption spectroscopy for the $A\,^2\Sigma^+ \leftarrow X\,^2\Pi_{3/2}$ transition in a thermal gas of nitric oxide was achieved. This high resolution spectroscopy technique enables the direct resolution of Lamb-dip spectra, i.e. the direct observation of the hyperfine structure of the molecule. The frequency splitting between individual hyperfine spectra was measured and allowed the determination of hyperfine constants of the $A\,^2\Sigma^+$ state of nitric oxide [1]. The comparison of the newly determined constants to values previously measured with different spectroscopic techniques, shows excellent agreement. In addition, the Rydberg excitation of nitric oxide with a three photon excitation scheme is presented. This is an essential part in the course of the development of a laboratory prototype for the investigation of a new kind of gas sensing scheme for nitric oxide.

In the beginning of this thesis a theoretical introduction to the energy structure of diatomic molecules is given. This comprises the electronic, vibrational and rotational energies. The different angular momentum coupling cases also denoted as Hund's cases are explained, followed by summaries concerning parity and dipole transition rules. The description of the aforementioned hyperfine structure of the molecules employs the effective Hamiltonian approach. The approach is briefly introduced and the corresponding matrix elements for fine and hyperfine structure of the molecule are given. It follows a very brief introduction of Rydberg states.

Next, the aforementioned excitation scheme is explained. It employs three transitions starting from the $X\,^2\Pi_{3/2}$ state the molecules are excited to the $A\,^2\Sigma^+$ state with light at a wavelength around 226 nm. The second transition is at 540 nm and excites the molecules to the $H\,^2\Sigma^+$ state. From there several different Rydberg states are addressable with wavelength between 833 - 835 nm. The energy structure of the

$\mathrm{X}\,^2\Pi$, $\mathrm{A}\,^2\Sigma^+$ and $\mathrm{H}\,^2\Sigma^+$ state are discussed in detail. This is followed by the introduction of optogalvanic spectroscopy. This technique can be explained in three steps. First, the aforementioned narrowband laser excitation to high Rydberg states takes place. Second, collisions between the Rydberg molecules and the background gas lead to ionisation of the Rydberg molecules. During the third and last step, the generated charges are detected by applying a small voltage to the onboard electrodes of the cell. In addition, an introduction to Doppler-free absorption spectroscopy is given. This technique is based on a counter-propagating beam configuration where a strong laser beam denoted as pump beam reduces the absorption of a weaker laser beam called probe beam, if both beams interact with the same velocity class. This enables the resolution of the molecular energy structure that is otherwise hidden within the Doppler-broadened line-profile.

The middle part of the thesis is very technical. It comprises a short overview over the employed laser systems, their working principles and the frequency stabilisation setup that was employed as well as an overview about the gas mixing unit that was developed within the scope of this work. To understand the gas mixing unit the necessary theoretical concepts for gas flow calculations are given, before the respective setup is explained in detail. The discussion includes safety aspects and a description of the individual parts of the setup. The gas mixing unit employs four mass flow controllers to generate mixtures of nitrogen and nitric oxide with different concentration of nitric oxide

In the last part of the thesis the spectroscopic results are discussed. First, the optogalvanic spectroscopy setup is explained and exemplary datasets are discussed proving the Rydberg excitation of nitric oxide with the described three photon excitation scheme.

However, the main focus lies here on the spectroscopic results of the Doppler-free saturated absorption spectroscopy. The corresponding setup is introduced, followed by a section where the process of signal optimisation is stated. Then the Lamb-dip data for different total angular momenta J_X is discussed. Within the course of the discussion the different transitions are assigned to be $\Delta F = -1$ transitions and the splittings between them are determined via a fit. The retrieved splittings are compared to a theoretical calculation employing PGOPHER and subsequently used to determine new values for the hyperfine constants of the $\mathrm{A}\,^2\Sigma^+$ state by fitting the data

employing a wrapper program for PGOPHER. It follows a qualitative discussion of spectra taken at two orders of magnitude lower pressure, showing additional spectroscopic lines. The additional lines might be attributed to crossover resonances. However, the corresponding theory does not fully support this hypothesis. Thus, further data would be necessary to clarify the matter. The final part of the discussion deals with the linewidth of the hyperfine spectra and is followed by a short overview on how the spectroscopic resolution may potentially be further improved and which additional measurements on that transition could yield important information for the general enhancement of the gas sensor prototype.

Contents

Introduction

This theses was conducted within the scope of the development of a laboratory prototype for the optogalvanic detection of nitric oxide. However, this work mainly focuses on high resolution optical spectroscopy. To set this into perspective, first an overview about the historic development behind the underlying sensor principle is given.

The technique of optogalvanic spectroscopy is based on electrically contacted spectroscopy cells. They were originally developed for the work with alkali vapours, opening up new possibilities to manipulate Rydberg atoms with electrical fields [2, 3]. In addition, the cell electrodes can not only be used to manipulate atoms inside the cell but also to read-out small electrical currents [4, 5]. These currents originate from the ionisation of the Rydberg atoms, i.e. they can be used to obtain information on the population of the Rydberg state [4]. If it is known how efficient the Rydberg state can be excited and how large the rate of ionisation is, it is possible to calculate the number of atoms in the ground state. Henceforth, the technique can be employed as a sensing scheme. This was further investigated in an idealised model system [6]. The basic principle of the sensing scheme is based on three steps. First, the atom or molecule in question is excited to a Rydberg state. Narrowband continuous wave lasers and a multi-photon excitation scheme ensure a high selectivity. Second, the weakly bound Rydberg atoms or molecules are then ionised by collisional ionisation with the background gas. Third, the generated charges are picked up by the cell electrodes and a current is measured [7, 8].

The feasibility of this concept was studied in [9, 10], setting it into perspective to other currently employed sensing techniques. Instead of alkali atoms nitric oxide was detected. In contrast to them nitric oxide is an important molecule in the human body. The 1998 nobel price in medicine was awarded to Furchgott, Ignarro and

Murad for their "discoveries concerning nitric oxide as a signalling molecule in the cardiovascular system" [11]. They were able to identify nitric oxide to be responsible for the process of vasodilation in the human body [12–14]. In addition, nitric oxide regulates neurotransmission and the immune function of macrophages [15, 16]. Furthermore, it acts as a signalling molecule indicating inflammatory diseases like cancer [17, 18] and asthma [19, 20]. Recently an extensive review on this field was published by Lundberg and Weitzberg [21]. Consequently, the efficient detection of nitric oxide in breath gas samples is of high interest in medical research and diagnostics.

Optogalvanic spectroscopy requires only small amounts of gas, since millilitre cell volumes are easy to realise and can achieve a high bandwidth in the 100 kHz range. Narrowband continuous wave lasers ensure high selectivity by exploiting the uniqueness of the energy structure of the molecules.

The development of the respective laboratory prototype requires precise knowledge on the involved states. The two involved states $\mathrm{X}\,^2\Pi$ and $\mathrm{A}\,^2\Sigma^+$ were investigated quite thoroughly [22–28]. Also the hyperfine structure of the two states has been investigated with different spectroscopic techniques [29–36]. However, the corresponding Lamb-dips have never been resolved directly. The new state of the art narrowband UV-laser system enables the direct resolution of the Lamb-dips. The investigation of the $\mathrm{A}\,^2\Sigma^+ \leftarrow \mathrm{X}\,^2\Pi_{3/2}$ transition with Doppler-free saturated absorption spectroscopy, allows to determine if the transition can be saturated with the corresponding laser system. The gained knowledge improves the quantification and assessment of the aforementioned gas sensor prototype.

This thesis is split into six chapters. The first two chapters are mainly of theoretical nature. In chapter 1 the theoretical concepts necessary to describe the energy structure of diatomic molecules are introduced. In chapter 2 the excitation path used for the sensor prototype and the structure of the involved states are discussed. In addition, optogalvanic spectroscopy and Doppler-free absorption spectroscopy are introduced.

The middle part of the thesis is of technical character and starts with chapter 3. Here, an overview on the employed laser systems and their frequency stabilisation is given. It is followed by chapter 4, which deals with the required gas mixing unit and vacuum system to safely mix and handle nitric oxide and nitrogen. This system has been developed within the scope of this thesis. The chapter gives an overview on the different setup components and the theoretical considerations that were made before setting the system up.

In the final part of this thesis the focus lies on the spectroscopic results achieved with the two introduced spectroscopic techniques. Chapter 5 presents first data on the Rydberg excitation of nitric oxide with the new excitation scheme and narrowband laser setup as published in [8]. The data is discussed qualitatively. In chapter 6 the main spectroscopic results are presented. It starts with an introduction to the experimental setup. This is followed by a description on how to optimise the experimental parameters to increase the signal quality. Subsequently the data on the hyperfine structure is quantitatively evaluated as published in [1]. In the last two sections crossover resonances and the width of the spectroscopic lines are discussed. The chapter ends with a short outlook, discussing the potential of further investigations.

1 The energy structure of diatomic molecules

Introduction

The energy structure of single atoms is described by quantum mechanics and quantum electrodynamics [37]. The electrons move around the nucleus in distinct volumes, atomic orbitals, resulting from the absolute square of the electron wave functions. Molecules are formed by two or more atoms bound to each other by a chemical bond. The simplest class of molecules are diatomic, i.e. consist of only two atoms bound together. Since this thesis is focused on the spectroscopy of nitric oxide (NO), this chapter will only deal with the energetic structure of diatomic molecules.

First the different contributions to the energy structure of diatomic molecules will be discussed in section 1.1-1.3. To understand the finer details of the diatomic energy structure the different coupling schemes for the angular momenta within the molecule, called Hund's coupling cases, are discussed. In section 1.6 and section 1.7 parity and symmetry will be introduced and an overview about the types of electronic transitions and the dipole transition rules will be given. The chapter ends with the introduction of the effective Hamiltonian in section 1.8 and the discussion of the smallest energy terms corresponding to Λ-type doubling, spin-rotation coupling and the terms describing the hyperfine structure, i.e. the coupling to the nuclear spin. At the very end of the chapter a short introduction to Rydberg states is given.

1.1 Electronic energy structure

This discussion relies closely on the explanations given by Herzberg [38]. The total energy of a molecule depends on the potential and kinetic energy of the electrons as well as on the corresponding energies of the nuclei [38]. The energy of a specific electronic state is based on which of the molecular orbitals are occupied by electrons. Transitions of electrons between different molecular orbitals can be induced by dipole radiation. Compared to the vibrational and rotational levels, which will be explained in the following sections, electronic energy levels have a larger distance to each other. Electronic transitions are often observed at wavelengths of the visible part of the electromagnetic spectrum or at the adjacent near-infrared or ultraviolet part. Vibrational transitions are often observed in the infrared and rotational transitions are mostly in the microwave regime.

The Schrödinger equation for the energies E of a diatomic molecule is given by Herzberg [38]

$$\frac{1}{m_e}\sum_i \Delta_i\Psi + \sum_k \frac{1}{M_k}\Delta_k\Psi + \frac{2}{\hbar^2}(E-V)\Psi = 0. \tag{1.1}$$

Here Δ_i is the Laplace operator acting on electron i and Δ_k the Laplace operator acting on the nucleus k with mass M_k. All electrons have mass m_e. V is the respective potential and $\hbar$ the reduced Planck constant. The exact solution of equation 1.1 is difficult. However, one can use a product wave function

$$\Psi = \psi_e(x_i, y_i, z_i)\cdot\psi_n(x_k, y_k, z_k), \tag{1.2}$$

to approximate the exact solution [38]. Here $\psi_e(x_i, y_i, z_i)$ is the electronic wave function solving equation 1.3a which is the Schrödinger equation describing the electrons moving in the field of the fixed nuclei described by the potential V_e. The nuclear wave function $\psi_n(x_k, y_k, z_k)$ solves the Schrödinger equation 1.3b for the movement of the nuclei under the influence of the potential $E_e + V_n$. The potential energy of the nuclear motion $E_e + V_n$ depends on the solution of equation 1.3a and therefore on the internuclear distance r. Thus a stable electronic state does only exist if $E_e + V_n$ has a minimum. The corresponding energy of the potential minimum is the electronic energy T_e of the state. The minimum of the lowest electronic state (i.e. groundstate) is usually choosen as zero.

$$\sum_i \Delta_i \psi_e + \frac{2m_e}{\hbar}(E_e - V_e)\psi_e = 0, \tag{1.3a}$$

$$\sum_k \frac{1}{M_k}\Delta_k \psi_n + \frac{2}{\hbar^2}(E - (E_e + V_n))\psi_n = 0. \tag{1.3b}$$

That the separation of the nuclear and electronic motion is legitimate was shown by Born and Oppenheimer [39] and is often referred to as Born-Oppenheimer approximation.

1.2 Vibrational energy structure

The minimum of the potential energy of the nuclear motion appears at a certain equilibrium r_e of the internuclear distance r. The nuclei vibrate around the equilibrium distance. The vibrational energy levels are quantised and for every electronic state there exist usually several different vibrational states. The exact number of vibrational states depends on the width of the potential and on the respective energy spacing between the vibrational levels. Radiative transitions between vibrational states are of much lower energy than those between electronic states. They occur at infrared wavelengths, so that early spectroscopic investigations relied on thermal light sources like mercury-vapour lamps or Nernst-lamps [40]. Nowadays modern infrared light sources like quantum-cascade lasers can be employed[41].

The exact energy levels can be obtained from the Schrödinger equation 1.3b. However, the solvability of equation 1.3b depends strongly on the form of $E_e + V_n$ and is in most cases not strictly possible. Therefore, it is feasible to approximate the term $E_e + V_n$ with a potential $V(r)$ describing the oscillating movement of the nuclei. Of course, the first idea that arises is the quadratic potential of an harmonic oscillator. However, the harmonic oscillator potential is symmetric and yields equidistant energy levels. This is contradictory to experimental observations since a symmetric potential will not allow dissociation and cannot explain the shrinking energetic distance between single vibrational energy levels [42, 43]. Therefore, an anharmonic potential is necessary to appropriately describe the nuclear motion. A good empirical approximation for $V(\mathrm{R})$ is the Morse-Potential [40] which allows to solve equation 1.3b exactly. It is given by

$$V(\mathbf{R}) = \mathrm{D_e}\left[1 - \exp\left(-a_M(r - r_e)\right)\right]^2 . \tag{1.4}$$

Here, $\mathrm{D_e}$ is the dissociation energy and a_M a molecule specific constant. Figure 1.1 depicts a Morse Potential with its minimum at r_e. For $r < r_e$ the potential is very steep, taking into account the repulsive Coulomb potential between the two nuclei. For $r > r_e$ the potential asymptotically approaches the dissociation energy $\mathrm{D_e}$. This is the energy threshold above which the vibrational energy states form a continuum (grey shading), so that the molecule will separate into the individual atoms that once formed it. The dissociation energy is sometimes also denoted by $\mathrm{D_0}$ and given with respect to the lowest vibrational energy level $\mathrm{v} = 0$. The yellow lines indicate a few vibrational energy levels below the dissociation energy. For $r > r_e$ the vibrational energies can be calculated by solving equation 1.3b with $E_e + V_n \rightarrow V(r)$. The vibrational energies can then be expressed in dependence of the vibrational quantum number υ and several vibrational constants.

$$G(\upsilon) = \omega_e\left(\upsilon + \frac{1}{2}\right) - \omega_e x_e\left(\upsilon + \frac{1}{2}\right)^2 + \omega_e y_e\left(\upsilon + \frac{1}{2}\right)^3 \ldots \tag{1.5}$$

The vibrational constants w_e,$w_e x_e$ and $w_e y_e$ differ for each electronic state within a molecule. The equation is dominated by the term linear in $(\upsilon + 1/2)$. Terms of higher order act usually only as small corrections, since the respective vibrational constants are in most cases one or more orders of magnitude smaller than w_e.

1.3 Rotational energy structure

This section also follows the descriptions given in [38]. Molecules are not only able to vibrate but also to rotate in space. The energy of the rotation is an additional con-

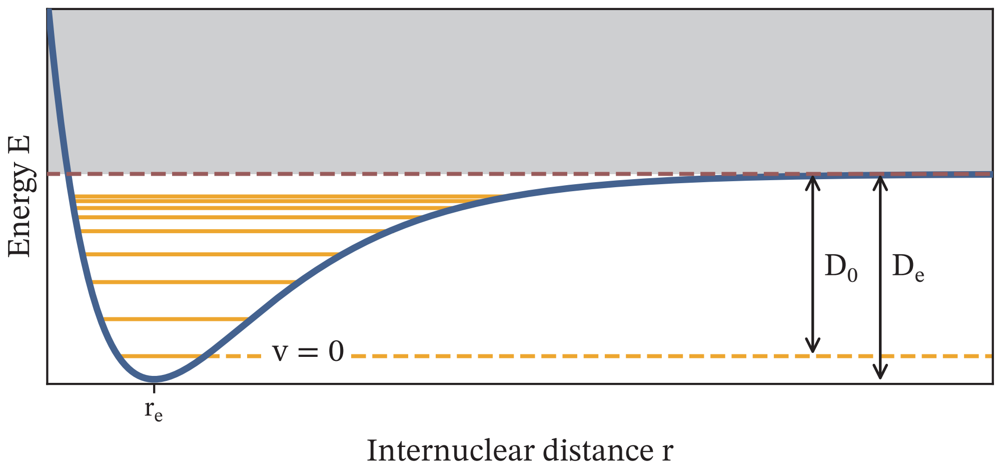

Figure 1.1: Morse potential with its minimum at the equilibrium internuclear distance r_e. D_e denotes the dissociation energy and D_0 the dissociation energy with respect to the lowest vibrational energy level, denoted as $v = 0$. Higher vibrational energy levels are indicated as yellow lines. Above the dissociation energy the grey shading represents the energetic continuum. After [40].

tribution to the total energy of the molecule. The spacing between single rotational energy levels is considerably smaller than between vibrational or electronic energy levels. Spectroscopic investigations of purely rotational transitions can therefore rely on microwave spectroscopy [44]. For the theoretical description of the rotation of diatomic molecules a number of different models exists. A detailed discussion of the different models is given for example in [38, 45] and is summarised in the following paragraph. It will end with an expression for the rotational energy based on the symmetric top model.

The simplest model is the rigid rotator where the two nuclei are considered to be connected by a rigid, massless rod. The rotational energy is given by

$$F(J) = \frac{h}{8\pi^2 c_0 I} J(J+1) = BJ(J+1). \tag{1.6}$$

Here, the rotational constant $B = h/(8\pi^2 c_0 I)$ given in cm^{-1} and the rotational quantum number J are introduced. The constant B depends on Planck's constant h, the speed of light c_0 and the moment of inertia perpendicular to the internuclear axis I. However, as already discussed in section 1.2 the nuclei vibrate periodically around an equilibrium distance r_e. Consequently, the assumption of a fully rigid connection between the nuclei is too simplified.

A better model is therefore the non-rigid rotator. Here, the massless rod is replaced by a massless spring, introducing centrifugal forces resulting from the rotation. These forces result in a correction term depending on the constant D_e (not to be confused with the dissociation energy $\mathrm{D_e}$) often referred to as centrifugal distortion constant. The rotational energy has then the form

$$F(J) = B_e J(J+1) - D_e J^2 (J+1)^2. \tag{1.7}$$

For the non-rigid rotator the vibrational and rotational movement are still treated independently of each other. The index e refers to the equilibrium distance r_e between the two nuclei. The respective constants are often called equilibrium constants.

Further refinement of the model leads to the vibrating rotator. Since the vibration of the nuclei changes the internuclear distance, the moment of inertia of the molecule changes alongside the vibrational motion. Henceforth the rotational energy and thus also the constant B of the molecule depend on its vibrational energy state. Since the vibrational motion is happening at a much higher frequency than the rotational motion it is justified to use a mean value $\bar{r}$ of the internuclear distance r for a each given vibrational energy level. As a consequence the rotational constant and also its higher order centrifugal correction are given in dependence of the vibrational level υ as B_υ, D_υ. They are related to the equilibrium constants B_e and D_e by a series expansion with the coefficients α_e, β_e and γ_e [45]

$$B_\upsilon = B_e - \alpha_e\left(\upsilon + \frac{1}{2}\right) + \gamma_e\left(\upsilon + \frac{1}{2}\right)^2 + \dots \tag{1.8}$$

$$D_\upsilon = D_e - \beta_e\left(\upsilon + \frac{1}{2}\right) + \dots \tag{1.9}$$

Here υ is the vibrational quantum number. The coefficients α_e, β_e and γ_e are determined empirically.

So far the electrons were completely neglected in the treatment of the rotational energy. Even though the mass of the electrons is very small compared to that of the nuclei it leads to a non-zero moment of inertia along the internuclear axis. The model of the symmetric top includes this very small moment of inertia. It was treated first by Reiche, Rademacher, Kronig and Rabi [46–48]. The electron cloud is considered to be rigid, ignoring the motion of the individual electrons. The total angular momentum of the rotation of the symmetric top $\mathbf{J}$ is no longer perpendicular to the internuclear axis. It's perpendicular component is denoted $\mathbf{N}$ and resembles the pure motion of the nuclei. The total angular momentum neglecting the electron spin, is then given by the sum of $\mathbf{N}$ and the angular momentum of the electrons along the internuclear axis $\mathbf{\Lambda}$ which is introduced within the scope of this model. Figure 1.2 illustrates the coupling of the vectors $\mathbf{N}$ and $\mathbf{\Lambda}$ to form $\mathbf{J}$. The reversal of the rotation of the electrons reverses also the direction of the vector $\mathbf{\Lambda}$. Therefore for each value of J two different modes of motion exist [38]. For the less refined models: the rigid, non-rigid and vibrating rotator $\mathbf{\Lambda}$ does not exist, thus in their case $\mathbf{J} = \mathbf{N}$.

The rotational energies for the symmetric top depend on the quantum number J and are given by

$$F(J) = B_\upsilon J(J+1) + (A_\Lambda - B_\upsilon)\Lambda^2 - D_\upsilon J^2(J+1)^2 + \dots \tag{1.10}$$

The constant A_Λ takes into account the moment of inertia parallel to the internuclear axis. It is defined in the same manor as the rotational constant to be $A_\Lambda = h/(8\pi^2 c_0 I_\mathrm{A})$. Since the moment of inertia perpendicular to the internuclear axis is

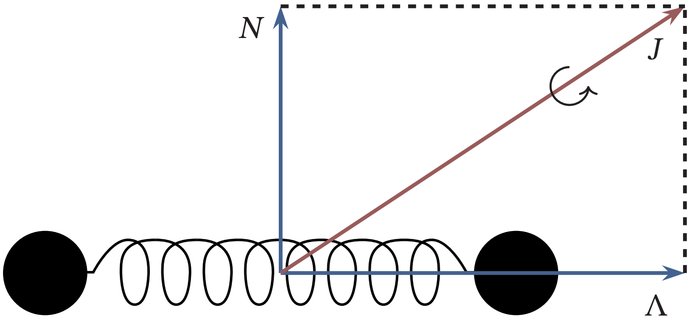

Figure 1.2: Schematic of the symmetric top. $\mathbf{\Lambda}$ is the orbital electron angular momentum along the internuclear axis. **N** resembles the motion of the pure nuclei and couples with $\mathbf{\Lambda}$ to **J**, the total angular momentum of the symmetric top. The whole diagram is rotating around **J** indicated by the curved arrow. After Herzberg [38].

much larger than the one along the axis, thus $I \gg I_A$ holds, the constant A_Λ is much larger than B_v.

For the interpretation of the spectra of very light molecules, like for example H_2, the interaction between vibration and rotation requires a more detailed treatment [45]. The corresponding theory was developed by Dunham [49] and Pekeris [50].

1.4 Thermal distribution of vibrational and rotational energy levels

In contrast to electronic states, where usually only the ground state is populated the population of the vibrational and rotational energy levels is distributed. Consequently, the spectroscopic strength of a transition is not only dependent on the transition moment but also on the population of molecules in the initial state.

The number of molecules N_υ in a particular vibrational state υ is given by [38]

$$N_\upsilon = \frac{N}{Q_\upsilon} \exp\left(\frac{-G_0(\upsilon)hc_0}{k_B T}\right). \tag{1.11}$$

Here, N is the total number of molecules, k_B the Boltzmann constant and T the temperature. Q_υ is the state sum of the vibrational levels which can be neglected when the exponential terms decrease rapidly [38], which is often the case. It is given by [38]

$$Q_\upsilon = 1 + \exp\left(\frac{-G_0(1)hc_0}{k_B T}\right) + \exp\left(\frac{-G_0(2)hc_0}{k_B T}\right) + \ldots \tag{1.12}$$

The energy term $G_0(\upsilon)hc_0$ is the vibrational energy referred to the zero-point energy of the potential when $G_0(\upsilon)$ is given in cm^{-1}. Its relation to the equilibrium constants can be found in [38]. Figure 1.3 shows the vibrational energy distribution for the ground state $\mathrm{X}\,^2\Pi$ (for the explanation of molecular term symbols see appendix B) of nitric oxide at 293 K and for comparison at 4400 K. The populations were calculated from the constants given in the appendix in table A.1. At room temperature

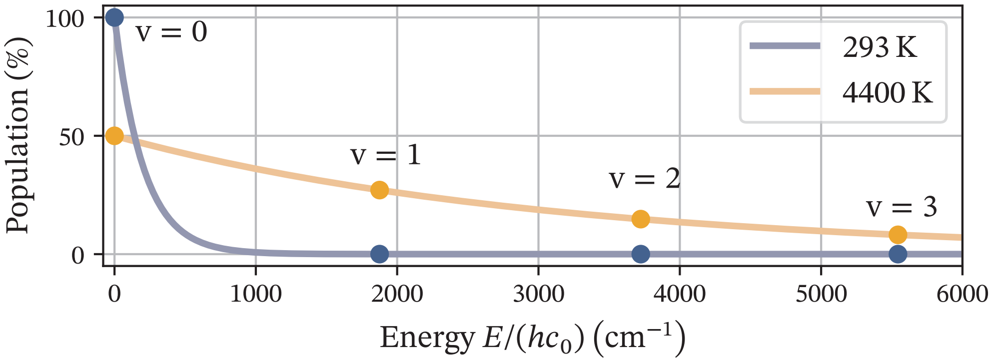

Figure 1.3: Population of the vibrational energy levels for $T = 293$ K and $T = 4400$ K of the ground state $\mathrm{X}\,^2\Pi$ of nitric oxide. The blue and orange dots mark the vibrational levels with quantum number $\upsilon = 0 - 3$. The lines act as a guides to the eye showing the population for continuous υ which of course is not physically correct.

almost all of the molecules are in the lowest vibrational state, the contribution of energy levels with $\upsilon > 0$ is negligibly small. Only at 4400 K the ratio between the number of molecules in the vibrational ground and excited states is equal, i.e. 50 % of the molecules are still in the ground state.

In case of the rotational levels the distribution is similar to that for the vibrational levels but the degeneracy of rotational levels has to be taken into account. For a total angular momentum J there are $2J + 1$ sublevels. These sublevels are energetically degenerate in the absence of external fields. The degeneracy results in an additional prefactor, so that the number of molecules N_J with total angular momentum J for the rotational constant B given in cm^{-1} is given by [38]

$$N_J = \frac{N}{Q_r}(2J + 1) \exp\left(\frac{-BJ(J + 1)hc}{k_B T}\right). \tag{1.13}$$

According to Herzberg [38] the state sum Q_r can be substituted by an integral, so that equation 1.13 simplifies to

$$N_J = N\frac{hcB}{k_B T}(2J + 1) \exp\left(\frac{-BJ(J + 1)hc}{k_B T}\right). \tag{1.14}$$

The rotational constant for the ground state of nitric oxide is given by $B = 1.696\,\mathrm{cm}^{-1}$ [35]. The resulting rotational energy distribution at 293 K is depicted in figure 1.4. The highest population is around 8 % in the $J = 15/2$ state. For comparison the distribution is plotted for 50 K and 1000 K too.

1.5 Coupling of angular Momenta: Hund's cases

The angular momenta in atoms and molecules couple to each other. This coupling defines the energy structure of a molecule or atom and is therefore essential for the understanding of the particular molecule or atom. For atoms there are two different coupling schemes: LS-coupling sometimes also called Russel-Saunders coupling and jj-coupling [37].

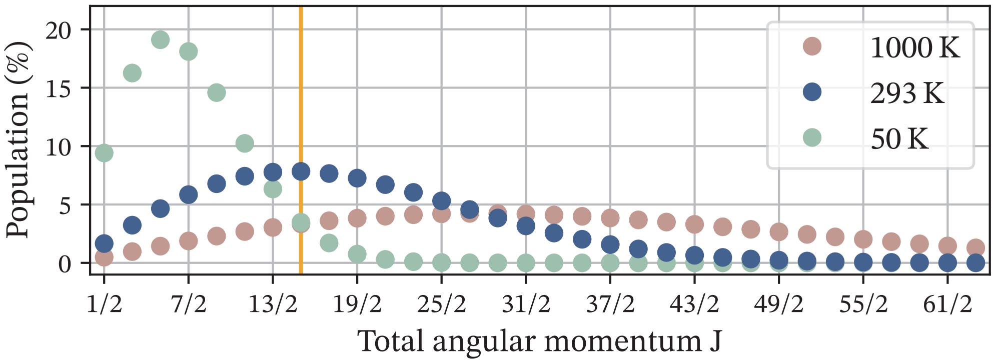

Figure 1.4: Population of the rotational energy levels in the ground state of NO calculated at different temperatures. At 293 K (room temperature) the highest population is in the $J = 15/2$ level, which is marked by the orange vertical line.

For molecules the situation is more complicated. In comparison to atoms, diatomic molecules are not spherical symmetric and possess more degrees of freedom. There are five distinct cases for the coupling of angular momenta in molecules. They are named Hund's cases after Friedrich Hund who also developed Hund's rules to determine the energetic ground state of atoms.

In this section Hund's cases (a) and (b) will be discussed in detail. These two cases are the most common in diatomic molecules. However, Hund's cases are idealised cases, thus they often do not fully fit the real physical situation. In fact for many states of diatomic molecules the coupling scheme is not purely given by case (a) and case (b) description, but by intermediate coupling between the two cases. A transition from Hund's case (a) to (b) occurs for example for the ground state of nitric oxide [27, 51].

Since case (d) is appropriate to describe most Rydberg states it will be mentioned briefly. Case (c) and (e) are not relevant for the description of nitric oxide and will be omitted. The discussion follows [45].

1.5.1 Hund's case (a)

The Hund's case (a) description is usually appropriate when the spin-orbit energy depending on the spin-orbit constant A is significantly larger than the rotational energy, i.e. $A\Lambda \gg BJ$.

The coupling scheme for Hund's case (a) is illustrated in figure 1.5. Electrostatic forces couple the orbital angular momentum **L** to the internuclear axis. The total electron spin **S** is coupled strongly to **L**, so that both vectors **L** and **S** precess fast around the internuclear axis. Therefore, L and S are not good quantum numbers. The projections on the internuclear axis $\mathbf{\Lambda}$ and $\mathbf{\Sigma}$ however, are well defined. Together they form $\mathbf{\Omega} = \mathbf{\Lambda} + \mathbf{\Sigma}$ which subsequently couples to the angular momentum of the rotation of the nuclei which is denoted **R**. The resulting total angular momentum is denoted **J**. The orientation of **L** and **S** can be reversed, which also reverses the projections on the internuclear axis. Henceforth, there are two-fold degeneracies in Λ and Ω, consequently named Λ- and Ω-type doubling. In many cases the degeneracy is lifted resulting in an additional splitting of energy levels. This will be discussed at a later point (see section 1.8.2).

Hund's case (a) basis wavefunctions can, according to [45] be written in the form $|\eta, v, \Lambda, s, \Sigma, J, \Omega, M_J\rangle$. Here M_J is the component of J along a space fixed axis [45], analogously to atomic physics. The symbol η denotes all quantum numbers which are not explicitly given and v is the vibrational quantum number.

1.5.2 Hund's case (b)

For Hund's case (b) the coupling between **L** and **S** is only weak. The projection $\mathbf{\Lambda}$ of **L** on the internuclear axis is still a good quantum number but $\mathbf{\Omega}$ is no longer defined. $\mathbf{\Lambda}$ couples directly to **R** forming the total angular momentum without spin **N** (in older works **N** is sometimes denoted **K**, e.g. [38]). The total electron spin couples then to **N** to form the total angular momentum **J**. The coupling scheme is depicted in figure 1.6. The coupling between **N** and **S** results in a small splitting for each $N > 1$ if $S = 1/2$. This results in two series of J-levels: $F_1(J)$ with $J = N + 1/2$ and $F_2(J)$ with $J = N - 1/2$. This effect is called spin-rotation splitting and will reappear

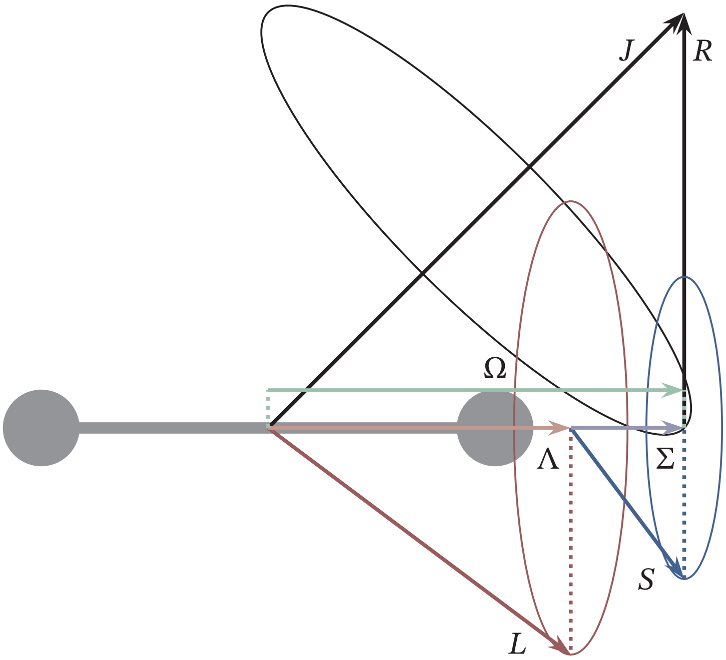

Figure 1.5: Angular momentum coupling scheme for Hund's case (a). After [45]

at the discussion of the effective Hamiltonian (see section 1.8.3). For larger values of S the splitting still exists but with a more complicated structure which is beyond the scope of this work.

The corresponding wavefunctions for Hund's case (b) are $|\eta, v, \Lambda, N, S, J, M_J\rangle$ according to [45]. Hund's case (b) is a good description when the rotational energy is much larger then the spin-orbit energy $A\Lambda \ll BJ$. Σ-states ($\Lambda = 0$) correspond almost always to Hund's case (b) coupling. In the case of $\Lambda \neq 0$ Hund's case (b) coupling is only an appropriate decription for some light molecules.

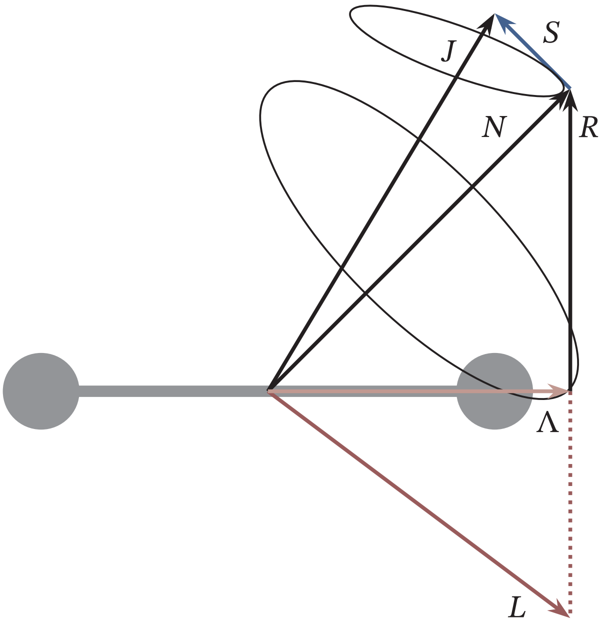

Figure 1.6: Angular momentum coupling scheme for Hund's case (b). After [45]

1.5.3 Hund's case (d)

In Hund's case (d) neither Λ nor Σ is defined, since the coupling between **L** and **R** is stronger than the coupling of **L** to the internuclear axis. Consequently **L** and **R** couple to a resulting vector **N**, which then couples with **S** to form the total angular momentum **J**. This scheme results in $2L + 1$ values of N for each value of R as long as $R > L$.

In Rydberg states (see section 1.10) the excited electron is only weakly interacting with the molecular core due to its large distance to the core and the shielding effect of the electron shell. Therefore, Hund's case (d) is in most cases appropriate to describe Rydberg molecules.

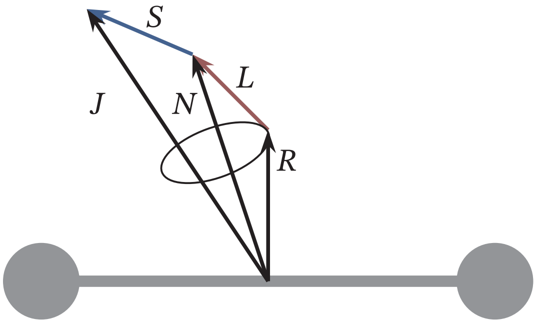

Figure 1.7: Angular momentum coupling scheme for Hund's case (d). After [45]

1.6 Parity of molecular states

Transition probabilities between individual molecular states are strongly linked to parity. Therefore, the concept of parity shall be introduced following [45]. To describe parity in molecules there are two operators that can be defined. The molecule fixed inversion operator i is used to define the overall wave function symmetry with respect to molecule fixed coordinates [45]. However, this operator does not give any information about the total parity of a state. A more general approach is an inversion operator E^* for arbitrary space-fixed coordinates (x_i, y_i, z_i). A function $f(x_i, y_i, z_i)$ of these coordinates is transformed as follows

$$E^* f(x_i, y_i, z_i) = f'(x_i, y_i, z_i) = f(-x_i, -y_i, -z_i). \qquad (1.15)$$

As a consequence for a wave function Ψ it can be written

$$E^*\Psi(x_i, y_i, z_i) = \pm\Psi(x_i, y_i, z_i). \tag{1.16}$$

Parity can then be defined to be positive if Ψ transforms to Ψ and to be negative if Ψ transforms to $-\Psi$.

As discussed in the previous section for diatomic molecules Hund's case (a) and (b) are most common. Even if an intermediate case is present the description will usually be done either with case (a) or case (b) wavefunctions. Therefore, it is crucial to know how case (a) and case (b) wave functions transform with respect to E^*. For Hund's case (a) basis functions the following holds true

$$E^* \left|\eta, \upsilon, \Lambda^s, S, \Sigma, J, \Omega, M_J\right\rangle = (-1)^{J-S+s} \left|\eta, \upsilon, -\Lambda^s, S, -\Sigma, J, -\Omega, M_J\right\rangle. \tag{1.17}$$

The number s has to be introduced within the treatment of the electronic orbital wave function. Because $\Sigma^\pm$ states have to be treated as special cases [45]. For Σ^+ states as well as for $\Lambda > 0$, s is an even number, for Σ^- states it is odd. For wavefunctions in Hund's case (b) the relation is very similar

$$E^* \left|\eta, \upsilon, \Lambda^s, N, \Sigma, S, J, M\right\rangle = (-1)^{N+s} \left|\eta, -\Lambda^s, N, -\Sigma, S, J, M\right\rangle. \tag{1.18}$$

From equation 1.17 and 1.18 one can see that Hund's case (a) and (b) wave functions are not eigenfunctions of E^*. To obtain wave functions with a well defined parity, i.e. eigenfunctions of E^* linear combinations of the respective wave functions have to be formed. For wave functions in Hund's case (a) basis they are given by [45]

$$\left|\eta, \Lambda^s, J, M; +\right\rangle = \frac{1}{\sqrt{2}} \left[\left|\eta, \Lambda^s, S, \Sigma, J, \Omega, M\right\rangle + (-1)^p \left|\eta, -\Lambda^s, S, -\Sigma, J, -\Omega, M\right\rangle\right], \tag{1.19}$$

$$\left|\eta, \Lambda^s, J, M; -\right\rangle = \frac{1}{\sqrt{2}} \left[\left|\eta, \Lambda^s, S, \Sigma, J, \Omega, M\right\rangle - (-1)^p \left|\eta, -\Lambda^s, S, -\Sigma, J, -\Omega, M\right\rangle\right]. \tag{1.20}$$

With exponent $p = J - S + s$. The energy eigenvalues of two wave functions 1.19 and 1.20 are degenerate. However, Λ-type doubling lifts exactly this degeneracy causing

Table 1.1: Overview of the parity labelling scheme introduced in [52]

J	Parity	Label	J	Parity	Label
Integer	$(-1)^J$	e	Half-Integer	$(-1)^{J-1/2}$	e
Integer	$(-1)^{J+1}$	f	Half-Integer	$(-1)^{J+1/2}$	f

a small energy splitting between the different parity levels. As long as this perturbation stays small enough the two functions can still be considered to be eigenfunctions of E^*. As a result of the parity conserving wavefunctions the parity alternates between different J-levels. For example if for $J = 1/2$ the parity $|+\rangle$ is lower than $|-\rangle$ it will be vice versa for $J = 3/2$. To avoid this, a different labelling scheme was proposed [52]. Here the parity label is either e or f. Following this notation the lower and upper parity levels of any value of J will always be denoted by either e or f and no longer alternate. Table 1.1 gives an overview about this labelling scheme which is widely used nowadays. For Hund's case (b) it follows that in Σ^+ states, all parity doublets have the same labels, i.e. F_1 levels are all denoted e and F_2 levels are all denoted f. In the case of Σ^- states the labelling is reversed.

1.7 Electronic transitions and transition rules

Like for atoms the evaluation of the electric transition dipole moment yields a set of rules determining if a certain transition is allowed or not. For molecules those rules can be divided into general rules that will hold in any case and rules that will only apply for a certain Hund's case. The later only apply if both of the involved electronic states belong to the same Hund's case. Since some states may change their Hund's case depending on the rotational quantum number, the rules may even change within a single electronic transition. Table 1.2 gives an overview on the different transition rules which hold either in general or for Hund's case (a) and (b). Transition rules for identical nuclei and nuclei with equal charge are omitted. They can be found in [38]. The parity selection rules can also be rewritten in the e, f-

Table 1.2: Overview of selection rules and their validity for the different quantum numbers and coupling cases in diatomic molecules as given by [38].

Affected Parameter	Selection Rule	Application
Total angular momentum J	$\Delta J = \pm 1, 0$ & $J = 0 \nrightarrow J = 0$	General
Parity $\pm$	$+ \leftrightarrow -$ & $+ \nleftrightarrow +$ & $- \nleftrightarrow -$	General
Total orbital angular momentum projection Λ	$\Delta\Lambda = \pm 1, 0$	Case (a) & (b)
$\Sigma^{\pm}$-states	$\Sigma^+ \leftrightarrow \Sigma^+$ $\Sigma^- \leftrightarrow \Sigma^-$ $\Sigma^+ \nleftrightarrow \Sigma^-$	Case (a) & (b)
Total electron spin S	$\Delta S = 0$	Case (a) & (b)
Total spin projection Σ	$\Delta\Sigma = 0$	Case (a)
Total electronic angular momentum along the internuclear axis Ω	$\Delta\Omega = \pm 1, 0$ & if $\Omega = 0 \rightarrow \Omega = 0$: $\Delta J = 0$ forbidden	Case (a)
Total angular momentum without spin N	$\Delta N = \pm 1, 0$ & for $\Sigma \rightarrow \Sigma$ transitions $\Delta N = 0$ forbidden	Case (b)
Total orbital angular momentum L	$\Delta L = \pm 1, 0$	Case (d)
Rotation R	$\Delta R = 0$	Case (d)

labelling scheme. In this scheme $\Delta J = 0$ transitions require $e \leftrightarrow f$ and $\Delta J = \pm 1$ require $e \leftrightarrow e$ and $f \leftrightarrow f$ [52].

1.8 The effective Hamiltonian approach

The interaction between the different angular momenta leads to a rich and complex energy structure for diatomic molecules. One way to treat such a complex system is perturbation theory. Here, the Hamiltonian H is separated into a strictly solvable part H_0 and a perturbation H_1 which is only a small correction to H_0.[53].

The separation of the Hamiltonian may prove to be difficult or in some cases even impossible. An alternative approach is the effective Hamiltonian. This is essentially a large matrix including terms for all the different angular momentum couplings and interactions within the molecule. The matrix can also include terms describing the interaction with external fields. It can be diagonalised to obtain the energy eigenvalues. This method requires enough computational power to diagonalise large and complex matrices.

For the effective Hamiltonian it is crucial to choose an appropriate set of basis states and to include only a single electronic state. Dealing with several electronic states at the same time will overcomplicate the Hamiltonian. However, exceptions exist. When different adjacent electronic states perturb each other, it is necessary to include all those states to describe the system correctly.

In general, the matrix elements of the effective Hamiltonian have the form

$$\langle \psi_f \,|\, \mathrm{H}_{\mathrm{int}} \,|\, \psi_i \rangle \,. \tag{1.21}$$

With the initial state ψ_i, the final state ψ_f and the sub-Hamiltonian $\mathrm{H}_{\mathrm{int}}$ describing a certain type of interaction. The matrix elements of the effective Hamiltonian given here are all given for Hund's case (a) basis states.

For the Wigner-3j and Wigner-6j symbols the following notation is used

$$\text{Wigner 3j-symbol:}\begin{pmatrix} a & b & c \\ d & e & f \end{pmatrix},$$
$$\text{Wigner 6j-symbol:}\begin{Bmatrix} a & b & c \\ d & e & f \end{Bmatrix}.$$

1.8.1 Fine structure effective Hamiltonian

The fine structure of a diatomic molecule depends mainly on two terms. The spin-orbit interaction and the rotational term. The spin-orbit matrix elements are fully diagonal in case (a) basis description and according to [45, 54] given by

$$\begin{aligned} \langle \psi \,|\, \mathrm{H}_{\mathrm{SO}} \,|\, \psi' \rangle = \delta_{\eta\eta'}\delta_{\Lambda\Lambda'}\delta_{\Sigma\Sigma'}\delta_{\Omega\Omega'}\Lambda\Sigma \\ \times \left[A + A_D(J(J+1) - \Omega^2 + S(S+1) - \Sigma^2)\right]. \end{aligned} \tag{1.22}$$

The spin-orbit constant is denoted as A, while A_D is the constant to correct for the centrifugal distortion of A.

To include the rotational energies the corresponding matrix element is [45, 54]

$$\begin{aligned} \langle \psi \,|\, \mathrm{H}_{\mathrm{ROT}} \,|\, \psi' \rangle = \delta_{\eta\eta'}\delta_{\Lambda\Lambda'}\delta_{\Sigma\Sigma'}\delta_{\Omega\Omega'} &\left[2B\Lambda\Sigma + B(J(J+1) + S(S+1) + \Lambda^2 - 2\Omega^2\right] \\ &- 2B \sum_{q=\pm1} (-1)^{J-\Omega+S-\Sigma} \begin{pmatrix} J & 1 & J \\ -\Omega & q & \Omega' \end{pmatrix} \begin{pmatrix} S & 1 & S \\ -\Sigma & q & \Sigma' \end{pmatrix} \\ &\times \sqrt{J(J+1)(2J+1)S(S+1)(2S+1)}. \end{aligned} \tag{1.23}$$

Here, the first term is again strictly diagonal while the sum over q may give some off-diagonal contributions. To correct for the centrifugal distortion two additional matrix elements can be included depending on the two correction constants D and H[54]:

$$\langle \psi \,|\, \mathrm{H}_{\mathrm{ROTCD}} \,|\, \psi' \rangle = -D\left(H_{\mathrm{ROT}}\right)^2 + H\left(H_{\mathrm{ROT}}\right)^4. \tag{1.24}$$

In many cases it is justified to omit the $(H_{\mathrm{ROT}})^4$ term or even both of the terms, since their energy contribution is negligible compared to $\langle\psi\,|\,H_{\mathrm{ROT}}\,|\,\psi'\rangle$.

1.8.2 Λ-type doubling

Λ-type doubling is an effect that does not occur in an ideal Hund's case (a) or (b) picture, where the coupling between the total electronic angular momentum and the rotation of the nuclei is neglected. If the speed of rotation is large, which is the case for many molecules, this effect has to be taken into account [38].

The additional interaction lifts the degeneracy between the two symmetry components + and − for $\Lambda \neq 0$ as already stated in section 1.6. The splitting between the two parity components for each J is small but increases with increasing J [38]. The effect is usually on the order of MHz to GHz. For its description the three parameters o, p, q are introduced. For Π-states Λ-type doubling has been treated by Brown and Merer [55], who give the following relations to obtain the matrix elements for Λ-type doubling in Π-states

$$\begin{aligned}
\langle\psi\,|\,\mathrm{H}_\Lambda\,|\,\psi'\rangle &= \langle\mp1, \Sigma=\Sigma'\pm2, J=J', \Omega=\Omega'\,|\,\mathrm{H}_\Lambda\,|\,\pm1,\Sigma',J',\Omega'\rangle \\
&= \frac{1}{2}(o_v+p_v+q_v)\sqrt{[S(S+1)-\Sigma(\Sigma\pm1)][S(S+1)-(\Sigma\pm1)(\Sigma\pm2)]}, \\
\langle\psi\,|\,\mathrm{H}_\Lambda\,|\,\psi'\rangle &= \langle\mp1, \Sigma=\Sigma'\pm1, J=J', \Omega=\Omega'\mp1\,|\,\mathrm{H}_\Lambda\,|\,\pm1,\Sigma',J',\Omega'\rangle \\
&= -\frac{1}{2}(p_v+2q_v)\sqrt{[S(S+1)-\Sigma(\Sigma\pm1)][J(J+1)-\Omega(\Omega\mp1)]}, \\
\langle\psi\,|\,\mathrm{H}_\Lambda\,|\,\psi'\rangle &= \langle\mp1, \Sigma=\Sigma', J=J', \Omega=\Omega'\mp2\,|\,\mathrm{H}_\Lambda\,|\,\pm1,\Sigma',J',\Omega'\rangle \\
&= \frac{1}{2}q\sqrt{[J(J+1)-\Omega(\Omega\mp1)][J(J+1)-(\Omega\mp1)(\Omega\mp2)]}.
\end{aligned} \tag{1.25}$$

1.8.3 Spin-rotation coupling

Spin-rotation coupling occurs for Hund's case (b), when the total electronic spin couples to the total angular momentum without spin. This has been discussed in detail in section 1.5.2 and is decribed by the constant γ. The corresponding matrix elements in Hund's case (a) basis are given by [54] to be

$$\begin{aligned}\langle\psi\,|\,\mathrm{H_{SROT}}\,|\,\psi'\rangle = \gamma\delta_{J,J'}\Bigg[&\delta_{\Sigma,\Sigma'}\delta_{\Omega,\Omega'}(\Sigma^2 - S(S+1)) + \sum_{q=\pm 1}(-1)^{J'-\Omega+S-\Sigma}\\ &\times\sqrt{J(J+1)(2J+1)}\sqrt{S(S+1)(2S+1)}\\ &\times\begin{pmatrix} J & 1 & J' \\ -\Omega & q & \Omega' \end{pmatrix}\begin{pmatrix} S & 1 & S \\ -\Sigma & q & -\Sigma' \end{pmatrix}\Bigg].\end{aligned} \tag{1.26}$$

Since spin-rotational coupling is especially important for Hund's case (b), the matrix element shall also be given in Hund's case (b) basis [45]. Note that in Hund's case (b) basis the matrix element is fully diagonal.

$$\langle\psi\,|\,\mathrm{H_{SROT}}\,|\,\psi\rangle = \gamma(-1)^{N+J+S}\begin{Bmatrix} S & N & J \\ N & S & 1 \end{Bmatrix}\sqrt{S(S+1)(2S+1)N(N+1)(2N+1)}. \tag{1.27}$$

The spin-rotational splitting can also be corrected for the centrifugal distortion with the corresponding correction parameter γ_D. The correction term depends also on the rotational Hamiltonian [54].

$$\langle\psi\,|\,\mathrm{H_{SROT}}\,|\,\psi'\rangle = \mathrm{H_{SROT}} + \frac{\gamma_D}{\gamma}\mathrm{H_{ROT}}\cdot\mathrm{H_{SROT}}. \tag{1.28}$$

1.9 Hyperfine structure

The smallest structural details of the energy landscape in diatomic molecules are called hyperfine structure. Like in atoms the hyperfine structure results from the coupling between the total angular momentum of the molecule J and the nuclear spin I. The two angular momenta form the total angular momentum $F = J + I$. The situation gets more complicated if the nuclei forming a diatomic molecule both have a non-zero nuclear spin. Yet, this is not the case for the present treatment of nitric oxide and as a result omitted.

To fully describe the hyperfine structure several different interactions have to be taken into account. The matrix elements summarised in this section were taken from [45], where also a more detailed derivation of the individual matrix elements can be found. Typographical errors that came to the attention of the author have been corrected. All matrix elements are given in Hund's case (a) basis.

The first interaction taken into account is the spin orbit interaction for the nuclear spin I with the total angular orbital momentum of the electrons L. The corresponding hyperfine constants is denoted a and the matrix element is given by [45]

$$\begin{aligned}\left\langle \psi \,\middle|\, \mathrm{H}^{\mathrm{Orbit}}_{\mathrm{HFS}} \,\middle|\, \psi' \right\rangle = a\Lambda(-1)^{J'+F+I}&\begin{Bmatrix} I & J' & F \\ J & I & 1 \end{Bmatrix}\sqrt{I(I+1)(2I+1)} \\ \times (-1)^{J-\Omega}&\begin{pmatrix} J & 1 & J' \\ -\Omega & 0 & \Omega' \end{pmatrix}\sqrt{(2J+1)(2J'+1)}.\end{aligned} \tag{1.29}$$

The magnetic hyperfine interaction results form the interaction of the nuclear spin I and the total electron spin S. For its description either the constant b or the Fermi contact constant b_F can be employed. The matrix element including the latter one is given by [45]

$$\begin{aligned}\left\langle \psi \,\middle|\, \mathrm{H}^{\mathrm{Magnetic}}_{\mathrm{HFS}} \,\middle|\, \psi' \right\rangle = b_F(-1)^{J'+F+I}&\begin{Bmatrix} I & J' & F \\ J & I & 1 \end{Bmatrix}\sqrt{I(I+1)(2I+1)} \\ \times \sum_{q=-1}^{1}(-1)^{J-\Omega}&\begin{pmatrix} J & 1 & J' \\ -\Omega & q & \Omega' \end{pmatrix}\sqrt{(2J+1)(2J'+1)} \\ \times (-1)^{S-\Sigma}&\begin{pmatrix} S & 1 & S \\ -\Sigma & q & \Sigma' \end{pmatrix}\sqrt{S(S+1)(2S+1)}.\end{aligned} \tag{1.30}$$

In addition to the magnetic interaction, the dipole-dipole interaction between the nuclear spin and electron spin has to be included. It is included via the following matrix element [45]

$$\begin{aligned}\left\langle\psi\right|\mathrm{H}_{\mathrm{HFS}}^{\mathrm{Dipole}}\left|\psi'\right\rangle = \sqrt{30}g_s\mu_B g_N\mu_N\frac{\mu_0}{4\pi}(-1)^{J'+F+I}\begin{Bmatrix} I & J' & F\\ J & I & 1\end{Bmatrix}\sqrt{I(I+1)(2I+1)}\\ \times\sum_{q=-1}^{1}(-1)^{J-\Omega+q}\begin{pmatrix} J & 1 & J'\\ -\Omega & q & \Omega'\end{pmatrix}\sqrt{(2J+1)(2J'+1)}\\ \times\sum_{q_1=-1}^{1}\sum_{q_2=-2}^{2}\begin{pmatrix} 1 & 2 & 1\\ q_1 & q_2 & -q\end{pmatrix}(-1)^{S-\Sigma}\begin{pmatrix} S & 1 & S\\ -\Sigma & q_1 & \Sigma'\end{pmatrix}\\ \times\sqrt{S(S+1)(2S+1)}\left\langle\eta,\Lambda\right|C_{q_2}^2(\theta,\phi)(r^{-3})\left|\eta',\Lambda'\right\rangle.\end{aligned} \tag{1.31}$$

The remaining matrix element including C_{q2}^2 can be resolved with the following definition which includes the spherical harmonic $Y_{kq}(\theta,\phi)$ [45],

$$C_q^k(\theta,\phi) = \sqrt{\frac{4\pi}{2k+1}}Y_{kq}(\theta,\phi). \tag{1.32}$$

Substituting the matrix element with the corresponding spherical harmonics allows the identification of the dipolar hyperfine constants [45]

$$t_0 = g_S\mu_B g_N\mu_N\frac{\mu_0}{8\pi}\left\langle\frac{3\cos^2(\theta)-1}{r^3}\right\rangle_\Pi, \tag{1.33a}$$

$$t_{\pm1} = g_S\mu_B g_N\mu_N\frac{\mu_0}{4\pi}\left\langle\frac{\cos(\theta)\sin(\theta)}{r^3}\right\rangle_{\Pi-\Sigma}, \tag{1.33b}$$

$$t_{\pm2} = g_S\mu_B g_N\mu_N\frac{\mu_0}{4\pi}\left\langle\frac{\sin^2(\theta)}{r^3}\right\rangle_\Pi. \tag{1.33c}$$

A different approach to treat the dipole-dipole interaction relies on the dipole-dipole constants c and d. The first one is diagonal in Λ while the second one in $\Lambda/2$. The constant c also links b and b_F via the relation $b = b_F - (c/3)$[36]. The corresponding matrix element is given in [54]

$$
\begin{aligned}
\left\langle \psi \middle| \mathrm{H}_{\mathrm{HFS}}^{\mathrm{AltDip}} \middle| \psi' \right\rangle = {} & \delta_{\Lambda\Lambda'}(-1)^{J'+I+F}\sqrt{(2J+1)(2J'+1)}\sqrt{I(I+1)(2I+1)} \\
& \times \begin{Bmatrix} F & J' & I \\ 1 & I & J \end{Bmatrix} \left(\sum_{q=-1}^{1} (-1)^{J-\Omega} \begin{pmatrix} J & 1 & J' \\ -\Omega & q & \Omega' \end{pmatrix} c\frac{\sqrt{30}}{3} \right. \\
& \times (-1)^{q+S-\Sigma}\sqrt{S(S+1)(2S+1)} \begin{pmatrix} S & 1 & S \\ -\Sigma & q & \Sigma' \end{pmatrix} \\
& \left. \times \begin{pmatrix} 1 & 2 & 1 \\ -q & 0 & q \end{pmatrix} \right) - d(-1)^{J'+I+F}\sqrt{(2J+1)(2J'+1)} \\
& \times \sqrt{I(I+1)(2I+1)} \begin{Bmatrix} F & J' & I \\ 1 & I & J \end{Bmatrix} \left(\sum_{q=\pm 1} \delta_{\Lambda\Lambda'-2q}(-1)^{J-\Omega} \right. \\
& \times (-1)^{q+S-\Sigma}\sqrt{S(S+1)(2S+1)} \begin{pmatrix} J & 1 & J' \\ -\Omega & -q & \Omega' \end{pmatrix} \\
& \left. \times \begin{pmatrix} S & 1 & S \\ -\Sigma & q & \Sigma' \end{pmatrix} \right) \\
& + c_I \delta_{\Sigma\Sigma'}\delta_{\Lambda\Lambda'}\delta_{JJ'}\frac{1}{2}[F(F+1) - I(I+1) - J(J+1)].
\end{aligned} \tag{1.34}
$$

It also includes a term proportional to the constant c_I which takes the nuclear spin-rotation interaction into account.

The last interaction term that has to be discussed is the quadrupole term for the nuclear spin. It is given by [45]

$$
\begin{aligned}
\left\langle \psi \,\middle|\, \mathrm{H}_{\mathrm{HFS}}^{\mathrm{Quadpole}} \,\middle|\, \psi' \right\rangle = \delta_{\Sigma\Sigma'}(-1)^{J'+I+F} &\begin{Bmatrix} I & J & F \\ J' & I & 2 \end{Bmatrix} \left(\frac{-eQ}{2}\right) \begin{pmatrix} I & 2 & I \\ -I & 0 & I \end{pmatrix}^{-1} \\
\times &\sum_{q=-2}^{2} (-1)^{J-\Omega} \begin{pmatrix} J & 2 & J' \\ -\Omega & q & \Omega' \end{pmatrix} \sqrt{(2J+1)(2J'+1)} \\
&\left\langle \eta\Lambda \,\middle|\, T_q^2(\nabla \mathbf{E}) \,\middle|\, \eta'\Lambda' \right\rangle .
\end{aligned}
\tag{1.35}
$$

Here, the remaining matrix element including the tensor of the electric field gradient $T_q^2(\nabla \mathbf{E})$ allows the defintion of its $q = 0, \pm 2$ components. These are given by [45]

$$
\left\langle \Lambda \,\middle|\, T_0^2(\nabla \mathbf{E}) \,\middle|\, \Lambda' \right\rangle = -\frac{1}{2} \left\langle \Lambda \,\middle|\, \sum_i \frac{e_i}{4\pi\varepsilon_0} \frac{3\cos^2(\theta_i)}{r_i^3} \,\middle|\, \Lambda' \right\rangle = -\frac{1}{2} q_0, \tag{1.36a}
$$

$$
\begin{aligned}
\left\langle \Lambda = \pm 1 \,\middle|\, T_{\pm 2}^2(\nabla \mathbf{E}) \,\middle|\, \Lambda' = \mp 1 \right\rangle &= -\frac{1}{2\sqrt{6}} \left\langle \Lambda \,\middle|\, \sum_i \frac{e_i}{4\pi\varepsilon_0} \frac{\sin^2(\theta_i)}{r_i^3} \,\middle|\, \Lambda \right\rangle \\
&= -\frac{1}{2\sqrt{6}} q_2 .
\end{aligned}
\tag{1.36b}
$$

The constants eQ and q_0, q_2 can be cumulated to form the nuclear quadrupole constants eQq_0 and eQq_2. Here, the first one is diagonal in Λ and the second one in $\Lambda/2$. The constant ε_0 is the dielectric constant and e_i the elementary charge of electron i.

1.10 Rydberg states

Rydberg states are already mentioned in the discussion of Hund's case (d) in section 1.5.3. They are atomic or molecular states where a single electron is excited, to a high principle quantum number [56]. Rydberg atoms or molecules can be described as hydrogen like, since the inner electrons shield the excited electron from the nucleus so that the other electrons are mainly influenced by the potential of a single positive charge [56].

According to the Bohr model the energy of an electron with principle quantum number n is given by [37]

$$E_n = -\frac{e^2}{4\pi\varepsilon_0} \cdot \frac{1}{2a_o} \cdot \frac{Z^2}{n^2} = -Ry\frac{Z^2}{n^2}. \tag{1.37}$$

With the elementary charges e, dielectric constant ε_0 and the Bohr radius $a_0 = (4\pi\varepsilon_0\hbar^2)/(e^2 m_e)$, including the electron mass m_e. The energy depends only on the proton number Z and the principle quantum number. Here, the Rydberg constant $Ry = 13.6\,\mathrm{eV}$ is introduced. To describe Rydberg atoms or molecules equation 1.37 has to be altered. The principle quantum number is substituted by an effective principle quantum number $n' = n - \delta_{nlj}$. The quantum defect δ_{nlj} depends on the respective Rydberg state. A thorough review on quantum defect theory was published by Seaton [57].

Not every molecules seams to be suitable for the excitation to Rydberg states. And according to Herzberg [58] along time the only known Rydberg molecules had been He_2. However, nowadays Rydberg states have been observed in many molecules, like for example in H_2S [59], H_2O and D_2O [60], ammonia [61] and even in large hydrocarbons like tetracene ($C_{18}H_{12}$) [62]. A good overview, especially for the earlier research on Rydberg molecules is provided by Herzberg [58].

2 Excitation scheme and spectroscopic techniques

Introduction

In chapter 1 the general energy structure of diatomic molecules has been discussed. Chapter 2 specifically focuses on the energy structure of nitric oxide and the two spectroscopic techniques that were used within the scope of this thesis.

At first, nitric oxide is introduced and its general properties will be summarised in section 2.1. Subsequently, the excitation scheme for the Rydberg excitation of nitric oxide is presented and the structure of the involved electronic states is discussed in section 2.2.1-2.2.3. The Rydberg excitation is crucial to employ optogalvanic spectroscoy which is described in section 2.3. The chapter ends with the description of Doppler-free saturation spectroscopy and a brief overview on the respective broadening mechanisms in section 2.4.

2.1 Nitric oxide

Nitric oxide is a colourless and odourless gas. It is toxic [63] and highly reactive since it is a free radical. Its electron configuration in the ground state is

$$(1\sigma)^2(2\sigma)^2(3\sigma)^2(4\sigma)^2(5\sigma)^2(1\pi)^4(2\pi)^1,$$

[45, 64] or rewritten in the hybridized picture

$$(1s\sigma)^2(1s\sigma^*)^2(2s\sigma)^2(2s\sigma^*)^2(2p\sigma)^2(2p\pi)^4(2p\pi^*)^1.$$

There are two stable isotopes of nitrogen ^{14}N and ^{15}N and three stable isotopes of oxygen ^{16}O, ^{17}O and ^{18}O. Thus, a total of six different isotopologues exist for nitric oxide. ^{14}N and ^{16}O are by far the most abundant isotopes of nitrogen and oxygen [65]. The most abundant isotopologue of nitric oxide is therefore ^{14}N^{16}O which is subject to this study. It has a mass of 30 u and a chemical bond length of 115 pm [66]. Nitric oxide has a small permanent dipole moment, $\mathbf{d}_{\mathrm{NO}} \approx 0.16\,\mathrm{D}$ [66]. Its total nuclear spin is $I = 1$ resulting from the nuclear spin of ^{14}N[67].

2.2 Excitation of NO to a Rydberg state

To perform optogalvanic spectroscopy in nitric oxide the molecules have to be excited to high lying Rydberg states. The addressed Rydberg states have to be so close to the ionisation threshold, that the collisional energies are sufficient to ionise the excited molecules. For the excitation to Rydberg states three transitions are driven. The employed excitation scheme is similar to the scheme described in [68]. Doppler-free spectroscopy was only performed on the lowest of the three transitions. An overview about the excitation scheme is given in this section. The individual transitions are discussed in detail in the subsequent sections 2.2.1-2.2.3

Figure 2.1 shows the excitation scheme used within the scope of this thesis. The first transition from the $\mathrm{X}\,^2\Pi_{3/2}$ state to the $\mathrm{A}\,^2\Sigma^+$ state can not be avoided even though the wavelength of 226 nm is inconvenient to work with. Since light in the deep UV is difficult to generate and requires additional safety gear, to avoid skin exposure and minimise the risk of skin cancer. It is not possible to avoid the $\mathrm{A}\,^2\Sigma^+$ state because there is no electronic state in between the ground state $\mathrm{X}\,^2\Pi$ and $\mathrm{A}\,^2\Sigma^+$ which corresponds to a single electron excitation within the molecule [69]. There are lower lying electronic states where more than a single electron is excited within the molecule [70]. The transition can be driven from both spin-orbit manifolds of the ground state since both of them are populated at room temperature [71].

The second transition in the excitation scheme is at a wavelength of around 540 nm between the A $^2\Sigma^+$ state and the H $^2\Sigma^+$ state. This transition requires a lot of power due to the different l-character of the electronic wave function. Its decomposition into partial waves for the corresponding states is given in [72]. The A $^2\Sigma^+$ state has 94 % s-character, 1 % p-character and 4 % d-character. The H $^2\Sigma^+$ state has 38 % s- and 62 % d-character. The H′ $^2\Pi$ state could in principle be reached with the employed laser systems but is assumed to require even more power since it has 99 % d- and 1 % p-character. A four-photon excitation scheme would be possible since there are states in between A $^2\Sigma^+$ and H $^2\Sigma^+$ [73], that could be reached with infrared transitions. However, according to [74] these alternative excitation schemes may suffer from predissociation and are therefore not suited for the use of optogalvanic spectroscopy. Especially, if the technique is used for sensing as it was explained in the introduction. From the H $^2\Sigma^+$ state a large number of Rydberg states are accessible. Depending on which Rydberg state should be adressed the required wavelength is between 833 and 835 nm. This wavelength region is covered by several different laser technologies. The choice of Rydberg state may offer a large optimisation potential for the sensing application of optogalvanic spectroscopy.

2.2.1 The A $^2\Sigma \leftarrow$ X $^2\Pi_{3/2}$ transition in nitric oxide

Figure 2.3 shows a schematic of the energy level structure of the X $^2\Pi$ ground state of nitric oxide and the A $^2\Sigma^+$ excited state.

The ground state is spin-orbit split by around 123 cm^{-1} [35]. It does neither belong exactly to Hund's case (a) nor to Hund's case (b) [27]. It can be best described by Hund's case (a) as long as the rotational energy is small enough. For larger rotational energies the Hund's case (b) description is more appropriate. The respective transition from Hund's case (a) to Hund's case (b) can be estimated by $J_{(a)\rightarrow(b)} \approx A/(2B)$ (for the respective constants see: table C.1.1) which yields that the transition occurs at $J_{(a)\rightarrow(b)} \approx 35.5$ [51]. The transition between the two different coupling cases has been studied in detail by Klisch et al. [75] using sub-millimetre wave spectroscopy. The ground state shows Λ-type doubling for both spin-orbit manifolds, i.e. the degeneracy of the two symmetry components ± is lifted. The splitting behaves differently for the two ground state manifolds. It can be calculated using the effective

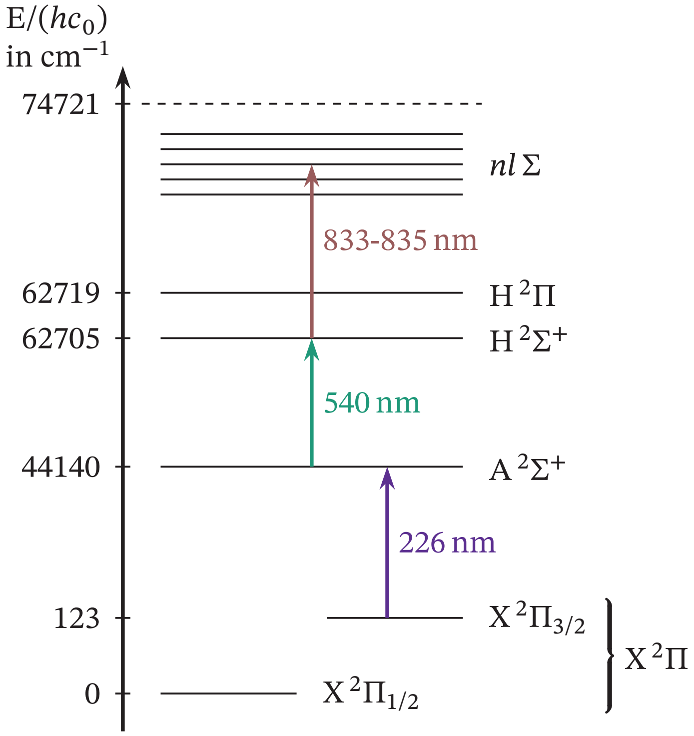

Figure 2.1: Excitation scheme for the Rydberg excitation of nitric oxide. For all electronic states only vibrational states with $\upsilon = 0$ are addressed. The rotational structure is omitted. The dashed line marks the first ionisation limit.

Hamiltonian approach introduced in section 1.8 taking into account the matrix elements given in equation 1.22 and 1.23 for the spin-orbit and rotational fine structure and in equation 1.26 and equation 1.25 for spin-rotation and Λ-type doubling. The centrifugal distortion term in equation 1.22 can be neglected, thus A_D is set to zero. Note that in Hund's case (a) the basis states are not parity conserving, i.e. do not have a definite parity. Henceforth, the effective Hamiltonian has to be transformed to the parity conserving base states which were introduced in section 1.6 (see. equation 1.19 and 1.20). Plugging in the respective constants from [35] which are given in table C.1.1, yields the splittings that are plotted in figure 2.2. In the $\Pi_{1/2}$ component the splitting is significantly larger then in the $\Pi_{3/2}$ component and goes approximately linear with J_X. For the $\Pi_{3/2}$ manifold the splitting is proportional to J_X^2. The hyperfine structure is not shown in figure 2.3 and will be discussed in more detail in chapter 6.

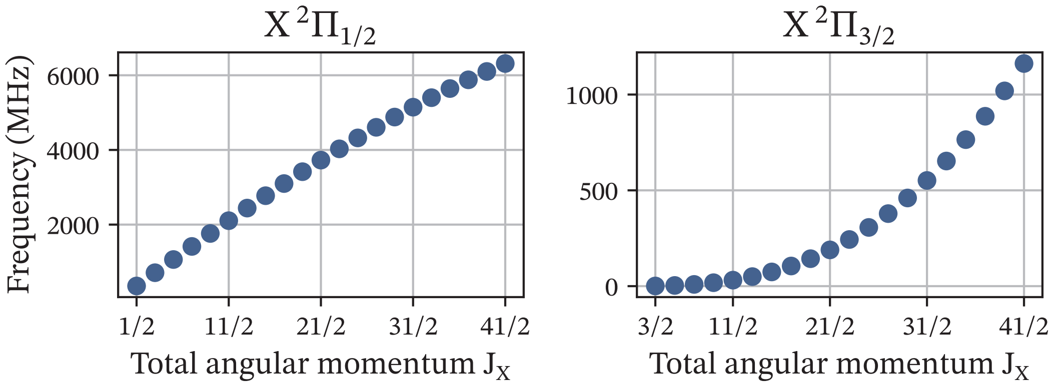

Figure 2.2: Calculated Λ-type doubling for the two spin-orbit manifolds of the ground state $X\,^2\Pi$ of nitric oxide.

The $A\,^2\Sigma^+$ state strictly belongs to Hund's case (b). It shows the characteristic spin-rotational splitting. Here states with parity +, e belong always to the F_1 manifold, i.e. $J = N + 1/2$ and states with parity −, f to the F_2 manifold for which $J = N - 1/2$ holds.

There are twelve allowed branches for the $A\,^2\Sigma^+ \leftarrow X\,^2\Pi$ transition. Each branch consists of transitions between different rotational levels in the ground and excited state. Figure 2.3 shows only a single rotational transition for each of the branches. The notation for the branches translates as follows: e.g. Q_{21fe} is a branch with transitions of $\Delta J = 0$ denoted by the letter Q ($R \rightarrow \Delta J = 1$, $P \rightarrow \Delta J = -1$). The letters in the subscript denote that the transition is from an e-level in the lower state to an f-level in the upper state. The numbers in the subscript give the respective F-component, i.e. 21 denotes a transition from an F1 component in the lower to a F2 component in the upper state. Here, caution is necessary since the definition of the F-components is different for Hund's case (a) and (b).

The P_{12ee}-branch is of particular interest to this thesis, since all measurements were performed on different rotational transitions of this branch. The branch lies in the outermost part of the total spectrum, and does only overlap with other branches for $J > 19.5$, so that the line assignment is particularly easy. In addition, it has already been experimentally shown that the excitation from the $X\,^2\Pi_{3/2}$ via the $A\,^2\Sigma^+$ to the $H\,^2\Sigma^+$ state is possible and able to generate enough population in the $H\,^2\Sigma^+$ state for quantitative measurements [76]. This is crucial for the application of optogalvanic spectroscopy for sensing.

2.2.2 The 3d-complex states $H\,^2\Sigma^+$ and $H'\,^2\Pi$

The second transition in the presented excitation scheme involves the $H\,^2\Sigma^+$ state which cannot be treated without considering the $H'\,^2\Pi$ state as well. The two states lie only approximately $14\,\mathrm{cm}^{-1}$ away from each other [77]. A level scheme for the transition from the $A\,^2\Sigma^+$ to the $H\,^2\Sigma^+$ and $H'\,^2\Pi$ state is shown in figure 2.4. The branch in which the particular transition of the presented excitation scheme lies is highlighted by a green arrow. Both the $H\,^2\Sigma^+$ and $H'\,^2\Pi$ states are best described by the Hund's case (b) coupling scheme [68]. There are in total six branches from the $A\,^2\Sigma^+$ to the $H\,^2\Sigma^+$ state and twelve for the transition to the $H'\,^2\Pi$ state. The small letter in front of the capital letter defining the ΔJ-type of a transition is giving the type of transition for the ΔN, thus rR for example means $\Delta N = +1$ and $\Delta J = +1$. The closeness of the $H\,^2\Sigma^+$ state and $H'\,^2\Pi$ state hinders the straight forward cal-

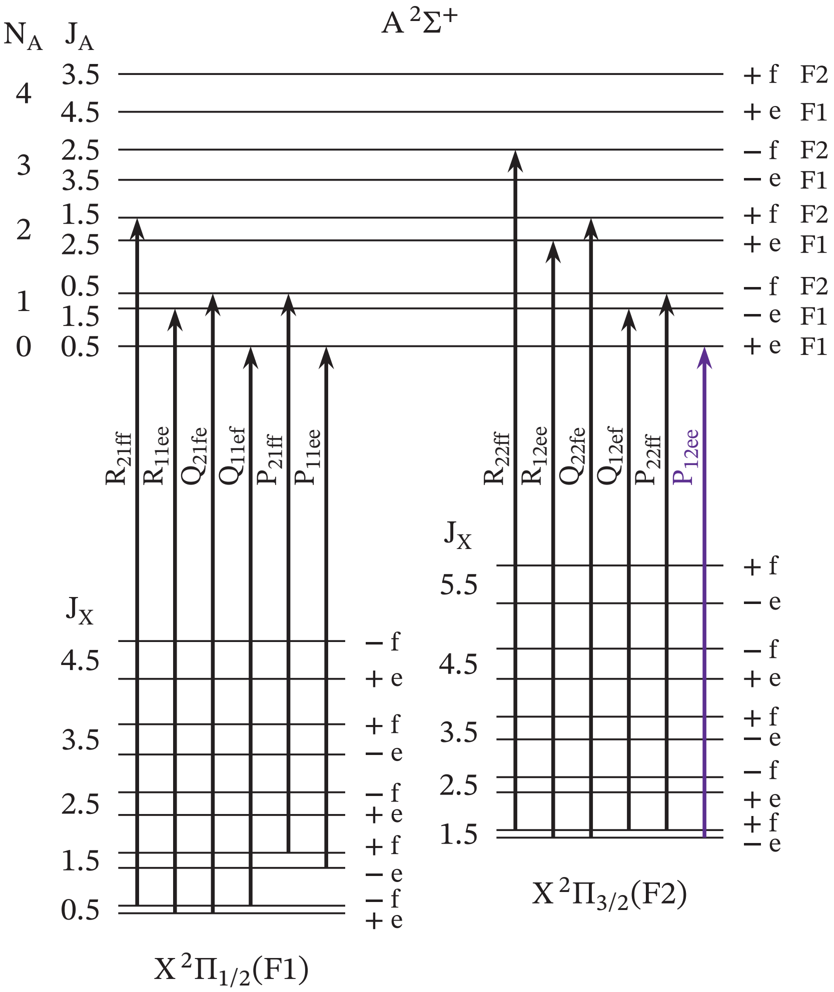

Figure 2.3: Schematic of the A $^2\Sigma^+$ ← X $^2\Pi$ transition showing the fine structure of both states and the transition with lowest J_X as an example for every of the twelve allowed branches in the corresponding spectrum of the transition. The P_{12ee} branch investigated as part of this thesis is highlighted in violet. In the ground state the splitting between the + and − symmetry component of each J, is the aforementioned Λ-type doubling. After [27].

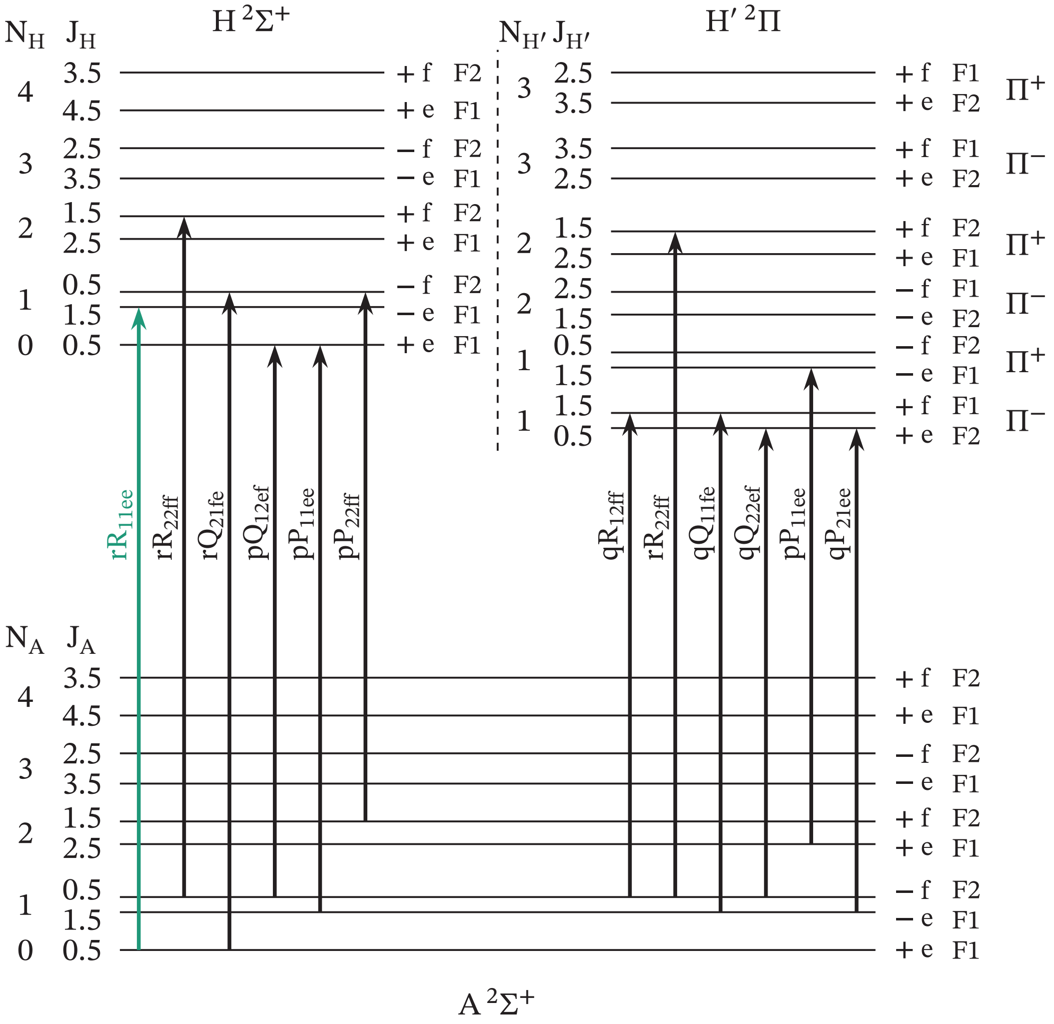

Figure 2.4: Level scheme for the transition between the $A\,^2\Sigma^+$ and $H\,^2\Sigma^+$, $H'\,^2\Pi$ states, respectively. For the transition between $A\,^2\Sigma^+$ and $H\,^2\Sigma^+$ all six branches are shown. From the twelve branches existing for the transitions between $A\,^2\Sigma^+$ and $H'\,^2\Pi$ six exemplary branches are shown. After [68].

culation of the molecular energy levels by simple effective Hamiltonian matrix elements. In fact the two states are so close to each other that they perturb each others energetic structure. Their treatment therefore requires a set of off-diagonal interaction parameters that describe the perturbing interaction and shift the energy levels of the individual states accordingly. The perturbation within the H and H' state is heterogeneous and was already studied in the sixties by Huber, Miescher [78] and Kovács [79]. The H and H' states have mostly d-character [75] and are also referred to as $3d\sigma$ and $3d\pi$ states, respectively. They belong to a set of states referred to as 3d-Rydberg complex which also includes the $3d\delta$-state $F\,^2\Delta$ which is additionally interacting with higher vibrational states of the $B'\,^2\Delta$ state. In addition to the $3d$-states also the close lying $4s\sigma$-state $E\,^2\Sigma^+$ is involved forming an s-d supercomplex [77]. The full system has been described by Bernard et. al. in [77].

If one wants to calculate the energy levels of the H and H' state it is sufficient to use a 5×5-matrix description neglecting the interaction with the $B'\,^2\Delta$ and $E\,^2\Sigma^+$ [68]. In fact Bernard et al. were not able to accurately determine the interaction constant linking the $4s\sigma$ and $3d\sigma$-state, since it seems to be too small to be determined from their data [77]. The description is given in Hund's case (a) basis in equation 2.1. The off diagonal matrix elements including the interaction parameters α, β, η and ξ were retrieved from [77] while the diagonal elements and the matrix elements M_{12}, M_{34} can be found in [80].

$$\begin{array}{c} \begin{array}{ccccc} F\,^2\Delta_{5/2} & F\,^2\Delta_{3/2} & H'\,^2\Delta_{3/2} & H'\,^2\Delta_{1/2} & H\,^2\Sigma^+ \end{array} \\ \begin{pmatrix} M_{11} & -B_{\mathrm{F}}\sqrt{X} + 2D_{\mathrm{F}}X^{3/2} & -\beta\sqrt{Y} & 0 & 0 \\ \ldots & M_{22} & \alpha + \beta & -\beta\sqrt{Z} & 0 \\ \ldots & \ldots & M_{33} & -B_{\mathrm{H'}}\sqrt{X} + 2D_{\mathrm{H'}}X^{3/2} & -\eta\sqrt{Z} \\ \ldots & \text{symmetric} & \ldots & M_{44} & \xi + \eta M \\ \ldots & \ldots & \ldots & \ldots & M_{55} \end{pmatrix} \end{array} \tag{2.1}$$

The diagonal elements M_{ii} are given by the following equations

$$M_{11} = T_{\text{F}} + A_{\text{F}} + B_{\text{F}}(X-2) - D_{\text{F}}((X-2)^2 + X), \tag{2.2}$$
$$M_{22} = T_{\text{F}} - A_{\text{F}} + B_{\text{F}}(X+2) - D_{\text{F}}((X+2)^2 + X), \tag{2.3}$$
$$M_{33} = T_{\text{H}'} + \frac{1}{2}A_{\text{H}'} + B_{\text{H}'}(X-1) - D_{\text{H}'}((X-1)^2 + X), \tag{2.4}$$
$$M_{44} = T_{\text{H}'} - \frac{1}{2}A_{\text{H}'} + B_{\text{H}'}(X+1) - D_{\text{H}'}((X+1)^2 + X), \tag{2.5}$$
$$M_{55} = T_{\text{H}} + B_{\text{H}}x(x \mp 1) - D_{\text{H}}x^2(x \mp 1)^2. \tag{2.6}$$

The upper sign in equation 2.6 refers to e-sublevels and the lower sign to f-sublevels. The following abbreviations were used for clarity in equation 2.1 - 2.6

$$\begin{aligned} X &= (J+1/2)^2 - \Lambda^2, & x &= J + 1/2, \\ Y &= (J-3/2)(J+5/2), & Z &= (J-1/2)(J+3/2) \\ M &= J + 3/2, \quad \text{for f-sublevels}, & M &= -(J-1/2), \quad \text{for e-sublevels}. \end{aligned}$$

The interaction parameters α, β, η and ξ are given in [77] and listed in table C.3.4. Interactions between different vibrational levels of the states can be neglected due to the large energetic distance amongst them [68]. Plugging in the respective constants and interaction parameters, which are listed in table C.3.1, C.3.2 and C.3.3 in the appendix, yields two matrices, one for e-parity sublevels and one for f-parity sublevels. Diagonalisation of the two matrices gives then the corresponding eigenenergies for the different states. In figure 2.5 the calculated values for a direct transition from the X $^2\Pi$ state to the H $^2\Sigma^+$ state are compared to a large set of measured data given in [78]. The energy values are given with respect to the X $^2\Pi_{1/2}$ $J = 1/2$ level. The ground state energies which are needed to calculate the different branches were calculated like described in section 2.2.1 for the calculation of the Λ-type doubling. The agreement between calculation and the plotted data is excellent.

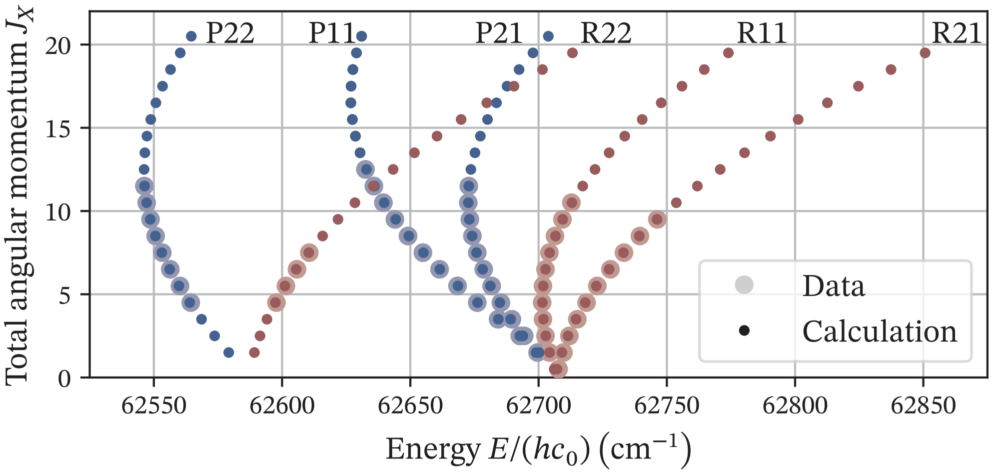

Figure 2.5: Comparison of calculated and measured data for the energy levels of the $\mathrm{H}\,^2\Sigma^+$ state with respect to the lowest rotational state $\mathrm{X}\,^2\Pi_{1/2}$ $J_X = 1/2$. The branches are those of the direct transition from the $\mathrm{X}\,^2\Pi_{1/2}$ to the $\mathrm{H}\,^2\Sigma^+$. The measured data was retrieved from [78].

2.2.3 Excitation to high lying Rydberg states of nitric oxide

The excitation to high lying Rydberg states from the $\mathrm{H}\,{}^2\Sigma^+$ state should allow the excitation of p,d and f states due to the d-character of the excited electron in the $\mathrm{H}\,{}^2\Sigma^+$ state. However, since the $\mathrm{H}\,{}^2\Sigma^+$ state has also partial s-character transitions into s-states may also be possible. The excitation targets Rydberg states of the lowest Rydberg series converging to the ground state of the resulting cation NO^+. However, the exact assignment of principle quantum numbers is not yet possible but subject of ongoing research on the presented excitation scheme [81]. As this thesis focuses on high resolution spectroscopy on the lowest transition in the excitation scheme and on the general implementation of the Rydberg excitation, precise knowledge on the addressed Rydberg states is at this point not necessary.

2.3 Optogalvanic spectroscopy

As described in the beginning, optogalvanic spectroscopy is the basic principle used to realise a new type of gas sensor for nitric oxide as explained in the introduction. The working principle of this technique is illustrated in figure 2.6.

Pure nitric oxide or a mixture of nitric oxide and one or several background gases flow continuously through the spectroscopy cell. The cell is equipped with electrodes which are later needed to retrieve the generated signal. The electrode configuration inside the cell is depicted in a very simplified way in figure 2.6. Since the electrode design may directly influence the measured signal it has been subject to investigation [82].

The process of generating the signal can be explained in three steps. These steps usually take place continuously and at the same time.

The first step is designated “Excitation” and shown on the top left of figure 2.6. Gaseous nitric oxide shown in red and blue and a background gas, for example nitrogen, shown in grey flow through the cell. The nitric oxide in the mixture is excited to a Rydberg state by continuous wave laser systems. The corresponding excitation scheme has been explained in section 2.2 and is depicted in the top center of

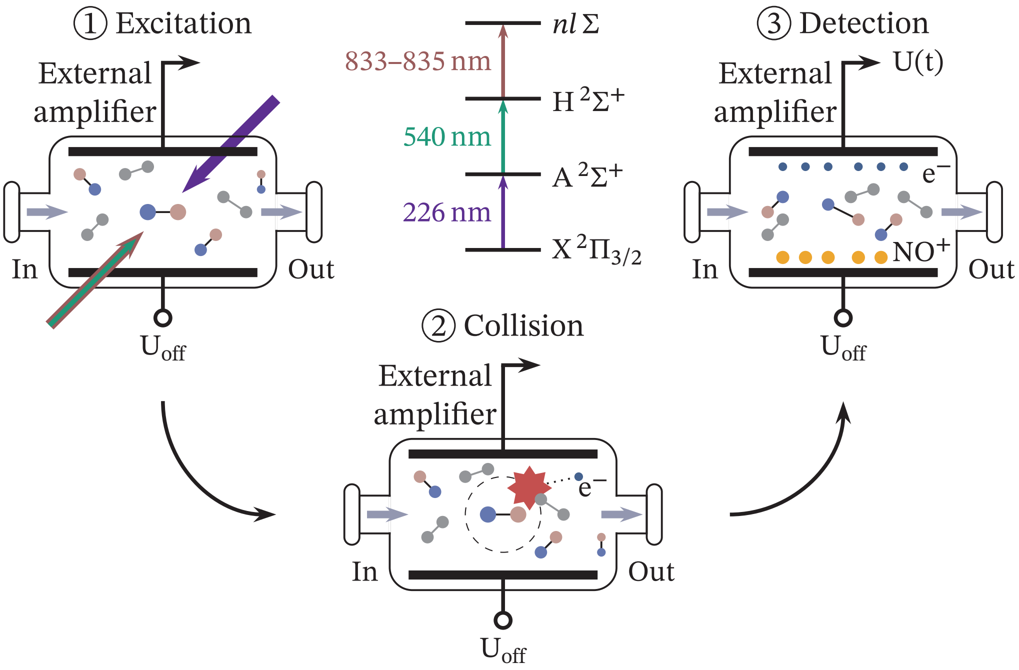

Figure 2.6: Schematic of the working principle of the optogalvanic spectroscopy which can be used for gas sensing as explained in the introduction. The three steps "Excitation", "Collision" and "Detection" happen simultaneous but are depicted separately for clarity.

figure 2.6. The laser beams are set up in such a fashion that the two longer wavelengths are counter-propagating with respect to the UV-beam. In the second step, “Collision”, the excited Rydberg molecules collide with the background gas or other nitric oxide molecules. The Rydberg electron is so weakly bound that the collisional energy is high enough to ionise the molecule. This process generates charges inside the cell. The generated charges have to be retrieved to generate a signal. This is the last step: “Detection”. To retrieve the charges from the cell a small potential has to be applied to the electrodes, so that the charges are separated and collected by the respective electrode. One electrode is connected to a transimpedance amplifier, so that the current generated by the retrieved charges can be amplified and converted to a voltage signal U(t).

In fact, this method is not limited to Rydberg states. Charges are already generated if only the first transition of the excitation scheme is driven [71]. However, as explained in [71] the ionisation mechanism is different. For the employment of this spectroscopy technique for sensing applications the Rydberg excitation is crucial, since it generates larger currents and increases the selectivity of the proposed sensing scheme [10]. The application of this technique as a sensing scheme has been investigated in a proof of concept study [9] and demonstrated in a model system [6]. The three photon excitation has been demonstrated and analysed in [8, 71]. The usage of an external amplifier has the disadvantage that it may pick up additional noise by the cables connected to the readout electrodes. It is in principle possible to use on-board amplifiers which are directly put onto the spectroscopy cell [83]. However, this requires a more elaborate electronic design and special fabrication techniques for the corresponding cell. This is subject of ongoing research (F. Munkes, PhD Thesis, in preparation) and will not be further discussed here.

2.4 Doppler-free absorption spectroscopy

Optogalvanic spectroscopy can be applied for gas sensing and is very useful for the spectroscopy of higher lying excited states particularly Rydberg states were the generated current gives a large signal. However, to resolve the hyperfine structure of a given transition or state, optogalvanic spectroscopy provides not the necessary resolution. To resolve the hyperfine structure Doppler-free saturated absorption spectroscopy can be employed. This technique allows a resolution well below the Doppler width by using two counter propagating laser beams. In this section first Doppler broadening will be briefly discussed before Doppler-free saturation spectroscopy is explained. The explanations follow [37].

2.4.1 Doppler Broadening

Doppler broadening is an inhomogeneous broadening mechanism that results from the thermal movement of atoms or molecules interacting with the laser. A more detailed treatment can be found in [37]. The effect is exactly the same for atoms and molecules. Even though in the following explanation the term molecule will be used exclusively.

The thermal movement of molecules leads to a frequency shift of the absorbed laser light which depends on the velocity v of the molecules with respect to the laser beam. Movement of a molecule towards the laser beam will result in a blue shift of the laser light in the rest frame of the molecule. For movement away from the laser beam the laser light is shifted to the red. Qualitatively, the effect is analogous to the Doppler effect experienced for sound waves. For a laser beam of frequency ω_L the frequency shift in the reference frame of a moving molecule is given by

$$\omega_\mathrm{Red} = \omega_\mathrm{L} - kv, \qquad \omega_\mathrm{Blue} = \omega_\mathrm{L} + kv. \tag{2.7}$$

Only the velocity component along the wave-vector $\mathbf{k}$ is contributing to the Doppler shift. For simplicity the problem is treated in one dimension, so that the scalars k and v can be used. Consequently $(\omega - \omega_0)/\omega_0 = v/c$ holds with the resonance frequency ω_0 in the rest frame of the molecules.

The velocities in an ensemble of thermal molecules are Maxwell-Boltzmann distributed, thus not all the molecules have the same velocity. The corresponding velocity distribution is given by [37]

$$f(v)\mathrm{d}v = \sqrt{\frac{m}{2\pi k_B T}} \exp\left(-\frac{mv^2}{2k_B T}\right)\mathrm{d}v. \tag{2.8}$$

Here, m the mass of the molecules, k_B is the Boltzmann constant and T the temperature.

From the thermal distribution and the relation between frequency and velocity the line-shape function can be derived. It is Gaussian and given by [37]

$$g_\mathrm{D} = \frac{c}{\omega_0} \cdot \sqrt{\frac{m}{2\pi k_B T}} \exp\left(-\frac{mc^2}{2k_B T}\left(\frac{\omega - \omega_0}{\omega_0}\right)^2\right). \tag{2.9}$$

The corresponding frequency shift of the laser in the reference frame of the molecule, can then be calculated from the full width at half maximum of equation 2.9 and is

$$\Delta\omega_D = \frac{\omega_0}{c}\sqrt{\frac{8\log(2)k_B T}{m}}. \tag{2.10}$$

From equation 2.10 one can deduce that heavier atoms or molecules will allow narrower linewidth than lighter atoms or molecules. Nitric oxide has a mass of only 30 u [66]. Plugging in the corresponding numbers for the ground state transition at roughly 226 nm and a temperature of 293 K results in a Doppler broadening of $\omega_{226} \approx 2\pi \times 3\,\mathrm{GHz}$. This has been experimentally confirmed during investigations on different transitions between the $\mathrm{X}\,^2\Pi_{1/2}$ and $\mathrm{A}\,^2\Sigma^+$ state with our narrow band continuous wave laser system [7].

2.4.2 Saturated absorption spectroscopy

To understand the working principle of saturated absorption spectroscopy the absorption cross section for Doppler broadening is required. The following derivation summarises the work of [37]. First, it is necessary to take into account that the absorption of a molecule at rest is not arbitrarily sharp but has a certain minimum linewidth Γ also denoted as natural linewidth or decay rate. Γ broadens the absorption line homogeneously, thus affects every molecule in the same way. The corresponding line shape function is Lorentzian. The absorption coefficient $\kappa(\omega)$ is given by [37]

$$\kappa(\omega) = \int N\sigma(\omega - kv)dv. \tag{2.11}$$

It depends on the number density of the molecules which is denoted as $N(v)$ and the absorption cross section $\sigma(\omega - kv)$. Plugging in the Lorentzian absorption line shape and the number density yields [37]

$$\kappa(\omega) = \frac{g_2}{g_1}\frac{\pi^2 c^2}{\omega_0^2} A_{21} N \int f(v) \frac{\Gamma/(2\pi)}{(\omega - \omega_0 - kv)^2 + (\Gamma^2/4)}. \tag{2.12}$$

The Gaussian function $f(v)$ here is convoluted with the Lorentzian line shape function. The convolution of a Gaussian and Lorentzian function results in a line shape profile denoted as Voigt profile. However, the Doppler width is in almost any case way larger then the Lorentzian linewidth Γ. Only for low temperatures this does not hold true. Therefore, it is possible to treat the Lorentzian absorption line shape in the integral as a Dirac delta function with argument $\omega - \omega_0 - kv$. The result of the integration is, that the integral turns into g_D. The Doppler broadened absorption cross section is then identified as [37]

$$\sigma(\omega) = \frac{g_2}{g_1}\frac{\pi^2 c^2}{\omega^2} A_{21} g_D(\omega) \tag{2.13}$$

The two factors g_2 and g_1 take into account the degeneracy of the two involved states. Thus if a state is non-degenerate $g_i = 1$ holds. A_{21} is the Einstein-A coefficient for spontaneous emission.

Now, that the absorption cross section for a Doppler broadened transition has been introduced, the technique of saturated absorption spectroscopy can be explained. This exploits the physical principle that absorption cannot increase limitless but will saturate for a certain laser intensity [37]. Assume again two states with number densities $N_1(v)$ for the lower and $N_2(v)$ for the higher energy level. The difference in population between the two levels will not change much as long as the laser intensity stays low enough. The majority of the molecules will be in the lower state. However, if the laser intensity equals the saturation intensity or is at least close to saturation, the difference in the number density is high enough that $N_1(v) \approx N(v)$ is not valid any more. Henceforth, equation 2.11 changes to

$$\kappa(\omega) = \int (N_1(v) - N_2(v))\sigma(\omega - kv)dv. \tag{2.14}$$

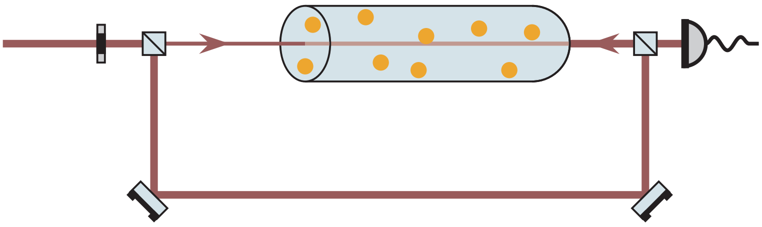

Figure 2.7: Schematic of the working principle of Doppler-free saturated absorption spectroscopy. The laser beam is divided into two beams which are sent through the sample counter propagating. The probe beam is depicted with half the linewidth of the pump beam. As a detector a photodiode is usually sufficient.

The change in the absorption coefficient can be probed by a laser beam with considerably less intensity than the saturation intensity. Saturated absorption spectroscopy therefore uses two laser beams of the same laser source. A simplified scheme of the experimental setup is depicted in figure 2.7. The laser beam is split into two beams which need to be overlapped in the cell containing a gas of molecules. The best results are achieved when both beams overlap perfectly. One of the two beams has to be set to an intensity close to the saturation intensity, it is denoted as pump beam and will change $\varkappa(\omega)$ as discussed previously. The second beam has to be considerably weaker in intensity than the pump beam and is denoted as probe beam.

The pump beam basically burns a hole in the population density $N_1(v)$ of the lower states. The probe beam does also excite some of the particles in the cell to the excited state but only few compared to the pump beam. The situation is illustrated in figure 2.8. Since both laser beams have the same frequency molecules with a velocity component along the optical axis will experience different Doppler shifts for the two beams, i.e. absorb different frequencies. This is depicted in column (a) and (c) of figure 2.8. However, for molecules that do not move or that have only velocity components that are perpendicular to the optical axis both laser beams are absorbed at the same frequency. Here the probe laser will sense the change in the optical absorption coefficient. The absorption of the probe laser is reduced due to the large amount of molecules that are excited by the pump laser. The reduced absorption of the probe laser leads to a dip with Lorentzian line shape within the Doppler broad-

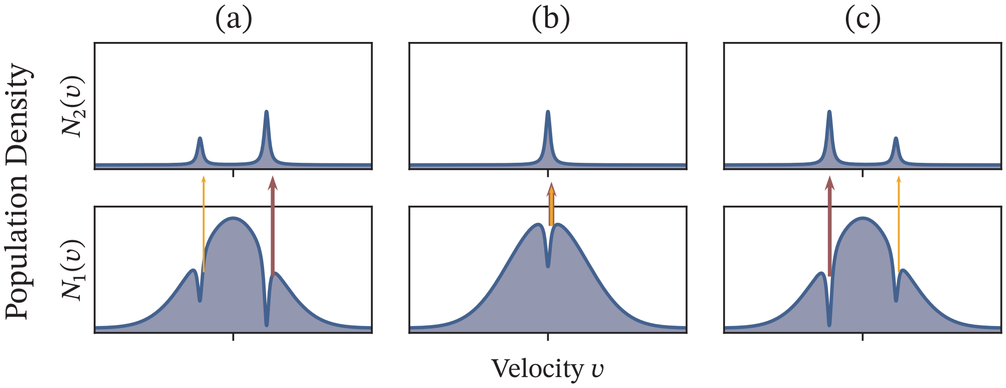

Figure 2.8: Schematic of the effect of the pump beam drawn in red and the probe beam drawn in yellow on the population densities $N_1(v)$ and $N_2(v)$ of the ground and excited state in a two level system. After [37].

ened line. These dips are named Lamb-dips. The width of the Lamb-dips depends on the homogeneous broadening mechanisms such as the natural linewidth, power and pressure broadening. Saturated absorption spectroscopy is an ideal tool to directly resolve hyperfine transitions that would otherwise be hidden in the Doppler broadened linewidth. Doppler free saturated absorption spectroscopy can be applied to a multitude of different atoms and molecules as long as narrow band lasers are available for the respective transition [84–87].

If there are two adjacent transitions with a common ground state but different excited states and the separation between the transitions is less than the Doppler width, so called crossover resonances occur. Assume the population density of the second excited state to be $N_3(v)$. If the pump beam is on resonance with the transition from the ground state to the second excited state it will burn a hole in the ground state population $N_1(v)$ by increasing the population density $N_3(v)$. If at the same time the probe laser is on resonance with the other transition i.e. increasing $N_2(v)$, its absorption will decrease because it is only sensitive to changes in the population of the ground state. The situation were the pump and probe laser are on resonance with two different transitions corresponds to the two lasers being absorbed by different velocity classes. The problem is strictly symmetric, thus the crossover resonance will appear exactly in the middle between the two actual transitions [37]. This usually allows to easily identify crossover resonances in a spectrum.

2.4.3 Additional broadening effects

In addition to the homogeneous broadening Γ denoted as the natural line width and the Doppler broadening further broadening effects occur. Namely these are transit time broadening, pressure broadening and power broadening. A short summary of these effect is given here. More detailed information is given in textbooks like [37, 88, 89].

Transit time broadening is sometimes also referred to as time-of-flight broadening. It takes into account that the interaction time of a molecule with the laser is finite. Due to their thermal movement molecules or atoms typically will not stay in the volume illuminated by the laser beam. The resulting broadening is given in [89] and is

$$\Gamma_T = \frac{4\bar{v}(T)}{d}\sqrt{2\log(2)}. \tag{2.15}$$

Here, d is the diameter of the laser beam and $\bar{v}(T)$ is the mean thermal velocity which can be derived from the Maxwell-Boltzmann distribution, given in equation 2.8, by calculating its expectation value. It is given by

$$\bar{v}(T) = \sqrt{\frac{8k_BT}{\pi m}}. \tag{2.16}$$

Here, m is the mass of the molecule, T the temperature and k_B the Boltzmann constant.

Pressure broadening is often also referred to as collisional broadening. Collisions between particles lead to a decrease in the lifetime of the excited state, since they may induce transitions to the ground or other excited states. The corresponding decay rate can be estimated from the mean free velocity of the particles which is given in equation 2.16 [89]

$$\Gamma_{\text{Press}} = N\sigma\bar{v} \tag{2.17}$$

Here, N is the number density of the respective particle and σ the collisional cross section.

The last of the listed broadening mechanisms is power broadening. The reason for this mechanism is that if a transition is saturated the absorption near resonance is reduced but does only change slightly further away from resonance [37]. If power broadening is taken into account the full width half maximum of the absorption coefficient $\kappa(\omega)$ changes. It is given by [37]

$$\Delta\omega_{\text{FWHM}} = \Gamma\left(1 + \frac{I}{I_{\text{Sat}}}\right). \tag{2.18}$$

Here I is the laser Intensity and I_{Sat} the saturation intensity which is also given in [37] and depends on Planck's constant h, the wavelength of the radiation Λ and the life time of the excited state $\tau = 1/\Gamma$

$$I_{\text{Sat}} = \frac{h\pi c}{3\lambda^3\tau}. \tag{2.19}$$

However, this relation for the saturation intensity is idealised. In practice, the decay rate Γ is not only the natural linewidth of the transition but rather an effective decay Γ_{Eff} rate that includes the contributions of the additional broadening effects like for example the previously introduced pressure broadening. Thus, it can be written as

$$I_{\text{Sat}} = \frac{h\pi c}{3\lambda^3\tau} \approx \frac{h\pi c\Gamma_{\text{Eff}}}{3\lambda^3} \tag{2.20}$$

3 Laser setup and frequency stabilisation

Introduction

This chapter briefly introduces the laser systems that were employed for the spectroscopy of nitric oxide. In addition, the necessary frequency stabilisation setup is explained that is used to lock these different lasers. The stabilisation of the laser systems is crucial for reliable and reproducible optogalvanic measurements. Furthermore, the presented locking setup enables precise scanning of the UV-laser considerably increasing the signal to noise ratio and quality of the spectra.

In section 3.1 the individual laser systems are presented and their specifications summarised. In section 3.2 a brief introduction to the employed locking technique is given, followed by a description of its implementation and the key features of the setup. The chapter concludes with an estimation of the performance of the lock setup for the $\mathrm{A}\,^2\Sigma^+ \leftarrow \mathrm{X}\,^2\Pi$ transition.

3.1 Laser systems

3.1.1 Frequency-quadrupled Ti:sapphire laser

The first excitation is in the deep UV which is a difficult wavelength to generate. It requires at least one stage of frequency-doubling. One way to generate such extreme

UV-wavelengths are frequency doubled dye lasers, which were subject to active research back in the 1970s [90, 91]. Even nowadays many experiments concerned with the excitation of nitric oxide rely on frequency-doubled dye laser systems [92–95]. These dye laser systems have the advantage of high total powers and robustness. However, they come with a large drawback. They are usually pulsed, typically operating with micro- to nano second pulses. If a laser pulse is very short in the time domain it has a broad frequency distribution. This follows from its limited time-bandwidth product that can be derived with Fourier analysis. For the application as a gas sensor and therefore for optogalvanic spectroscopy as introduced in section 2.3, a narrow band laser excitation is necessary to ensure a high selectivity. Furthermore, to perform Doppler free saturated absorption spectroscopy (see section 2.4), the laser linewidth has to be lower than the Doppler width of the spectroscopic feature. Therefore, pulsed dye lasers are not suitable for the experimental techniques employed within the scope of this work.

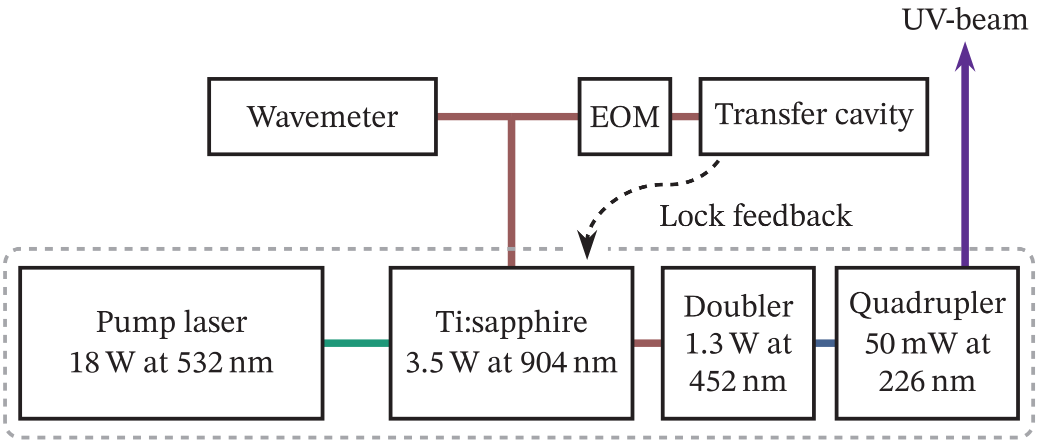

Figure 3.1: Schematic of the UV-laser and its stabilisation setup. A detailed explanation on how the laser frequency stabilisation works is given in section 3.2

Figure 3.1 gives a schematic overview on the narrow band continuous wave UV-laser system employed in the optogalvanic and Doppler-free measurements discussed in this thesis. The dashed frame shows the parts belonging to the commercially available UV-laser system. Here, a frequency doubled diode pumped solid state laser (DPSS laser) is emitting light at 532 nm with a maximum power of 18 W. This laser is used to pump a Ti:sapphire laser emitting at least 3.5 W single mode at 904 nm. The emitted light is mainly send to the doubler which is a ring cavity build around a lithium triborate (LBO) crystal which is used to frequency double it to 452 nm. The doubler typically yields up to 1.3 W at this wavelength. The blue light from the doubler is sent to the quadrupler which contains another ring cavity using beta barium borate (BBO) to double the frequency for a second time. This yields, if the cavity is well adjusted, an output of 50 mW at 226 nm. Additional information on the UV-laser system can be found in [7].

To tune and frequency stabilise the system, a small fraction of the light emitted by the Ti:sapphire laser is sent to a wavemeter and coupled into an electro-optic modulator (EOM). The EOM adds radio frequency sidebands which are used to lock the laser to a transfer cavity which can also be employed as a relative frequency reference if the laser is scanned. The lock setup is discussed in more detail in section 3.2.2. The short term linewidth of the laser (3 ms) is specified by the manufacturer to be 50 kHz in the fundamental, thus 200 kHz in the UV.

Since the full spectrum of the $A\,^2\Sigma^+ \leftarrow X\,^2\Pi$ transition in NO is spread over a range of roughly 4 nm from 224 nm to 228 nm, the system benefits from the large tunability of the Ti:sapphire laser. The doubling crystals are cut such that the full spectrum is addressable and only a reoptimisation of the crystal angle and cavity alignment of the doubler and quadrupler are necessary. The maximum mode-hop free scan range of the system around the set wavelength is roughly 20 GHz for the fundamental wavelength.

3.1.2 Frequency-doubled fibre amplifier system

For the second transition from $A\,^2\Sigma^+$ to the $H\,^2\Sigma^+$ state high laser power is necessary to drive the transition. The required wavelength of 540 nm is generated using a self-built frequency doubling setup. An overview of the system is shown in figure 3.2. The individual components of the system are off-the-shelve components. The basis of the system is a continuous wave external cavity diode laser in Littrow configuration. Detailed information on this type of laser system [96] as well as on other commonly used laser systems can be found in [97]. The diode laser runs at

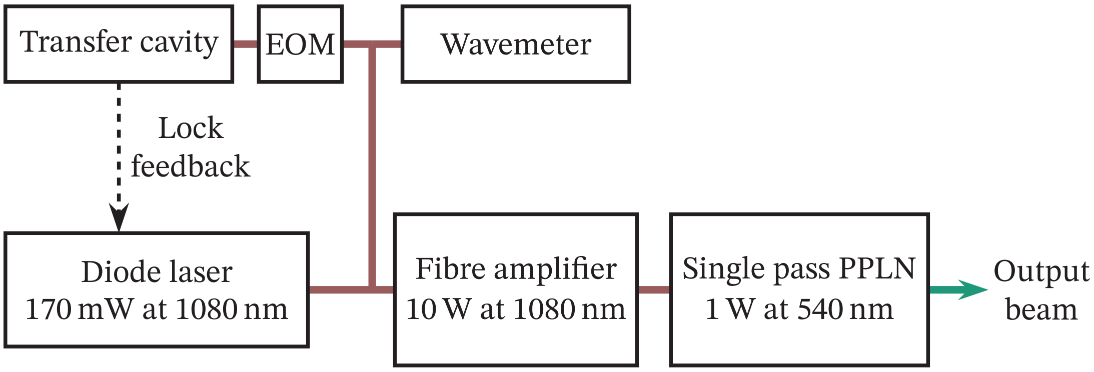

Figure 3.2: Schematic of the laser setup for the $A\,^2\Sigma^+ \leftarrow H\,^2\Sigma^+$ transition at around 540 nm. A detailed explanation on how the laser frequency stabilisation works is given in section 3.2.

around 1080 nm and produces an output power of up to 170 mW at a short time linewidth below 50 kHz. To obtain enough laser power for the frequency doubling the diode laser has to be amplified. This is done by employing an ytterbium doped fibre amplifier capable to amplify laser wavelengths from 1060 - 1090 nm. The maximum output power of the fibre amplifier is 10 W. The amplified laser beam is sent through a periodically poled lithium niobate crystal (PPLN) which is doped with magnesium oxide. The crystal is 25 mm long and used in single pass. It generates a maximum output of 1 W laser power at 540 nm. The crystal is placed in an oven for stabilisation to the required temperature for optimal phase matching. Details on the basic optical setup of this system can be found in [98]. However, it must be noted that the optical setup has changed since its first installation. The beam path has been optimised to add an acousto-optic modulator for power stabilisation and amplitude modulation. Further information on the topic is available in [99] and especially on the optimisation of phase matching in [100]. For the application of optogalvanic spectroscopy for sensing, it is crucial to optimise the excitation path. Therefore, it is beneficial to be able to address several different rotational levels of each of the involved states. The tunability of the fundamental diode laser is specified from 1000 - 1085 nm and may even be extended up to 1090 nm according to the manufacturer. This allows to address a large range of rotational manifolds of the

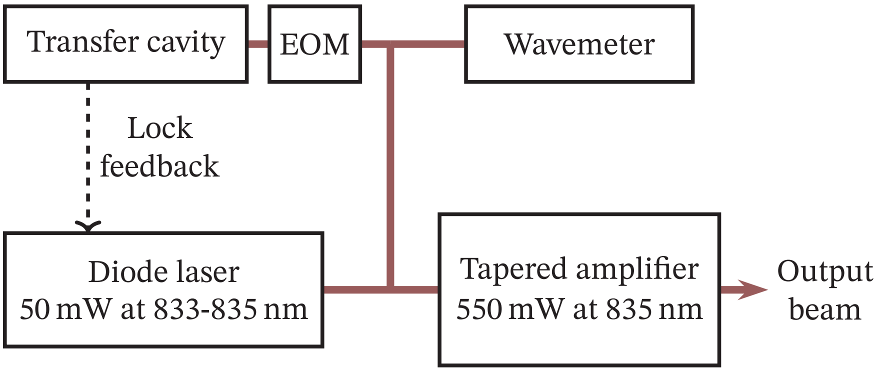

Figure 3.3: Schematic of the tapered amplifier setup employed for the Rydberg excitation. A detailed explanation on how the laser frequency stabilisation works is given in section 3.2.

$H\,^2\Sigma^+$ and $H'\,^2\Pi$ states, since the fibre amplifier and PPLN can also be operated at the required wavelengths.

Like in the case of the UV-laser system, the fundamental laser has to be actively frequency stabilised to obtain long-term frequency stability. This is done in the same way as for the UV-system and depicted in figure 3.2. A small fraction of the 1080 nm laser light is split off and sent to an EOM and transfer cavity, to lock the fundamental laser to this cavity. The rest of the split off light is sent to a wavemeter for coarse wavelength adjustment and wavelength monitoring during the measurements.

3.1.3 Tapered amplifier system

The last transition is at 833 - 835 nm. Since the Rydberg energy levels are very close to each other, even a tuning range of a couple of nano meters allows the excitation of several different Rydberg states. However, the excitation of Rydberg states generally requires higher laser powers, since the wave function overlap between states of low principle quantum number and Rydberg states (i.e. high principle quantum number) is in general small [101]. Consequently, the dipole matrix elements for Rydberg excitation are quite small. The near infrared wavelength range is easily accessible by diode lasers. However, to reach high laser powers the employed diode laser system has to be amplified. This is done using a tapered amplifier system. A schematic of the system is displayed in figure 3.3. The corresponding optical setup is described in [102], but underwent optimisation since its initial comissioning.

The employed continuous wave external cavity diode laser is in principle tunable from 825 - 853 nm. It has a peak output power of around 50 mW. The laser beam is split into two parts. The first part is used as seed laser and coupled into the tapered amplifier system. The system consists of a commercially available tapered amplifier chip mounted on a self-built oven and mounting setup which is based on [103], but has been modified. It allows peak powers of 550 mW. The other part of the laser light is treated to the other laser systems and sent to an EOM followed by a transfer cavity which is used to stabilise the TA's seed laser. A wavemeter is used for coarse wavelength adjustments and monitoring as well.

3.2 Frequency stabilisation of the individual laser systems

Over longer time-scales free running lasers will drift in frequency due to small fluctuations in temperature, current and other external factors. It is therefore crucial to stabilise the frequency of the employed laser systems to the frequencies of the corresponding resonances in the molecule. Especially, the current signal of the optogalvanic spectroscopy depends on the number of molecules excited to the Rydberg state. Comparable measurements are only possible when all laser systems are frequency stabilised.

In this section, the frequency stabilisation setup and the underlying technique will be briefly introduced. In addition, the lock error of the UV-laser is estimated since the frequency uncertainty is needed to evaluate and asses the quantitative spectroscopy data which has been collected (see chapter 6). For the optogalvanic spectroscopy data presented here (see chapter 5), the frequency accuracy is not of importance since the main goal was the general proof that the Rydberg excitation with the presented scheme works and the current detection is possible.

3.2.1 Pound-Drever-Hall technique

For the frequency stabilisation the Pound-Drever-Hall method [104, 105] is used. This technique is similar to frequency modulation spectroscopy [106, 107] and uses a Fabry-Pérot interferometer (FPI) to measure and stabilise the frequency of a laser. The technique will be qualitatively introduced here. This introduction is based on the work of Black [108], where a more detailed and quantitative discussion of the technique can be found.

A very simple way to frequency stabilise a laser system to a Fabry-Pérot interferometer is side-of-fringe locking. Here, the transmission signal of a single cavity fringe is taken and the set-point for the stabilisation is set somewhere (typically around half of the maximum) on the rising or falling slope of the fringe. If the laser frequency changes, the cavity fringe will change its position, due to the resonance condition of the Interferometer. This results in a change of the transmitted laser intensity which will be noticed by the control electronics to give feedback to the laser to counteract the frequency change. This technique is very easy to implement but suffers certain drawbacks. For example the side-of-fringe technique is sensitive to power fluctuations of the laser too. Thus, the control electronic will react to changes in laser power as if the laser frequency would change. It is obvious that this will disrupt the overall frequency stability of the system. A possible solution to this problem is to stabilise the light reflected from the cavity to zero. However, the reflected signal is strictly symmetric. Henceforth, the control electronics will not recognize in which direction the laser frequency drifts away from resonance and can therefore not counteract appropriately. The solution to this problem is to stick with the reflected signal but to measure its first order derivative which is antisymmetric with respect to the resonance.

The Pound-Drever-Hall technique uses a small sinusoidal modulation of the laser frequency to measure the derivative of the reflected signal. This is achieved by comparison of the change in the reflected intensity to the modulation applied to the laser. At frequencies above the resonance frequency the derivative of the reflection is positive and the intensity change due to the modulation will be in phase. On the lower frequency side of the resonance the derivative is negative. As a consequence it will react 180° out of phase with respect to the modulation. On resonance the derivative is zero. Conclusively, the comparison between the modulation frequency and the reaction of the reflected intensity to it, allows it to determine the direction the laser is drifting to and enables the control electronics to counteract appropriately.

This qualitative explanation of the Pound-Drever-Hall technique holds only true if the modulation frequency is low. What the model ignores is that cavities in general require a build up time, thus the light has to make a few round trips through the cavity to build up the signal. To entirely understand the Pound-Drever-Hall technique a quantitative model is necessary. This model is presented in detail in [108] and it is stated that for faster modulation frequencies the technique yields an even better noise performance and higher bandwidth then for smaller modulation frequencies. The exemplary error signal depicted in figure 3.5 is of the form that is obtained for fast modulation of the laser. For slow modulation the signal looks different (see [108])

In terms of the technical realisation modulating the laser frequency is usually more difficult to achieve than modulation of its phase [108]. In section 3.1.1 - 3.1.3 it was explained that all fundamental lasers are coupled into an EOM before they are coupled into the respective transfer cavities. Those EOMs are used to modulate the phase of the lasers to generate the respective Pound-Drever-Hall error signal. Phase modulation results in sidebands on the cavity fringes of the laser which appear at $\omega_\mathrm{L} \pm \omega_\mathrm{Mod}$ when ω_L is the laser frequency and ω_Mod the frequency of the phase modulation. The demodulation and generation of the error signal can be achieved by feeding the modulation signal and the measured signal of the reflection from the interferometer to a mixer. By adjusting the phase of one of the two input signals, the dc-part of the signal which corresponds to the configuration were both input signals of the mixer have the same frequency can be retrieved using a low-pass filter. This dc-part of the signal is the characteristic Pound-Drever-Hall error signal.

3.2.2 Implementation

In this section the implementation of the Pound-Drever-Hall technique for the employed laser systems is explained. Figure 3.4 shows schematically how the reference

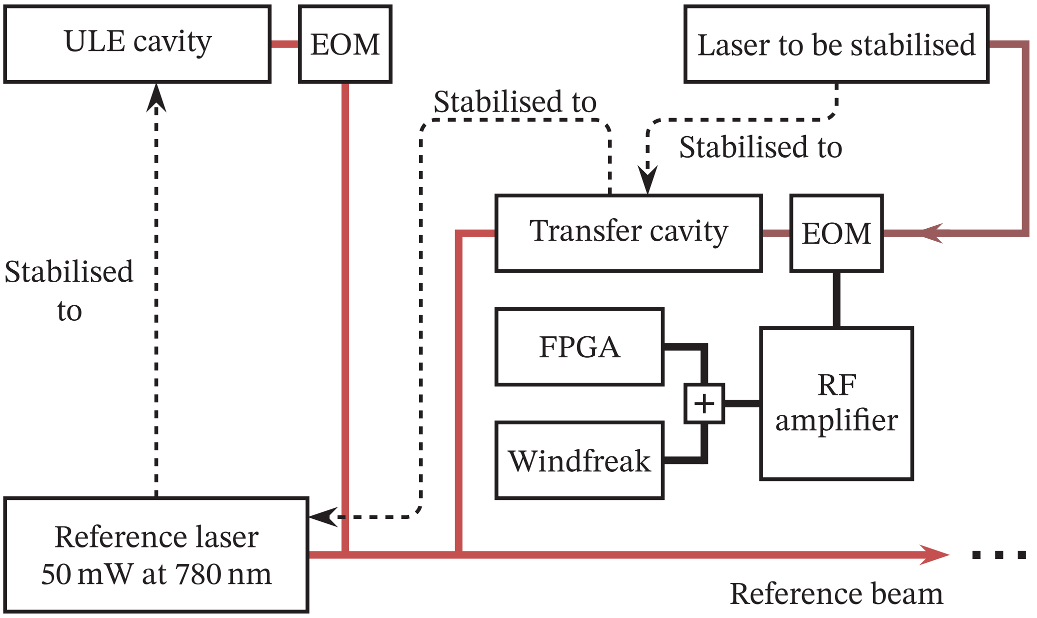

Figure 3.4: Schematic example of a transfer lock as it is realised for the different laser systems for the Rydberg excitation of nitric oxide. The reference beam is distributed to several transfer cavities.

laser is locked and distributed to the transfer cavities. The scheme shows only a single transfer cavity. As already explained in sections 3.1.1 - 3.1.3 each laser is sent to its own transfer cavity but all transfer cavities are stabilized to the same reference laser. As control electronic the PID controller of the "Red Pitaya" FPGA boards (STEMlab 125-14) are used. The full setup employs a large number of those FPGAs to stabilise all the lasers and cavities. The reference laser is a diode laser running at 780 nm and produces around 50 mW laser power. A Doppler-free saturated absorption spectroscopy setup with rubidium is set up for this laser so that the spectrum of the rubidium D2-line can in principle be used as an absolute frequency reference. This part of the setup is omitted in figure 3.4. The reference laser is separated into two beams. The first one is sent to an EOM and then coupled into an ultra-low expansion (ULE) cavity with a free spectral range of 1.5 GHz. The reflection of the ULE-cavity is then used to lock the reference laser. To keep this lock as stable as possible, the ULE-cavity is placed in vacuum and actively kept at a temperature of 35 °C. At this temperature the derivative of the thermal expansion coefficient of the cavity is zero. The EOM used for the reference laser allows it to lock the laser on a fringe generated by the EOM instead of locking it to a cavity fringe. Henceforth, the lock position of the reference laser is more flexible and can be shifted if necessary. The radio frequency sidebands added to the reference laser are directly added to the laser via the ac-input of the laser head.

The second part of the reference laser is distributed to the different transfer cavities to lock those cavities to the stabilised lasers. The transfer cavities are based on the design developed within the scope of [109] and have been characterised and tested in another work [110]. The original cavity design has been altered to fit to the needs of the experiment. The free spectral range is different for each of the transfer cavities due to the individual assembly. However, in general it is between 850 MHz and 950 MHz. The finesse of this type of cavity is around 200 [110]. The free spectral range can be experimentally determined using either radio frequency sidebands modulated to a laser at a known frequency or by using the rubidium hyperfine spectrum as a frequency reference. The transfer cavities have a low voltage piezo which is used to adjust the position of the planar mirror of the cavity. The piezo can be used to scan the cavity and also to lock the cavity length. Its resonance frequency is at around 85 kHz and the bandwidth of the lock of the transfer cavities is below 1 kHz. Keeping in mind that the main source of length instability is thermal drift due to small temperature fluctuations. Additional contributions result most likely from air pressure variation which also happen on a slow time scale. The lock uses the same rf-sidebands as used for the stabilisation of the reference laser.

The fundamental beams of the other lasers also need rf-sidebands. However, since these sidebands may prove problematic during the actual spectroscopy they are not directly added to the laser. To create the sidebands a phase-modulating EOM is employed as depicted in figure 3.4 and the schematics of the laser setups. The EOM is used to not only modulate rf-sidebands at $\omega_{\mathrm{PDH}} = 2\pi \times 15\,\mathrm{MHz}$ for the Pound-Drever-Hall lock but also additional sidebands that can be tuned between $\omega_{\mathrm{Lock}} = 2\pi \times 35\,\mathrm{MHz}$ and roughly $2\pi \times 500\,\mathrm{MHz}$. This is implemented as depicted in figure 3.4. The Red Pitaya FPGA board generates the 15 MHz sidebands for the Pound-Drever-Hall lock. The “Windfreak” radio frequency generator (SynthUSBII) is a commercially available product which can generate radio frequencies in a range from 34 MHz to 4.4 GHz. The two frequencies are added with a power combiner and fed to a radio frequency amplifier which is connected to the rf-input of the EOM. The limitation to a maximum frequency of 500 MHz is due to the capability of the employed amplifier. However, the setup is fully sufficient in this form. The second set of sidebands is necessary for being able to lock the laser at any desired frequency. Without the additional higher frequency sidebands an error signal would only be available at the position of the cavity fringes. The additional sidebands enable the generation of an error signal at any frequency in between two cavity fringes, so that the laser can be directly locked to a spectroscopic resonance even if the resonance does not coincide with a cavity fringe. Additionally, locking the laser on a fringe that was generated by the EOM allows it to optimise the frequency position after the lock was applied. In terms of the optogalvanic spectroscopy this can be used to shift the laser exactly onto the maximum of the resonance of a corresponding transition by carefully fine tuning the EOM frequency.

3.3 Lock error estimation for the ground state transition

For the optogalvanic spectroscopy the frequency uncertainty of the locks is, at the current stage of the experiment, not of particular importance. However, the goal of the saturated absorption spectroscopy performed on the ground state transition was to obtain information about the hyperfine structure and the line splittings between individual hyperfine transitions. Therefore the frequency stability of the locking system for the $\mathrm{A}\,^2\Sigma^+ \leftarrow \mathrm{X}\,^2\Pi$ transition has to be estimated.

The first component is the stability of the reference laser. Since this system is used by several experiments it has been optimised and characterised within the scope of [111]. The linewidth of the stabilised system was determined to be $\Delta f_{\mathrm{Reference}} = 121.1\,\mathrm{kHz}$. For the transfer cavity and lock of the Ti:sapphire laser the frequency stability is estimated by extracting a scaling factor from the slope of the Pound-Drever-Hall error signal. This allows to estimate the frequency uncertainty from the root

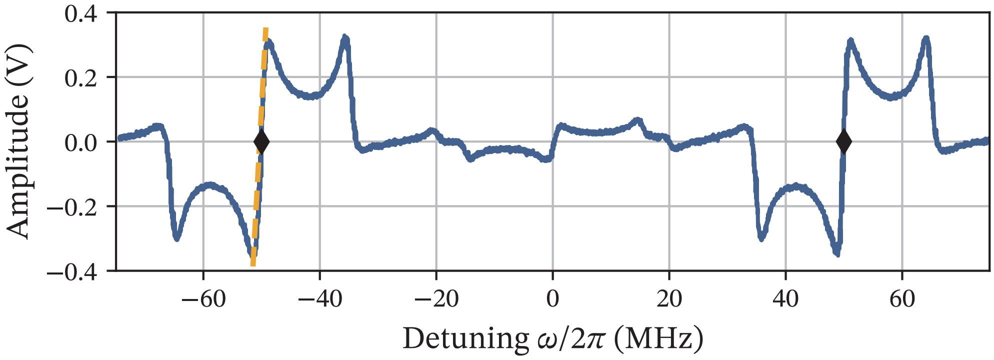

Figure 3.5: Pound-Drever-Hall error signal of the Ti:sapphire laser. The two black diamonds mark the position of the sidebands with frequency ω_{Lock}. The orange line indicates the slope of the error signal which was fitted to obtain a scaling factor for estimating the frequency uncertainty.

mean square of the error signal which is fed to the PID-Controller when the laser is locked. Figure 3.5 shows the Pound-Drever-Hall error signal for the Ti:sapphire laser. The additional sidebands were set to $\omega_{\text{Lock}} = 2\pi \times 50\,\text{MHz}$. Their positions are marked by black diamonds in figure 3.5 and were used as frequency reference. In the center at zero detuning the actual cavity fringe is producing a smaller error signal. It is strongly suppressed because of the large modulation amplitude of ω_{Lock}. The laser can be locked on either the left or the right sideband. The dashed orange line marks the slope of the left error signal. To estimate the lock error the absolute value of the slopes of the error signal are determined by a linear fit. The average value for the two slopes at ω_{Lock} is then inverted yielding a scaling factor in MHz/V. If the laser is locked, the error signal that is fed to the PID is a flat line. However, there is noise on that flat line which resembles the leftover frequency uncertainty. Taking the root-mean square of the error signal's amplitude in Volts and multiplying it by the scaling factor yields an estimated value for the frequency uncertainty.

For the UV-transfer cavity the estimated frequency uncertainty is $\Delta f_{\text{Transfer904}} = 229.9\,\text{kHz}$, while for the laser itself it is $\Delta f_{\text{Ti:sa}} = 202.6\,\text{kHz}$. To obtain the total frequency error these values have to be added up correctly. The lock of the reference laser on the ULE cavity can be considered to be independent of both other locks, since the ULE cavity is thermally isolated and actively temperature stabilised in contrast to the transfer cavity. However, the lock of the transfer cavity's piezo and Ti:sapphire laser can not be considered to be fully independent of each other. Problems or fluctuations from the piezo lock may be transferred easily onto the lock of the Ti:sapphire laser. Therefore, these two errors are added up first and are then added geometrically with the error of the reference lock. The respective total error for the UV-Laser is then given by

$$\Delta F_{\mathrm{Total}} = 4 \times \sqrt{(\Delta f_{\mathrm{Ti:sa}} + \Delta f_{\mathrm{Transfer904}})^2 + \Delta f_{\mathrm{Reference}}^2} \approx \pm 1.8\,\mathrm{MHz}, \tag{3.1}$$

where the additional factor four takes into account the frequency quadrupling of the fundamental laser.

4 A gas mixing unit for nitrogen and nitric oxide

Introduction

In section 2.3 optogalvanic spectroscopy was introduced and it was explained that this technique has the capability to be used for gas sensing. For testing a sensor principle and determining its detection limit it is necessary to produce gas mixtures of well known compositions. In the related proof of concept study [9] the way the gas mixtures were prepared, limited the determination of the detection limit to around 10 ppm.

The test mixture should be composed of NO and N_2 since the latter is the main component of human and animal breath. Of course this is only a very course simulation of human breath but it allows to investigate the technique without the potentially disturbing influence of oxygen, water and the multitude of organic components that can be found in very small concentrations in human breath [112]. After those initial tests real breath samples have to be investigated to check for cross-sensitivities and quantify the influence of the aforementioned potentially disturbing substances.

In addition, the setup allows the precise control of the flow of gas to the experiment. This is advantageous to control the pressure in the spectroscopy cell and perform measurements at comparable parameters. Since the pressure in the cell is directly correlated to the density of the gas it is assumed to have significant influence on the number of charges generated due to collisional ionisation. Thus, the system enables also the exact optimisation of the pressure for different cell sizes and geometries.

This chapter starts with a short introduction on how to treat gases and their flow dynamics, introducing the Knudsen and Reynolds number with respect of their relevance in planning the setup in section 4.1 - 4.2. Subsequently, the gas setup itself is discussed in section 4.3. Here, each part of the setup is explained in more detail starting with the safety aspects for dealing with a toxic and corrosive gas like NO (section 4.3.1), followed by the mass flow controllers, pipe and valve system and finally the pump and Choke system (sections 4.3.2-4.3.4).

4.1 Basic concepts for the description of gases

Kinetic gas theory is an area of physics which describes the properties of gases by consideration of the movement of the individual gas particles, which are atoms or molecules, and their interaction due to collisions [113]. The ideal gas law and the Van-der-Waals equation are two simple models to describe gases which were developed within the frame of the kinetic gas theory.

4.1.1 The ideal gas law

The ideal gas law is a simple model description for gasses. Several assumptions are made which result in an equation of state for gases.

For the ideal gas law it is assumed that the particles of the gas, which are either molecules or atoms, act like hard spheres and that they can be treated as point masses. Consequently collisions between gas particles or the gas particles and the walls of a surrounding environment are assumed to be fully elastic, thus conserving kinetic energy. The velocities of the gas particles are assumed to be Maxwell Boltzmann distributed, with mean thermal velocity $\bar{v}$. The distribution of the velocities with respect to the directions in space is isotropic. Otherwise the pressure would not be a spatially isotropic property. Linking the pressure p to the mean kinetic energy of all particles in a given Volume V and introducing the absolute temperature as $(m/2)\bar{v}^2 = (3/2)k_\mathrm{B}T$ results in the ideal gas law [113].

$$pV = Nk_\mathrm{B}T. \tag{4.1}$$

Here, N represents the number of particles, T the absolute temperature and k_B the Boltzmann constant. A more detailed derivation of the equation is given in [113] and [114] where also the fundamental concepts of gas kinetics are discussed comprehensively.

4.1.2 The Van der Waals equation

The following explanation follows [113]. The assumptions, which were taken to derive the equation of state for an ideal gas, do not hold in any case. If the pressure in a system increases the assumption that the gas particles can be treated as point-like masses breaks down. Thus, one has to take into account the Volume V_a an individual gas particle occupies in space. The total volume the gas particles occupy is then given by NV_a. The correction of V can be derived by averaging over all atoms N in the Volume [113]. The result is a parameter $b_\mathrm{vdW} = 4NV_\mathrm{a}$ which has to be subtracted from the Volume V [113].

In addition, high pressures and low temperatures invalidate the assumption that there is no other interaction between the particles than fully elastic collisions. Thus the potential energies, which result form the attractive interaction between the particles can no longer be omitted. Simple considerations of symmetry show that for particles within the gas, which are only surrounded by other gas particles the rotational symmetry cancels out the attractive forces between the particles. However, when a particle is close to the wall the interaction will lead to a resulting force pulling the particle away from the wall. This behaviour can be described as an effective pressure a_vdW/V^2, increasing the total pressure within the gas [113]. The constant a_vdW is taking into account the strength of the interaction and is a substance depending constant.

Adding the two correction terms just discussed to the ideal gas law results in the van der Waals equation for a real gas [113]

$$\left(p + \frac{n^2 a_{\mathrm{vdW}}}{V^2}\right) \cdot (V - n b_{\mathrm{vdW}}) = nRT. \tag{4.2}$$

The constants a_{vdW} and b_{vdW} are usually referred to as van der Waals constants and n denotes the amount of substance. The corresponding values for NO of the two constants are given in [66]. The subscript vdW is uncommon and has been added to avoid confusion with the molecular hyperfine constants introduced in section 1.9. The van der Waals equation uses the universal gas constant R instead of the Boltzmann constant k_{B}. However, the two constants can be linked easily via the Avogadro constant: $R = N_{\mathrm{A}} \cdot k_B$.

4.2 Gas flow dynamics

This section follows [115]. The flow of fluids and gases is governed by their own thermal movement and forces that result from local differences in pressure [115]. The particles move from regions of higher pressure to regions of lower pressure. Gas flow is called stationary if the velocity of the flowing gas stays constant at any position of the system [113]. However, this does not mean that the velocity is the same at any position in the system. In the gas mixing unit of the experiment two pumps are used to generate a pressure difference and draw the gas through the pipe system. If the settings are not changed, the flow can be considered to be stationary after a few minutes equilibration time. The exact equilibration time varies in dependence of the system settings.

There are two main types of gas flow that are fundamentally different. The first type is called molecular or ballistic flow. This type of flow occurs for low pressures where collisions of the gas particles with each other are less likely than collisions of the gas particles with the wall of the gas line. Therefore, the gas particles follow individual trajectories that are driven by their thermal movement. Averaging over many of the

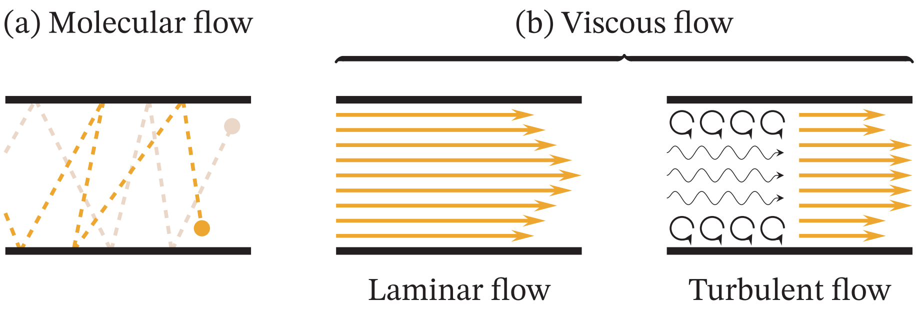

Figure 4.1: Schematic explaining basic types of gas flows. (a) Molecular flow, sometimes also denoted as ballistic flow. Particles only collide rarely with each other and follow individual trajectories. (b) Viscous flow, macroscopic behaviour without individual trajectories. This type of flow can be separated in laminar and turbulent flow. The orange arrows indicate the velocity profile along the cross section of the pipe. After [115].

individual trajectories will result in a macroscopic flow [115]. This is illustrated in figure 4.1a.

If the pressure is higher the mean free path of the particles is shorter and they interact strongly via collisions. The collisions allow the exchange of energy and momentum amongst the particles. Henceforth, the particles can be treated macroscopically and individual trajectories are not longer relevant. This type of flow is denoted as viscous flow. It is driven by a pressure difference along the gas line [115] and depicted in figure 4.1b. The orange arrows indicate the velocity distribution along the pipe cross section. The speed of flow is lower at the edges due to friction between the gas with the wall. That friction may cause vortices in the transported medium. Thus viscous flow can be separated in two different sub-categories which are denoted as laminar and turbulent flow. Laminar flow does not show any vortices because the friction between the gas and the wall is small. Turbulent flow occurs at higher friction, thus often for large velocities, since velocity dependent forces of friction are increased then. A part of the gas particles is slowed down by the friction leading to forces pulling some of the particles towards the wall which causes vortices and turbulence [115].

The transition between different flow types is continuous. Henceforth, there are intermediate types of flow which are neither well described as ballistic nor as viscous. For planning and operation of the gas system it is important to know which type of flow prevails. Therefore, quantitative tools are necessary to determine what flow one has to expect in the system. These tools are the Knudsen and Reynolds number which will be introduced in the following sections.

4.2.1 Viscous or molecular flow - the Knudsen number

To distinguish between molecular and viscous gas flows the Knudsen number is introduced. It is a dimensionless number which relates the mean free path l of the gas particles to the geometric expansion of the gas line cross section [115]. In case of a cylindrical pipe the geometric expansion is given by its diameter d. The Knudsen number Kn can then be defined as [115]

$$\mathrm{Kn} = \frac{l}{d}. \tag{4.3}$$

The Knudsen number can also be expressed in terms of the mean thermal velocity. Equation 4.3 transforms then to [115]

$$\mathrm{Kn} = \frac{\pi \bar{v}(T)\eta(T)}{4pd}, \tag{4.4}$$

depending also on the pressure p and the viscosity $\eta(T)$ of the gas.

The transition region in between is named Knudsen flow. In [116] the definition of the different flow regions is given as follows

$$\begin{aligned} &\mathrm{Kn} < 0.01 \text{ viscous flow,}\\ &0.1 > \mathrm{Kn} > 0.01 \text{ slip flow,}\\ &10 > \mathrm{Kn} > 0.1 \text{ transition region}\\ &\mathrm{Kn} > 10 \text{ molecular flow.} \end{aligned}$$

Slip flow is a special case that occurs at the edge of the transition region to the purely viscous flow.

4.2.2 Laminar or turbulent flow - the Reynolds number

If the flow is in the viscous regime, it is useful to determine if turbulences or vortices are to be expected or not. The approach to do so, is the same as in case of the Knudsen number. The physical quantities that mainly define if the flow is laminar or turbulent are compared to obtain another dimensionless number. In this case the corresponding number is denoted as Reynolds number. The two forces defining the gas flow are the force of inertia which depends on the density ρ and flow velocity v of the gas and the friction that causes the slowing of the outermost gas layers [115]. The friction is proportional to the viscosity $\eta(T)$. The Reynolds number is then defined by [115]

$$\mathrm{Re} = \frac{\rho v d}{\eta(T)}. \tag{4.5}$$

The parameter d is as previously introduced the diameter of the corresponding pipe. Note that for a different shape of the gas line the diameter has to be replaced by the corresponding expression for the gas line cross sectional expansion. In [115] the different viscous flow types are split into three different regions. A low Reynolds number marks pure laminar flow, a high Reynolds number turbulent flow. In between a intermediate flow region is defined where the flow is neither fully viscous nor fully turbulent. The corresponding definition is [115]

$\mathrm{Re} < 2300$ laminar flow,
$\mathrm{Re} > 2300 < 4000$ intermediate flow,
$\mathrm{Re} > 4000$ turbulent flow.

4.2.3 The Hagen-Poiseuille equation

The flow of fluids through pipes is important for numerous applications. It is described by the law of Hagen-Poiseuille. It results from integration from zero to the pipe radius $R = D/2$ over the velocity field $u(d)$ describing the flow velocity of the respective fluid at the radial distance $d/2$ from the center of the pipe. The velocity field $u(d)$ is given by [113]

$$u(d) = \frac{p_1 - p_2}{16\eta(T)L}(D^2 - d^2), \tag{4.6}$$

and depends on the pressure difference $p_1 - p_2$ along the pipe, the length of the pipe L and the viscosity $\eta(T)$. The velocity field can be derived by equating the friction force on the cylindrical surface of the fluid and the force exerted by the fluids pressure on the cross sectional area of the pipe.

The Hagen-Poiseuille equation is then obtained by integration of the velocity field over the cross section of the pipe, determining the volume flow $V/t = I$ through the cross sectional area per unit of time. The result is then given by [113]

$$\frac{V}{t} = I = \frac{\pi\left(\frac{D}{2}\right)^4 (p_1 - p_2)}{8\eta(T)L}. \tag{4.7}$$

The current is strongly depending on the pipe diameter and is driven by the pressure difference $\Delta p = p_1 - p_2$. Equation 4.7 has been experimentally derived for Newtonian fluids by Hagen as well as Poiseuille. However, according to [117] it is also very accurate for gases as long as they are not strongly diluted.

4.3 The setup and its components

The gas mixing unit is basically separated in two parts. The first part is the pipe and valve system which connects the gas bottles to the different mass flow controllers (MFC). This part of the setup has to be able to supply enough gas to the system to achieve a continuous flow and to enable the mixing of gas.

The second part of the gas setup consists of standard vacuum components including flexible stainless steel hoses, flanges, the spectroscopy cell itself, the chokes and pumps. In the second part of the setup parts can be exchanged relatively easy. Especially the exchange of the spectroscopy cell is important since the optimisation of the cell is an important future task of the sensor development.

4.3.1 Safety aspects

Nitric oxide is, as stated in section 2.1 toxic. It is therefore crucial to avoid the leakage of NO from the system into the laboratory. At room temperature NO reacts with the oxygen present in air and forms nitrogen dioxide (NO_2) [118]. Nitrogen dioxide is toxic too [119] but is easier to perceive since it is a brown gas with a distinct, sharp odour. To avoid leakage the vacuum pumps are running continuously, keeping almost the full system at a lower pressure than the laboratory. In case of a leak air will be sucked into the system. Of course, the gas bottle and the connection of the bottle cannot directly be set to a pressure lower than ambient pressure. To decrease the risk, the high pressure area was constructed to have a relatively low volume. In addition, the pressures set at the nitric oxide pressure reducer are chosen to be relatively low above atmospheric pressure.

Furthermore, the design of the gas mixing unit required it to take into account the corrosive properties of NO. Most types of plastic are only partially resistive to NO [120]. According to [120] only Polytetrafluoroethylene (PTFE) and Polyether ether ketone (PEEK) are well resistant to NO. Thus, in particular the pipe system in front of the mass flow controllers, where the NO is present at higher pressure, had to be build using plastic seals made of one of the two types of plastic. In case of closed mass flow controllers, the NO is not flowing through this part of the system and therefore in direct contact with the seals for longer periods of time. Since PTFE is more commonly used for sealing applications it has been chosen for the employed ball valves. In addition, to PTFE, stainless steel and glass are employed. For the lower pressure regions standard flanges are employed. The sealing rings are not made of PTFE but only have contact to the NO flow with a very small part of their surface and the overall amount of NO present is smaller than in the pipe system. Of course, also the employed pumps have to be suitable for pumping corrosive gases and where selected accordingly. The employed pressure reducer for the NO gas bottle has an additional valve which can be connected to the nitrogen gas bottle. This allows it to flush all parts of the system that were in contact with NO with Nitrogen every time after usage. Another essential safety aspect of the design is to avoid nitric oxide in the gas lines exclusively meant for nitrogen. The details on how to ensure this are discussed in section 4.3.3.

The outlet of the full gas system which is the outlet of the last pump is connected to a suction system which is part of the building's infrastructure to dispose waste gases or fumes. Gas ballast valves ensure the fast disposal of the toxic and corrosive gas via the suction system. A more detailed explanation will be given in section 4.3.4. Of course, a failure of the suction system may result in a dangerous situation where the NO is no longer transported away and may leak from the suction system into the room. To avoid this scenario differential pressure detectors have been installed which measure the pressure difference between the suction system and the ambient pressure in the laboratory. If the pressure difference sinks under a certain threshold an alarm will notify the experimenters and the gas flow can be stopped.

4.3.2 Mass Flow Controllers

Creating a gas mixture with a certain ratio between two gases can be achieved with different techniques. A very simple approach would be to use two buffer vessels with the same volume, filling each with one type of gas to a certain pressure so that the pressure ratio resembles the desired ratio between the two gases. However, this static method suffers from a list of drawbacks. Depending on what ratio is required either the volumes or the pressures to mix the two gases have to be set to extreme values that may be difficult to realise. In addition, only a fixed amount of gas is available to perform a measurement. This limits the time of measurement and is especially critical when it is not fully clear how much gas is needed for a certain measurement. Furthermore, signal optimisation depending on the gas concentration and composition will be time consuming, since the concentration can not be changed dynamically.

Because of the aforementioned reasons a different approach was chosen for the presented gas mixing unit. To be able to change the concentration of nitric oxide in nitrogen continuously the system relies on a dynamic mixing method employing

Table 4.1: Overview over the minimum and maximum flow rate of the employed mass flow controllers in standard cubic centimetres and which gas type they are used for.

Max. flow in sccm	Min. flow in sccm	Gas type
50000	1000	N_2
2000	40	N_2 and NO
100	2	N_2 and NO
5	0.1	NO

mass flow controllers. Thus, the mixing ratio of the two gases is given by the ratio of the flow through the employed mass flow controllers.

The employed mass flow controllers are thermal MFCs and part of the GM50A series of MKS Instruments Incorporated. They use a heating element to heat up the gas and compare the gas temperature before and after the heating element. From the transported thermal energy the device can calculate the mass transfer through a certain aperture using a look-up table with the corresponding proportionality constants for the type of gas measured. The GM50A series MFCs are calibrated with nitrogen and the maximum flow rate setting may change for different gases. This is not the case for nitric oxide. For the controllers only metal seals and PTFE seals are used so that they are able to withstand nitric oxide.

To be able to cover the full range of possible dilutions, the flow rates of the employed mass flow controller have to overlap. For the desired dilution factor of 10000 at least four mass flow controllers are required. An overview about the employed MFCs is given in table 4.1. The flow rates are given in standard cubic centimetres (sccm). A flow of 1 sccm corresponds to 1 cm^3/min under standard conditions, i.e. $p_{\text{std}} = 101\,325\,\text{Pa}$ and $T_{\text{std}} = 0\,°\text{C}$ [115]. Another commonly used unit for the gas flow is mL/min which is essentially the same as cm^3/min. Nitric oxide is either used in pure form or diluted with nitrogen. In any of the two cases the total flow of NO that is required is small. Therefore, the MFC with the maximum flow rate does not have to be employed for nitric oxide but only for nitrogen. The potentially high nitrogen flows, which will be required to mix very dilute samples, set certain requirements for the pipe radius. The expected volume flow through a pipe with diameter D can be estimated with equation 4.7. The mass flow controllers require a certain pressure differential to work correctly. In addition, the pressure at the MFC inlet is not allowed to exceed a certain value. In the case of the GM50A series the maximum inlet pressure is 10.34 bar and the allowed pressure differential between 1.72 bar and 2.75 bar for the MFC with the largest volume flow. For the MFCs with smaller flow rates a value between 0.69 bar and 2.75 bar is allowed. To estimate the gas flow at room temperature the viscosity of nitrogen at 300 K (see table D.1 in the appendix) and a pressure differential of $\approx$ 1 bar is assumed. For a pipe diameter of 4 mm and a pipe length of 10 m equation 4.7 yields a flow of $\approx$ 210 L min^{-1}. This is more than four times the maximum flow of the MFC with the highest flow rate. This shows that a pipe with an inner diameter of 4 mm is more than sufficient to supply enough gas to the system. Especially, since the pipe length has been rather overestimated and in principle the pressure difference can also be increased. Before the full system was set up the calculation was verified by an experimental test, where the pressure before the inlet of the MFC at full flow was measured to see if the opened MFC still dams up the nitrogen gas.

The employed mass flow controllers reach the best precision for a flow set point between 20 % and 100 % of the maximum possible flow. Thus, for the highest possible mixing precision the overlap between the flow rates of the different mass flow controllers should be at least 20 %. This would require a total of seven mass flow controllers instead of four. The setup could be extended by adding the respective MFCs. A list of the seven MFCs that would then be employed is given in table 4.2. Diluting a gas by a factor of 10000 is not sufficient, if dilutions in the parts per million or parts per billion regime are required. To achieve such low concentrations of NO it is easier to start with pre-diluted gas which can be bought as calibration gas with concentrations of 100 ppm or 10 ppm for example.

4.3.3 Pipe and valve system

The pipe and valve system connects the gas bottles with the input of the mass flow controllers and their output to the cell and pump system. The system has been de-

Table 4.2: List of mass flow controllers that would be needed for maximum mixing precision. The highest flow precision is achieved for a setpoint between 20 % and 100 % of the maximum flow.

Max. flow in sccm	20 % in sccm	Min. flow in sccm	Gas type
50000	10000	1000	N_2
10000	2000	200	N_2
2000	400	40	N_2 and NO
500	100	10	N_2 and NO
100	20	2	N_2 and NO
20	4	0.4	N_2 and NO
5	1	0.1	NO

signed to comply with the safety aspects disscused in section 4.3.1. The pipe system consists of seamless stainless steel pipes with an outer diameter of 6 mm and an inner diameter of 4 mm. Seamless pipes have been chosen because they have the same structural integrity at any point. The pipes where cut and bend to fit on a perforated metal plate which is used as a mounting base for the system. They are connected to the valves and to each other with cutting ring fittings. There are two types of valves in the system. Both with an inner diameter of 1/4". The ball valves are used to open or close gas lines, while the three-way ball valves are used to choose between the different gas types. There are only three-way ball valves with L-drillings. The L-drillings provide the advantage that the three-way ball valves can be closed completely and that it is never possible to connect the openings of the valve which are opposite to each other. This ensures that lines that can be used for both gases cannot accidentally connect the NO lines to parts of the setup which should not come in contact with NO. Figure 4.2 gives an schematic overview about the gas mixing unit and the possible positions of the different valves. The system has three gas inlets. The N_2 inlet can be connected to the three largest MFCs, while the NO and NO-mix inlets can only be connected to the smallest three MFCs. After the gas streamed through the MFCs the lines are connected to one single line. The outlet connector is a standard KF-16 flange. The system has been leak tested for under and over

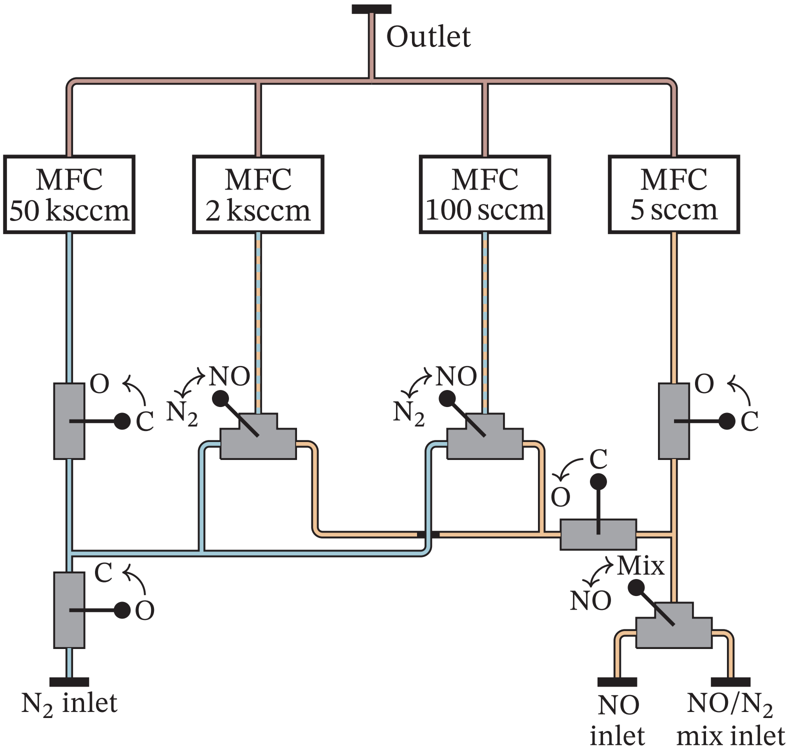

Figure 4.2: Schematic overview of the gas mixing unit. The letters O and C indicate if the valve is open or close for the respective position of the handles. N_2 gas lines are marked blue and NO gas lines in orange. The red coloured pipes indicate the area where the gas is mixed together, the blue and orange lines are those which can be used for both gases.

pressure. The over pressure test was conducted with leak detection spray and dry nitrogen at a pressure of around 5 bar. For the under pressure test the system was connected to a rotary vane pump and turbo pump. Leaks were detected by spraying alcohol on the connections. The adapters from the 6 mm tubing to the ball valves were additionally sealed with PTFE sealing tape.

The system was set up and also tested within the scope of [121]. The tests were conducted with a commercial gas sensor for carbon dioxide. Thus, instead of nitric oxide carbon dioxide was mixed with nitrogen. This was mainly done for safety reasons. CO_2 concentrations below 500 ppm could not be measured due to the limited capabilities of the CO_2 sensor. However, an important information that could be retrieved, was the average waiting time necessary between changes of the concentration. It could be shown that a change of the MFC-settings will almost immediately change the composition of the mixed gas, but a stable equilibrium, i.e. a constant concentration of CO_2 needs an equilibration time of $t_{\mathrm{Eq}} \approx 450\,\mathrm{s}$. Thus, it is recommended to wait at least 500 s after a change of concentration to proceed with the measurements.

Stainless steel parts have a large number of benefits like their good availability and high resistivity against corrosion as well as good machine-ability. However, they also come with a drawback. They can form nitrosyl complexes with nitric oxide, where several nitric oxide molecules act as ligands [122–124]. The formation of nitrosyl complexes may lead to adsorption and desorption of nitric oxide on metal surfaces [125] in dependence of the ambient conditions. This process is particularly problematic for a static mixing method as stated in [9]. If a considerable amount of NO is adsorbed to the metal surface of a pipe or vessel it stays on the surface for the moment. However, if the surrounding pressure drops, for example, if the flow through the pipe changes or the vessel is emptied the NO molecules bound to the surface may desorb from the surface, thus changing the NO content of the gas flowing through the pipe or that is still inside the vessel.

So far it is not clear how large the effect may be for the presented gas mixing unit. The dynamic mixing method may proof to be less sensitive to these processes, since there may be a dynamic equilibrium between adsorption and desorption after some time without a concentration change in the gas flow. Even in the worst case scenario, i.e. a strong influence of adsorption or desorption on the absolute concentration of the mixed gas, it should still be possible to test the sensor by detecting changes in the NO concentration. It is in any case helpful to keep such effects in mind for future experiments and the interpretation of the respective datasets.

4.3.4 Vacuum system

Behind the gas mixing unit the gas has to be pumped through the cell where the measurements take place. The optimal pressure differs and depends on the type of measurement and the cell that is used. It is therefore crucial to set the cell pressure and pressure difference along the cell as precise as possible. The Vacuum system was designed to do that and has been altered several times to comply with the requirements of the experiment. Figure 4.3 gives an overview about the vacuum and pump system in its current form. The system is connected via a KF16 flange to the gas mixing unit. It consists of standard vacuum components, mainly of flexible KF16 steel hoses. Employing only standard components has the advantage that parts of the setup can be exchanged quickly so that alterations are not too time consuming. The desired end pressures inside the cell are in the range of 1.0×10^{-5} mbar. Pressures in that range can be realised without the necessity for long bake out procedures or copper flanges (CF).

The gas line is split up right after the connection to the gas mixing unit into two lines. The main line is connected to the cell via a ball valve which can be used to shut off the cell from the gas flow. Since the cell pressure and the pressure difference between cell inlet and outlet is crucial, there are two full range pressure gauges installed directly at the cell inlet and outlet. Behind the cell the gas line is interrupted by two butterfly valves. When those valves are partially closed they act effectively as chokes for the gas flow. If butterfly valve 3 is shut, the gas flow is directed through the throttling line. This part of the setup is made of the same stainless steal pipes as the gas mixing unit, i.e. the inner diameter of the throttling line is only 4 mm. The throttling line is 1.7 m long and can be used to strongly limit the suction power of the turbo pump. In addition, the bypass line which can be closed with butterfly valve 1 influences how much gas can reach the cell. In combination with the mass flow controllers the butterfly valves and throttling line enable the precise adjustment of the cell pressure and pressure differential.

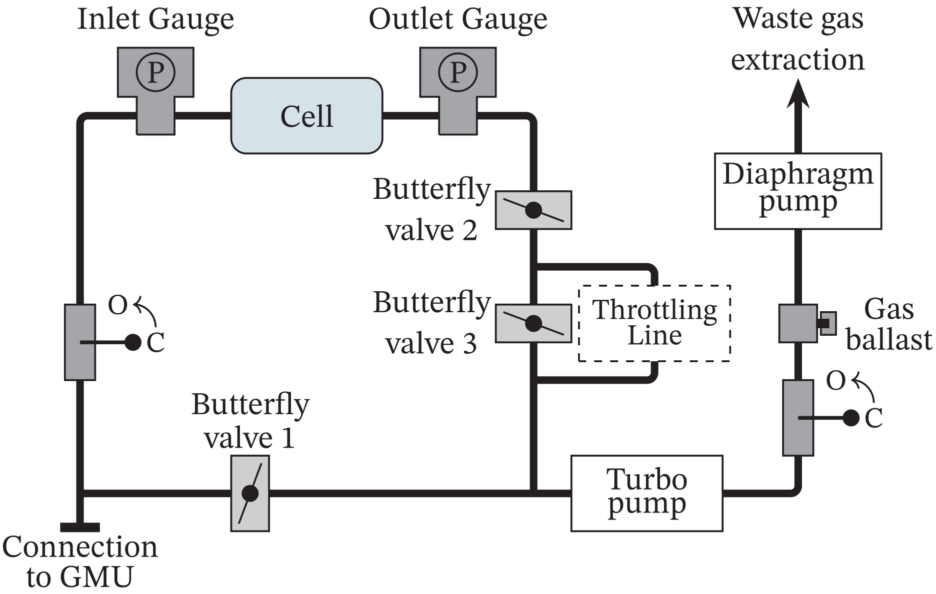

Figure 4.3: Schematic of the vacuum system connected to the gas mixing unit. It contains a bypass and throttling line for coarse adjustments of the pressure difference along the cell. The butterfly valves 2 and 3 can be employed as additional chokes.

After passing through the cell and turbo pump the gas is pumped out of the system by a diaphragm pump. The diaphragm pump is especially designed to withstand corrosive gases and can pump a maximum of $56\,\mathrm{L\,min^{-1}}$. This is more than the total possible flow through the mass flow controllers. However, in case that the system is extended by additional mass flow controllers, as suggested in table 4.2, the maximum possible flow through the mass flow controllers is larger then the maximum volume the pump can transport. One can then either limit the maximum flow through the mass flow controllers or exchange the diaphragm pump.

As already mentioned, the diaphragm pump is especially made for corrosive gases with the diaphragm and seals made of PTFE. To additionally protect the pump from corrosion, a gas ballast valve is installed at the pump inlet. The gas ballast valve has a small inlet where air can flow into the pipe to mix with the gas pumped from the cell. The oxygen in the air will oxidise most of the nitric oxide before it is pumped through the diaphragm pump. Nitrogen dioxide is corrosive itself but the additional gas volume is helpful to flush the gas lines and remove as much nitric oxide and nitrogen dioxide as possible. In addition to that, a second gas ballast valve is installed at the gas line of the suction system, so that the disposal line following the outlet of the diaphragm pump is flushed permanently too. This ensures that the corrosive gasses are effectively transported away and at the same time dilutes the gasses with the air that is sucked in through the gas ballasts. Condensed moisture in the gas lines of the waste gas extraction or water vapor present in the air sucked in through the gas ballast valve can lead to the formation of nitric acid[126]: $3\mathrm{NO_2} + \mathrm{H_2O} \rightarrow \mathrm{NO} + 2\mathrm{HNO_3}$. This should be kept in mind when changing parts connecting the diaphragm pump to the waste gas extraction.

In section 4.2.1 and 4.2.2 the Knudsen and Reynolds number have been introduced. These numbers can now be used to coarsely estimate which type of flow one would expect inside the vacuum system and gas mixing unit. The viscosities $\eta(T)$ of nitrogen and nitric oxide can be found in the appendix in table D.1. The Knudsen number in dependence on the pressure is depicted in figure 4.4 for different pipe diameters. The difference between NO and $\mathrm{N_2}$ is negligibly small.

Measurements are typically conducted in the pressure range between 1.0×10^{-1} mbar and 1.0×10^{-4} mbar. For most pipe diameters the flow is expected to be in the intermediate flow regime between viscous and laminar flow. For small pipe diameters

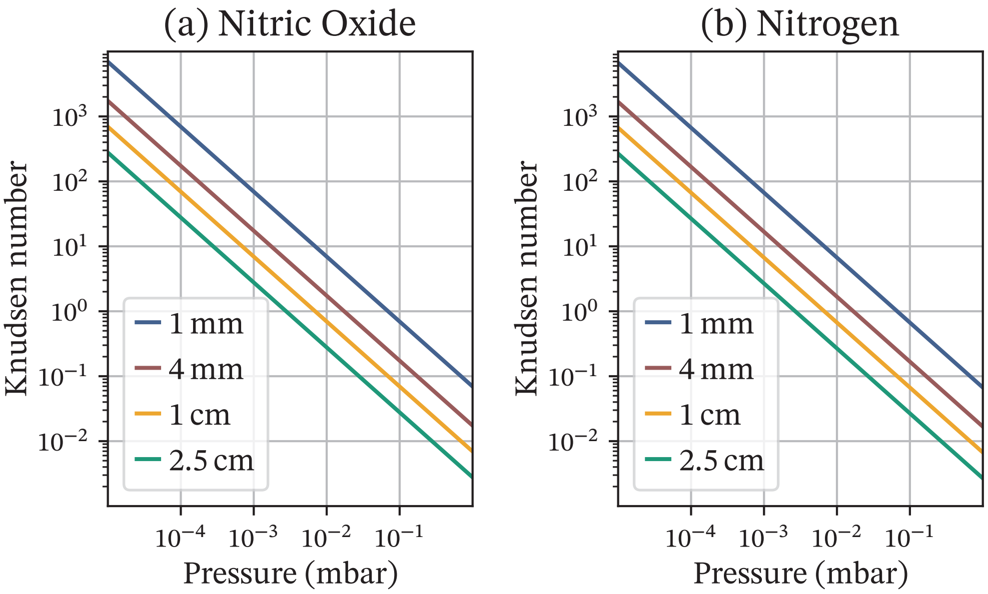

Figure 4.4: The Knudsen number in dependence of the pressure in the gas system for different pipe diameters plotted with logarithmic axes. (a) Calculated for Nitric Oxide. (b) Calculated for Nitrogen

ballistic transport prevails from pressures around 1.0×10^{-2} mbar downwards. For larger pipe diameters at the higher end of the pressure range the flow can be considered as viscous and is only ballistic for very low pressure values. The cells used for the experiments presented in this thesis had rather larger diameters. A very typical size is a diameter of one inch. The pipe system has an inner diameter of 4 mm. However, since the pressure in front of the mass flow controllers is considerably higher than behind, only laminar flow can be expected in this region. The curve for a diameter of 1 mm is an exemplary boundary case. Since the goal for the cells for optogalvanic measurements is to be miniaturised. A diameter of 1 mm is a realistic and realisable cell size. It is important to keep in mind that the calculated values from figure 4.4 are only coarse estimates. Treating the cells as pipes, is a simplification neglecting curves and bends at the cell in- and outlet. In addition, curves and crossings of the gas lines are completely neglected too. However, the calculation at least shows that both flow regimes should in principle be accessible. Which pressure is most favourable for the aquisition of data depends on the cell type and if the measurement is optical or optogalvanic. The easiest way to find the optimal pressure is to systematically ramp through different pressure values with the other measurement parameters fixed.

In the case of viscous flow it may be important to know if turbulences occur. The largest pressure difference in the system is present immediately after the mass flow controllers are opened. Which can be estimated to be 1 bar. Thus, immediately after opening the MFC there will certainly be turbulences in the gas flowing into the system. However, after some time of continuous gas flow there will be a pressure gradient along the system with way lower pressure differentials than for the time directly after the opening of the MFC valve. Since the pressure is only measured for the cell inlet and cell outlet a useful estimation of the Reynolds number can only be given for the cell itself. The calculation of the Reynolds number requires the density and the flow speed of the gas. Both parameters have to be estimated for this setup. From equation 4.6 the flow speed can be estimated. By setting $d = 0$ one obtains the maximum possible flow speed in the pipe. The density can be estimated from an equivalent formulation of the ideal gas law (equation 4.1) relying on the specific gas constant R_S.

$$\rho = \frac{m}{V} = \frac{p}{R_S \cdot T}. \tag{4.8}$$

Assuming a cell length of 10 cm, a cell diameter of 2.54 cm, a mean cell pressure of 1 mbar and a pressure difference in the same order of magnitude, i.e. $\Delta p = 0.5$ mbar yields for the gas specific parameters of nitrogen (the specific gas constant of N_2 can be found in [127]) a Reynolds number of Re $\approx$ 1795. Thus, one would not expect turbulences under these conditions. The assumed pressure of 1 mbar is around one order of magnitude higher then typical pressures during measurements. In addition, the pressure differential has been overestimated. The difference between nitrogen and nitric oxide is negligible, so that in general one can assume, that in case of a viscous flow inside the cell, turbulences are not expected. Of course, this is again a very rough estimation and there may be turbulence occurring due to line crossings and curves. Especially when the butterfly valves are not fully closed, turbulences may occur. However, gas that flows through any of the butterfly valves is either bypassing the cell or has already passed it so that the type of flow is no longer of importance.

For higher pressures which may eventually be investigated when dealing with strongly diluted NO or real breath samples the setup may have to be altered. For example one could use a buffer vessel between the MFCs and cell to temporarily store the gas mixture. This would allow to measure at low pressures even for strongly diluted mixtures which require large flow rates. A buffer vessel would also need an additional MFC to control the flow out of the vessel.

5 Rydberg excitation of nitric oxide

Introduction

The excitation of nitric oxide to high lying Rydberg states has been achieved already with different excitation schemes [68, 128, 129]. Also optogalvanic spectroscopy has been used to detect such Rydberg states in NO [6, 9]. However, it has not been achieved by using the three-photon excitation scheme introduced in section 2.2. In contrast to earlier work narrowband continuous wave laser systems are employed. The excitation of NO to high lying Rydberg states is crucial for the proposed sensing technique. It opens up the possibility to test, optimise and improve the sensing technique on the electronic as well as the laser based parts of the system.

This chapter gives on overview on the proof of concept for the three-photon excitation scheme. The Rydberg excitation has already been topic of [71] and [8].

In section 5.1 the optical setup and exact excitation scheme are explained. Then in section 5.2 the excitation and detection of the $\mathrm{H}\,^2\Sigma^+$ state with optogalvanic spectroscopy is discussed. It follows a brief discussion of the Rydberg excitation in section 5.3. The chapter closes with an outlook on the potential of optogalvanic spectroscopy and the sensing principle in section 5.4.

5.1 Optical setup and cell

The basic setup of optogalvanic spectroscopy is depicted in figure 5.1a. The employed spectroscopy cell was cylindrical, 80 mm long and had an outer diameter of

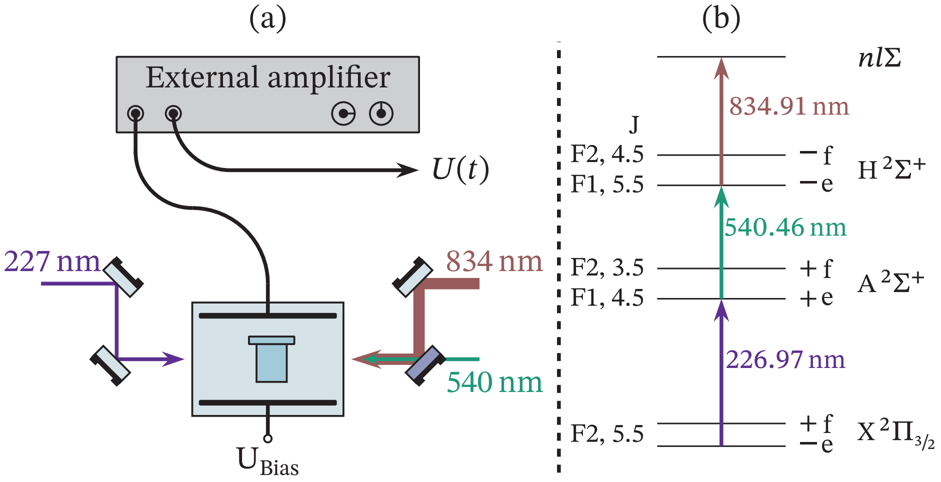

Figure 5.1: (a) Schematic of the measurement setup for the Rydberg excitation of NO. The gas inlet and outlet of the cell are at right angle to the electrodes and laser beams. The UV-laser is counter-propagating to the red and green laser. (b) Level scheme of the exact excitation path with which the Rydberg excitation was first realised in our lab.

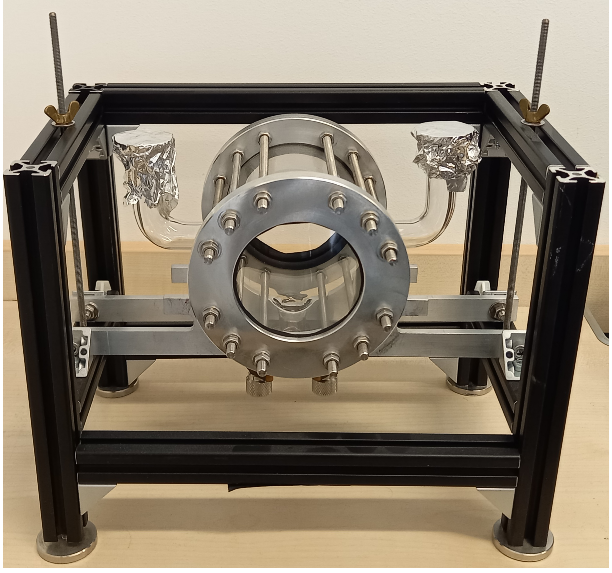

Figure 5.2: Picture of the employed through-flow gas cell without any electrodes inside. Further information on that cell is given in [82].

80 mm. Further information on the cell can be found in [82], where additionally the two possible electrode configurations, that were employed first, are explained and analysed. A picture of the cell is shown in figure 5.2. The first electrode configuration was basically a plate capacitor. The second electrode configuration shielded the measurement electrode from the UV-laser beam to avoid an additional offset due to charges generated by the photoelectric effect. Both electrodes enable the detection of nitric oxide Rydberg states.

The gas inlet and outlet of the cell is at right angle to the electrodes and laser beams. The first Rydberg spectra were taken during the time where the gas mixing unit explained in chapter 4 was under development. Nevertheless, the measurements were performed in through flow. However, the flow was regulated with a single needle valve controlling the amount of gas flowing into the cell. Since the needle valve had to be adjusted by hand and no active regulation was employed, the pressure changed over longer periods of time. This hinders the comparison of individual spectra to each other. The installation of the gas mixing unit introduced in chapter 4 increased the pressure stability significantly, i.e.the pressure could be kept stable for several hours.

The UV-laser counter-propagates the two other lasers through the cell. The red and green laser were overlapped with a dichroic mirror. The beams were shaped to similar sizes. For the first measurements active power stabilisation was not available for the green and red transition. The UV-laser could already be stabilised with a rotating waveplate. The stabilisation setup is based on [130].

The green and red laser underwent beam shaping before they were sent to the spectroscopy cell. When the first measurements were conducted the setup to lock the lasers had not been completed, so that the lasers had to be repositioned quite frequently. The high uncertainty of the parameters complicates systematic comparison of the measurements. However, the main point is to prove the feasibility of the excitation scheme for the application in gas sensing.

The employed external amplifier is a *DL Instruments Model 1211 Current Preamplifier*. Which is a commercially available trans-impedance amplifier with a measurement range from 1×10^{-2} A to 1×10^{-12} A. Its output was connected to an oscilloscope to measure the corresponding voltage $U(t)$.

The exact excitation scheme for the Rydberg excitation is shown in figure 5.1b. Up to the $\mathrm{H}\,^2\Sigma^+$ state the scheme is the same that has been employed in [76]. The final step to Rydberg states is the same as in [68]. The UV-transition is at 226.97 nm. It belongs to the oP_{12ee}-branch with $\mathrm{J}_\mathrm{X} = 5.5 \leftarrow \mathrm{J}_\mathrm{A} = 4.5$. The green transition belongs to the R_{11ee} branch between the $\mathrm{A}\,^2\Sigma^+$ and $\mathrm{H}\,^2\Sigma^+$ state with a change of the rotational quantum number from $\mathrm{J}_\mathrm{A} = 4.5$ to $\mathrm{J}_\mathrm{H} = 5.5$. It is at a wavelength of 540.46 nm. The observed Rydberg transition occurred at 834.91 nm.

5.2 Excitation of the $\mathrm{H}\,^2\Sigma^+$ state

The optogalvanic spectroscopy technique works if only the UV-laser is scanned over resonance and the other two lasers are blocked. However, the investigation of the mechanism underlying the charge production showed that most charges are not

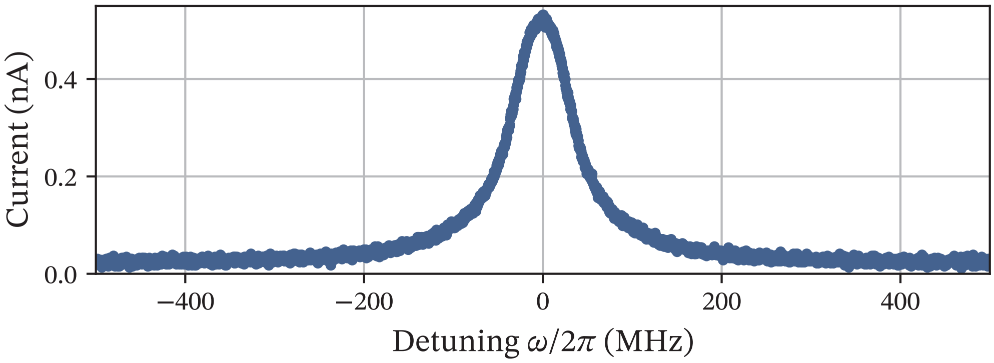

Figure 5.3: Exemplary current signal for the A $^2\Sigma^+ \leftarrow$ H $^2\Sigma^+$ transition. The data was Fourier filtered to remove noise above 45 Hz. The exact parameters of the measurement can be found in the text.

produced by collisional ionisation [71]. The resulting current is small. Adding the green laser, i.e. keeping the UV-laser on resonance and scanning the green laser above the resonance, produces a clear current signal. The signal is not detectable optically [71]. An exemplary dataset is plotted in figure 5.3. The dataset was taken with 12 mW UV-laser power and 750 mW green laser power. The bias voltage was $U_{\text{Bias}} = 10\,\text{V}$ and the pressure 0.63 mbar. The dataset was averaged three times on the oscilloscope and later Fourier filtered, i.e. frequencies above 45 Hz were removed from the data. This increases the signal to noise ratio and is necessary because especially the cables to the external amplifiers pick up a lot of 50 Hz noise.

The excitation generates a current of around 0.5 nA. The main ionisation mechanism was identified as collisional ionisation by measurement of the power dependence of the current [71].

The pressure of 0.63 mbar was not optimised so that larger signals may be possible at a different pressure. However, the signal optimisation of the green transition is beyond the scope of this work.

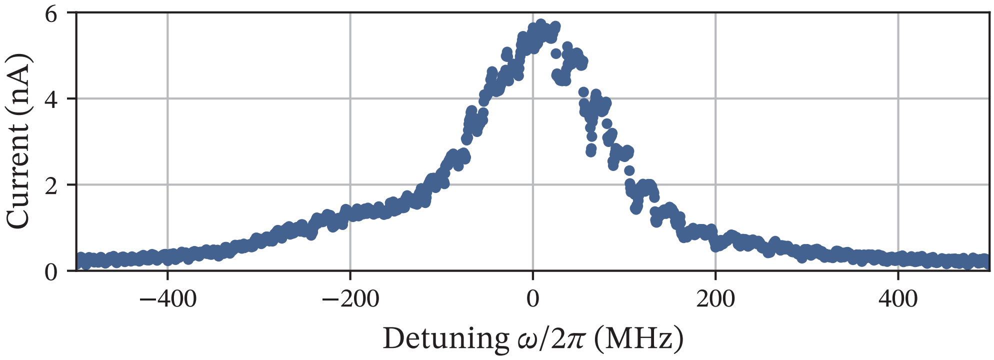

Figure 5.4: Exemplary signal for the transition from the H $^2\Sigma^+$ state to a Rydberg state. The exact parameter of the measurement can be found in the text.

5.3 Rydberg excitation of nitric oxide

The Rydberg excitation adds additional selectivity to the scheme and increases the current, since the collisional energy needed for ionisation is much lower. In figure 5.4 a typical Rydberg signal is plotted. The data was taken after signal optimisation, so that it was not necessary to Fourier filter the signal. However, the data was post-processed by a Savitzky-Golay filter. The UV laser power was 35 mW, the green laser power 1.15 W, the red laser power 350 mW and the pressure 0.51 mbar. The bias voltage was 10.1 V. The maximum current is significantly larger than for the two-photon signal. The signal is also wider and shows small signs of asymmetry. This is most likely due to the electric field originating from the applied bias voltage. Rydberg states are particularly sensitive to electric fields.

However, since the main purpose of those measurements was the general proof of the excitation scheme, the absolute measured current was not important at this stage of the experiment. A full characterisation of the cell and amplifier configuration presented here has not been conducted, since back then pressure and laser frequency stability were not under control well enough.

5.4 Outlook: Optogalvanic spectroscopy

There are many areas suitable for enhancement in the presented optogalvanic spectroscopy setup. The gas mixing setup and laser frequency stabilisation have been completed after the measurements presented in section 5.2 and 5.3 were conducted. The main parameters determining the efficiency of this spectroscopy technique are the cell pressure, laser power, bias voltage, cell design and electronics. The first three have to be empirically determined for each employed cell type.

The cell design and electronics are linked closely to each other. Future cells are expected to rely on onboard amplifiers which will reduce the pick up of noise significantly. The amplifier itself can be tailored to the needs of the experiment to allow the detection of smaller currents. This is subject to ongoing development [83, 131]. In addition, it is possible to install acousto-optic modulators or in case of the UV-laser a Pockels cell to amplitude modulate one or multiple lasers. A lock-in amplifier can then be employed to increase the signal to noise ratio. This can also be used to remove possible offsets on the current signal. The offset current is generated by charges which are not produced by the Rydberg excitation but by different mechanisms which have been discussed in [71]. Future improvements on the cell design may also include noise analysis and shielding of the cell to further reduce external influences on the signal.

If this spectroscopy technique is used for trace gas sensing the amount of nitric oxide inside the cell will be very small in a large background of nitrogen. Therefore, the most efficient excitation path is needed to achieve as much population in the Rydberg state as possible. The large number of rotational levels in each electronic state gives rise to a multitude of different excitation paths that can be addressed with the employed laser systems. In principle, it is possible to simulate different excitation schemes with the optical Bloch equations. However, there is a lack of accurate literature values concerning the necessary simulation parameters. Thus, it may be necessary to test the different paths experimentally with the other experimental parameters fixed. This will also require precise control of the beam overlap.

One benefit that was stated in [10] is that the sensor is immune to light fluctuations as long as the transitions are driven in saturation. This has to be tested for the chosen excitation path as well. For the $\mathrm{A}\,^2\Sigma^+ \leftarrow \mathrm{X}\,^2\Pi_{3/2}$ transition information on this can be retrieved from optical spectroscopy which also enables the precise investigation of the states sub structure. These investigations are discussed in detail in chapter 6.

Eventually also the transition to the Rydberg states and the assignment of the Rydberg states is needed to optimise the spectroscopic signal. The investigation of the Rydberg states and their behaviour in electric fields is subject to current investigation [81].

6 Doppler-free spectroscopy within the γ_{00}–band in nitric oxide

Introduction

The hyperfine structure of nitric oxide has already been investigated in several studies. Microwave spectroscopy was the preferred tool of early studies on the hyperfine structure of the ground state reported in [29, 132–135]. The corresponding hyperfine constants of the ground state $X\,^2\Pi$ were later determined precisely by employing infrared spectroscopy [33, 35]. The hyperfine structure of the excited state $A\,^2\Sigma^+$ was first investigated experimentally by Bergeman and Zare [30]. Two-colour resonant four-wave mixing [34] as well as quantum beat spectroscopy [31, 32, 36, 136] enabled the determination of hyperfine constants for the $A\,^2\Sigma^+$ state.

However, the direct resolution of Lamb-dips was not possible so far, since it requires narrowband continuous wave laser systems. We employed our frequency quadrupled Ti:sapphire laser to perform Doppler-free saturated absorption spectroscopy on the $A\,^2\Sigma^+ \leftarrow X\,^2\Pi_{3/2}$ transition. The technique should give information about dynamic constants like the saturation intensity and state life times. Precise Knowledge of these constants can be used to optimise the sensing scheme introduced in section 2.3.

This chapter will guide through the process of signal search and optimisation which was also presented in [137]. In addition, it will present the spectroscopic results reported in [1]. First the experimental setup will be introduced in section 6.1 and the signal optimisation process will be summarised in section 6.2. These two sections can be seen as a guide on how to approach this challenge, when one seeks to employ Doppler-free saturated absorption spectroscopy on a different ground state transition in nitric oxide or even another molecule.

The middle part of the chapter will deal with the high resolution measurements on the hyperfine structure of different transition belonging to the P_{12ee} branch, which can also be found in [1]. In addition, data measured at a lower pressure is discussed in section 6.4 and the linewidth of the different datasets in section 6.5. It ends with a conclusion and outlook on the further potential of Doppler-free saturated absorption spectroscopy in section 6.6.

6.1 Experimental Setup

The spectroscopic setup for Doppler-free saturated absorption spectroscopy in nitric oxide is depicted schematically in figure 6.1. It is based on the primitive setup introduced in section 2.4. The beam of the UV-laser is power stabilised with a motorised half-wave plate [130]. For that, a small fraction of power from the laser beam is picked off, using a glass plate. The picked off light is sent to a photodiode which is connected to a micro-controller (Teensy). The teensy controls a stepper motor rotating the first wave plate in the setup so that the measured signal on the photodiode stays constant. Since the signal quality depends on the power in the pump and probe beam, power stability is vital to achieve the best signal quality throughout a measurement.

The UV-beam is separated into the pump and probe beam with a polarising beam splitting cube. Both beams are widened with two planoconvex lenses each. Their focal lengths are given in mm in figure 6.1. The pump beam has a diameter of around 3.5 mm in front of the cell and the probe beam a diameter of around 2.8 mm. Since both beams are of rather elliptical shape, these value should be considered as estimates. The larger size of the pump beam simplifies the adjustment of the beam overlap, which is crucial to obtain an optimal signal. In addition, larger beam diameters ensure small transit time broadening. With equation 2.15 one can estimate the expected transit time broadening. The mean free velocity of NO at 293 K is

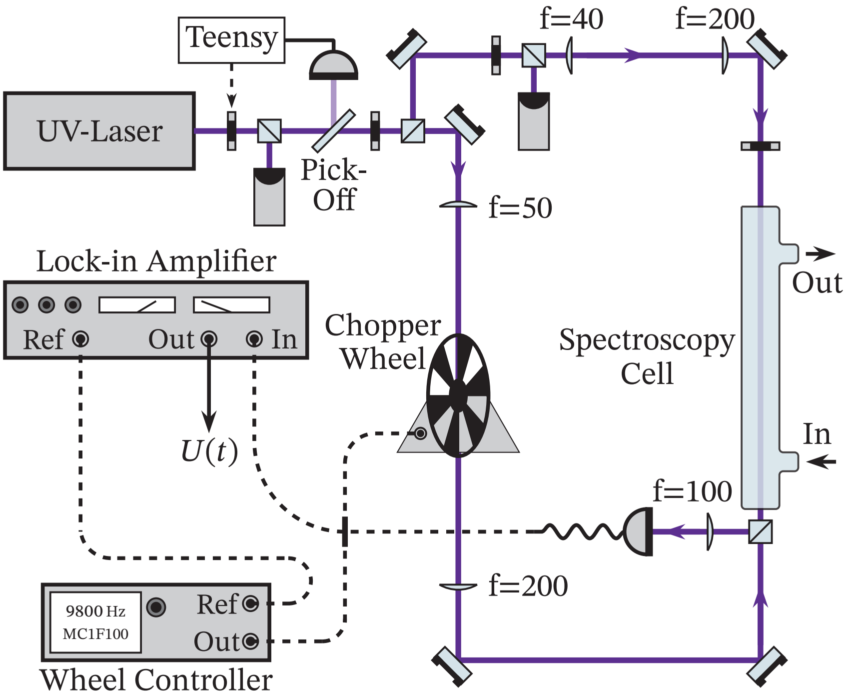

Figure 6.1: Schematic of the full setup for Doppler free saturated absorption spectroscopy on the $A\,^2\Sigma^+ \leftarrow X\,^2\Pi_{3/2}$ transition in nitric oxide. Throughout the optimisation process for the signal different spectroscopy cells have been employed. The best spectroscopic resolution was achieved with a 50 cm long through-flow cell. Details on the setup are given in the text.

$\bar{v}_{\mathrm{NO}} = 454.74\,\mathrm{m\,s^{-1}}$ according to equation 2.16. The resulting transit time broadening for a beam with a diameter of 2.8 mm is then 191.2 kHz. This is small compared to the overall linewidth of the measured data presented in section 6.3. The two beams are overlapped inside the spectroscopy cell with crossed linear polarisations. After passing through the cell the probe beam is focused on a photodiode (Thorlabs PDA25K2).

The pump beam is amplitude modulated at 9.8 kHz by a chopper wheel. A Doppler-free signal will only be obtained when the pump beam is unblocked. Feeding the signal of the probe beam to a lock-in amplifier, as well as the reference signal from the wheel controller, enables the lock-in to significantly increase the signal to noise ratio of the measured signal. A detailed introduction to the technique can be found in [138]. The basic principles of the underlying electronics can be found in [139] and technical introduction in [140] where also some applications for lock-in amplifiers are discussed.

For the measurements presented in section 6.3 and published in [1] a 50 cm long through flow glass cell was used. The cell has angled windows to minimise back reflections of the pump beam onto the photodiode. During the process of signal search and optimisation different types of cells were tested. However, the 50 cm cell produced the best signal amongst the different cells. It has the advantage that one can work at relatively low pressures (1.0×10^{-2} mbar to 1.0×10^{-4} mbar) but still gains a decent signal due to the longer distance at which absorption of the laser beam takes place. The precise control of the pressure and flow is ensured by the mass flow controller setup, which was introduced in chapter 4. For any type of cell the beam overlap is crucial for the signal quality and has to be optimised carefully. This can be done by looking at the single shot signal of the Lamb-dip. For weaker transitions, a single shot signal is not visible. In such cases one has to rely on opto-mechanical tools like irises.

When scanning the laser over resonance, the resulting spectra suffer from its frequency jitter. Especially if several scans are averaged the spectra smear out. One way to counteract this is to stop the data acquisition and manually correct the frequency position of the laser by comparison to a reference signal. This can be for example the error signal of the PDH-lock with respect to the trigger signal of the scan. This method was used in [137] and for the measurements presented in section 6.2.

However, the method is time consuming and can not fully remove the effect of the frequency jitter.

For the measurements presented in section 6.3 and section 6.4 the UV-laser was locked to a certain frequency and the lock frequency was changed step by step, moving the laser slowly above resonance. For each frequency step a single data-point from the lock-in amplifier was taken. In comparison to scanning the laser over the resonance this technique ensures a higher frequency stability, i.e. a higher resolution.

In detail, this technique works as follows. The UV-laser is locked onto a tunable sideband at frequency $\Delta\omega_{\mathrm{EOM}}$. This frequency can be tuned from $\Delta\omega_{\mathrm{EOM}}/2\pi = 35\,\mathrm{MHz}$ to $\Delta\omega_{\mathrm{EOM}}/2\pi = 500\,\mathrm{MHz}$. In contrast to the sidebands necessary to generate the PDH-error signal are set to a fixed frequency of $\omega_{\mathrm{PDH}}/2\pi = 15\,\mathrm{MHz}$. The free spectral range of the corresponding transfer cavity is $\mathrm{FSR}_{904} = 897.4\,\mathrm{MHz}$, so that the full range in between two cavity fringes can be covered by the EOM-sidebands. The locked laser can be moved over the resonance by changing the frequency ω_{EOM}. For each frequency step a single data point is generated by integrating the signal for a specific time via the lock-in amplifier. For the finest scans the frequency step size in the UV was set to 0.4 MHz and the integration time of the lock-in amplifier to 10 s. In advance of taking a spectrum at high resolution the respective lamb-dip has to be searched in the vicinity of the center of the Doppler-broadened line. To do so, the laser is locked next to the center of the absorption feature and moved over the resonance in larger frequency steps, for example 2 MHz. For the signal search also the integration time of the lock-in amplifier can be set to a smaller value, like for example 1 s.

6.2 Optimisation of the spectroscopic parameters

This section is supposed to aid future researchers with the process of signal optimisation. For a system were the saturation intensity is not perfectly known to the experimenter finding a Doppler-free signal with the technique of saturated absorption spectroscopy is not always fully straight forward. The saturation intensity was given in equation 2.19. It includes the life time τ of the excited state. Thus, if the life time of the excited state is known the saturation intensity can be estimated. In the case of nitric oxide there are several values for the life time of the excited state. Callear [141] gives a mean radiative lifetime of 2.3×10^{-7} s for the $A\,^2\Sigma^+$, $\upsilon_A = 0$ state. In contrast to the data of [142] a radiative lifetime of 9.98×10^{-7} s for transitions from $\upsilon_A = 0 \leftarrow \upsilon_X = 0$ can be calculated. While [143] gives 7.2×10^{-8} s and from [144] one can calculate the state life time to be 1.08×10^{-6} s. These values suggest that the saturation intensity is in the range of 0.016 mW mm^{-2} to 0.25 mW mm^{-2}. For the aforementioned estimated size of the pump beam this would require at least laser powers between 1.5 mW and 2.4 mW

However, it is very important to keep in mind that collisions will influence the required saturation intensity. As introduced in section 2.4.3 the saturation intensity does not solely depend on the natural linewidth Γ. Thus, if the pressure is to high, the large number of collisions will reduce the lifetime of the excited state. Effectively this means that, the higher the pressure, the more laser power is necessary to saturate the transition. Of course, if the pressure is chosen too low, saturation will be achieved easily with the pump beam, but the remaining change in absorption for the probe beam might be difficult or impossible to detect. In this case the absorption can be increased without increasing the pressure by using a longer spectroscopy cell. This is one of the reasons why, during the process of signal optimisation, different gas cells were employed. Collisions were identified to already limit the spectroscopic resolution in the 8 cm cell used in the beginning. In the subsequently used 10 cm cell the limitation stayed almost the same. Therefore, the 50 cm cell introduced in section 6.1 was manufactured. In this cell there is still enough absorption to obtain a decent signal even at pressures in the range between 1×10^{-2} mbar and 1×10^{-4} mbar. In the shorter cells pressures around 0.6 mbar were typically used.

The first attempts to find a Lamb-dip signal have been conducted without a lock-in amplifier. Several different settings for pressure and laser power were tried out employing the 8 cm long gas cell depicted in figure 6.2, without any electrodes inside. Since these attempts to find the respective Lamb-dip signal failed, a lock-in amplifier was employed. This device can improve the signal to noise ratio of the data by orders of magnitude. So that signals, that would otherwise vanish in a large background of noise, emerge. However, it also adds additional complexity to the experiment and

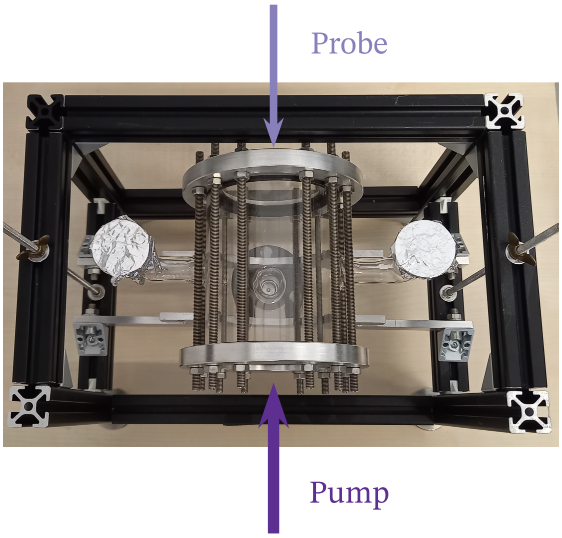

Figure 6.2: Top view of the cell used for the first Doppler-free measurements. Pump and Probe beam are indicated by arrows. The probe beam is depicted in a lighter color to symbolise its lower intensity.

requires to carefully choose the respective time constants which are the modulation frequency and integration time. This is later discussed in more detail.

The first measured Lamb-dip signal is depicted in figure 6.3 for different numbers of averages. One sweep corresponds to a single scan of the laser over resonance. The data was taken at a pressure of 6.3 mbar. The pump laser was set to a power of 24 mW, the probe laser to 20 µW. To obtain spectra with so many averages the laser's frequency position had to be corrected every few sweeps to avoid blurring of the signal, as described in the previous section. The data also had to be offset corrected. A large offset despite the usage of a lock-in amplifier indicates that there is a large amount of light from the pump beam hitting the photodiode, since any other light hitting the detector is not modulated and should be filtered out. Since the cell windows are not anti-reflection coated, back-reflections from the pump laser were expected to appear. To avoid them hitting the detector the cell can be put into the setup at an angle. However, this leads to stress on the flange connections to the steel hoses. Therefore, later cell generations where manufactured with angled windows.

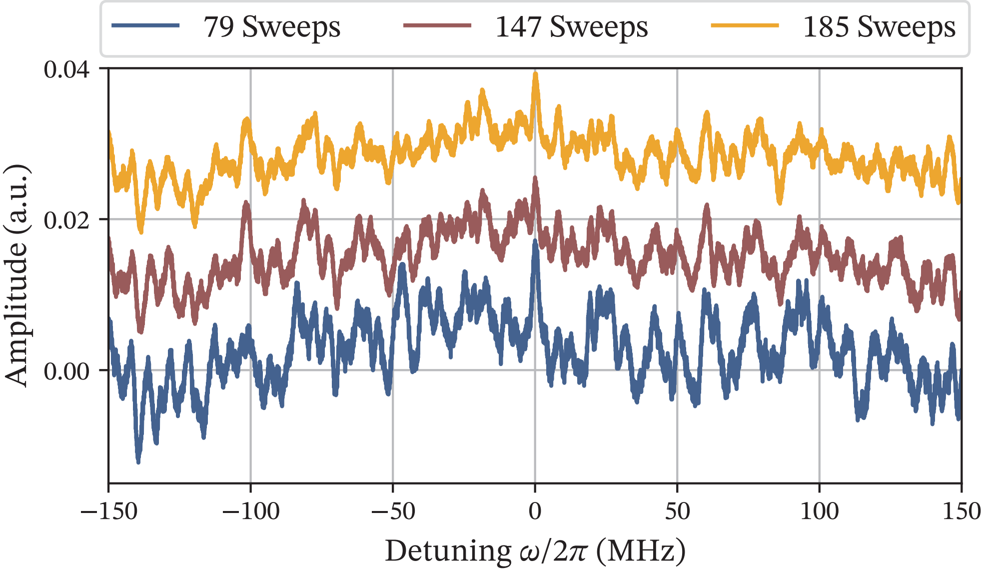

Figure 6.3: First measured Lamb-dip signal for a different number of averages. The Lamb-dip was set to zero detuning. Each dataset was offset corrected but for clarity the datasets are depicted with an offset with respect to each other.

In addition back-reflections can be minimized by elongating the distance between the cell and the detector and built in irises to block all light except the probe beam itself.

The frequency axis for this dataset and all others presented in this section has been calculated from the scan time of the laser. For example if the UV-laser scans 250 MHz in 10 seconds, the time axis from the oscilloscope was converted into frequency based on that value. This method is inaccurate and relies on the laser scan to be linear and to agree with the scan distance set in the control interface. To check if the latter is the case a calibration measurement was conducted were the error signal of the lock of the UV-laser was used as a frequency reference. The evaluation showed that the set value of the scan distance and the actual scan distance deviate. Fitting the behaviour of the deviation results in a correction factor for the different scan settings. The corresponding evaluation and calculation of the correction factors can be found in [137]. This correction factor has been included in the frequency scaling of the datasets shown in this section. This is still not very accurate but since this section deals with the improvement of the signal quality and not with the quantitative determination of frequency shifts or molecular constants, it is sufficient.

The first signal was only visible after a considerable amount of averages. Despite the averaging the overall signal quality was low, with background noise in the same order of magnitude as the signal. Therefore, it is worth to try out different parameters to optimise the signal. Even an improvement by a factor of 1.5 or 2 may reduce the number of necessary averages significantly. Especially in the beginning, when the signal is not visible in single shot, the optimisation procedure is time consuming, since it takes a number of averages to evaluate if the parameter changes one made, improved the signal quality.

Setting the correct laser power for pump and probe is crucial. Therefore, after a first signal is present it is worth to try out different power ratios and absolute values. It is very important to keep a significant intensity difference between the pump and probe laser. If the probe laser is to strong or the pump laser to weak the technique does not work. An intensity difference of around one order of magnitude is a good rule of thumb. If this does not work one can go to more extreme ratios. Here it may be beneficial to first increase the pump power, since one has to make sure that the pump's intensity is close to saturation. If increasing the pump laser does not show any effect, the transitions may already be saturated and one should go on with the probe laser to check if its intensity is either too high or too low. In case of this experiment the probe laser intensity was very low when the first signal was obtained. In such a case it is very difficult to detect the change in probe absorption induced by the pump laser. If the probe laser power is set to high, it may be able to saturate the transition itself.

When optimising the laser powers of the pump and probe laser one should also keep in mind the beam diameters of both lasers. Since in the end not the power but the intensity is crucial. It is beneficial if both beams have roughly the same diameter, to obtain a large volume for which the two beams overlap.

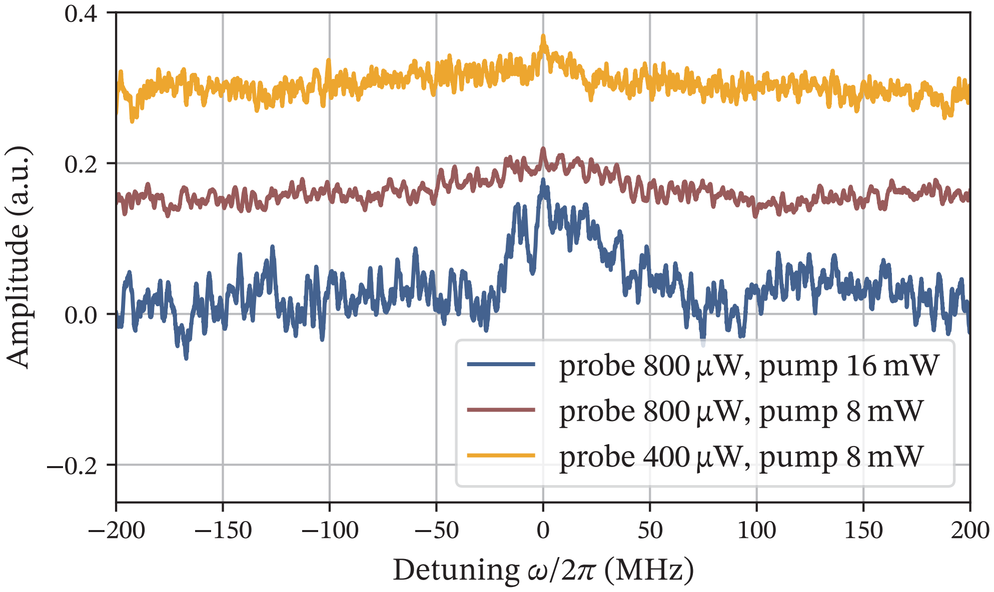

Figure 6.4: Traces illustrating the effect of different pump and probe laser powers. The three traces were measured with different numbers of averages.

In figure 6.4 three signals are depicted. They have been taken with a different number of averages so that the noise level is not comparable. However, they illustrate the influence of the pump and probe power on the signal behaviour. The blue signal has the highest pump and probe power and also the highest amplitude. The power ratio is the same as for the red signal. The yellow one was taken at the same pump power as the red one but only half the power of the probe laser has been used. This decreases the signal amplitude significantly. All three spectra were measured in the cell depicted in figure 6.2. This type of cell has particularly thick windows, so that the loss of power due to absorption and reflection from the cell windows is quite high compared to other cells (up to 30 %).

In addition, to the aforementioned time constants the phase setting of the lock-in amplifier is important. Due to experimental imperfections, electronic delays and the travelling distance of the signals, the reference signal fed to the lock-in amplifier and the signal fed from the experiment to its input, can be out of phase. To obtain the best signal to noise ratio the phase setting of the lock-in amplifier has to be chosen so that the phases of the reference and input signal match each other. If they are exactly 90° out of phase the signal even vanishes completely. This is illustrated in figure 6.5.

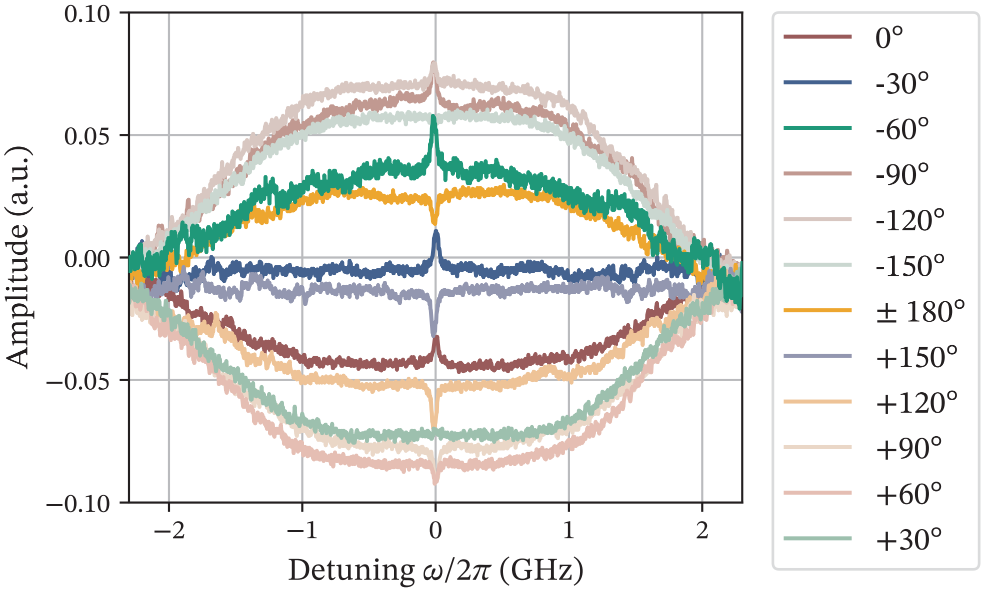

Figure 6.5: The spectroscopy signal measured at 21.5 mW pump and 800 µW probe with a cell pressure of 6.5×10^{-1} mbar for different phase settings of the lock-in amplifier.

The figure shows several scans over the resonance, all recorded at the same parameters. The lock-in phase was varied in steps of 30°. A change of 180° corresponds to a flip of the signal from positive to negative amplitude. This can be seen by comparison of the trace for −30° and 150°. That an incorrect choice of the phase may remove the Lamb-dip from the signal is illustrated by the traces at 30° and −150°. Most of the traces show a large absorption background in which the Lamb-dip appears. This is due to additional light from the pump beam hitting the detector after passing through the cell. Light of the pump beam that is reflected without passing through NO leads to a constant offset without the absorption profile. That it is possible to reduce the absorption background to zero, indicates that the signal generated by the additional light of the pump beam on the detector has a different phase then the signal generated by the probe beam. Furthermore, the figure illustrates that only at two distinct phase choices the signal vanishes completely, for all others its amplitude may be decreased in comparison to the maximum possible amplitude, but the signal in general is still visible. The largest signal amplitude is obtained at a phase of $-60°$. The difference to the phases where the signal is completely suppressed is 90°. This illustrates, that when searching the first signal it is useful to change the phase by 90° from time to time and check if this changes the output signal. This avoids that the signal search is performed at a phase setting where the signal is fully suppressed. If the setting is at the worst possible value, a 90° phase change would theoretically set it to the optimum. Conclusively the fine adjustment of the phase is only possible, after a first signal has been found.

As already mentioned, the setting of the time constant of the lock-in amplifier, sometimes also denoted as integration time, has to match the other time constants of the experiment. In this particular case, one is only interested in the Doppler-free signal. Thus the lock-in is employed to suppress noise on the signal. For other use-cases the requirements on the settings of the lock-in may be entirely different. This should be kept in mind. To illustrate the importance of the correct settings of the time constants, in the following, an example is discussed.

One may assume that the frequency of the amplitude modulation of the pump laser is 1 kHz. Thus, a single modulation step, i.e. turning the laser on and off, takes 1 ms. For this application the requirement for the integration time of the lock-in amplifier is, that it has to be larger than 1 ms. Otherwise the noise suppression would not work as desired. Of course, one could now just use an integration time of half a second, i.e taking into account 500 modulation cycles, which would give a very good filtering effect and consequently good noise suppression. However, there is another limitation which is the scan speed of the laser. If one assumes that the laser scans 1 GHz per second the lock-in would deliver only two data points at this setting, since it will integrate the signal fed to it’s input for half a second. The result is then, that the frequency resolution of the detection is limited to 500 MHz. Thus, to increase the resolution one can either scan the laser slower or decrease the integration time, which effectively may also decrease the signal to noise ratio if one cannot increase the modulation frequency, i.e. the number of modulation cycles that the lock-in integrates over. As a consequence the scan speed of the laser, the integration time and the modulation frequency of the pump laser have to match each other. The limit of the modulation frequency is thereby either given by the respective device or the bandwidth of the detector. The maximum modulation frequency of the employed chopper wheel is 10 kHz. From the data for the state life time given above one can very coarsely estimate that the linewidth of the Lamb-dip has to be in the range of MHz to tens of MHz. Thus the time constants were chosen so that the obtained frequency resolution was inside this range.

If the parameters of the lock-in have been set to suitable values a simple change of the scanning speed of the laser may increase the resolution. Scanning slower while keeping all other time constants fixed will not cause any problems for the detection. The effect of lowering the scan speed on the signal is depicted for an exemplary measurement in figure 6.6. At the highest scan speed the signal is broadened and the line-shape is edgy and neither Lorentzian nor Gaussian. Lowering the scan speed decreases the width of the signal and its line shape is rounder. At a scan speed of 240 MHz s^{-1} the signal seems to split into two parts, that could not be fully separated. At even lower scan speeds the signature of this splitting gets clearer. That the signal consists of more than a single Lam-dip was later confirmed, when the signal quality and method of measurement were fully optimised (see figure 6.7). The reduction of the scan speed effectively allows a higher sampling rate, i.e. a clearer signal.

It may happen, that even though a lock-in amplifier is employed, that there is still noise on the signal. It has been mentioned several times that this may be generated by additional light of the pump beam on the detector. But what if this can be ruled out and there is still some noise remaining? A simple Fourier analysis of the signal may help then. The Fourier transformation of the signal fed to the lock-in amplifier will reveal which frequencies are contained in it. If there is any frequency which is close to the modulation frequency it may partially or fully pass through the lock-in amplifier, disrupting the output signal. The problem can be solved by choosing the modulation frequency so that it is in a part of the frequency spectrum, where there are no or only very small contributions from other sources. There can be plenty of

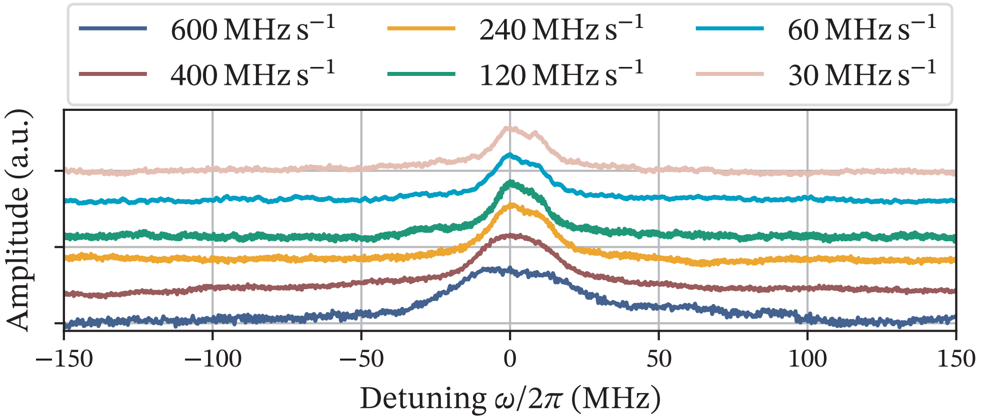

Figure 6.6: Lamp-Dip spectra measured at identical experimental parameters and lock-in setttings but at different scan speeds of the UV-Laser. All spectra have been averaged for 25 sweeps.

reasons for such additional noise frequencies. In the case of the UV-laser system a typical source for that type of noise may be the locking systems of the two employed doubling cavities. They can easily produce tiny amplitude fluctuations in the kilohertz regime. Since most modern oscilloscopes offer a FFT-function (Fast Fourier Transform), such an analysis can be done within a few minutes and should always be considered as a quick check if the choice of modulation frequency is correct or may have to be optimised.

As a final remark on signal optimisation for Doppler-free saturated absorption spectroscopy the importance of the beam overlap has to be stressed. If the signal quality is suddenly very poor, one should always check the beam overlap first, since a poor beam overlap cannot be compensated by any of the other parameters. If the beams overlap at an angle they may also not fully cancel out the Doppler-broadening so that a residual broadening remains. The best way to optimise the beam overlap after initial alignment with two irises for example, is usually to look at the signal and adjust it carefully until it reaches maximum amplitude.

6.3 Determination of the hyperfine constants for the A $^2\Sigma^+$ state

The measurements presented in this section were conducted after the signal optimisation process, that has been treated in the previous section, was finished. The measurements were performed with the 50 cm long spectroscopy cell and the beam diameters given in section 6.1. The pressure inside the cell was set to be 0.023 mbar and data was collected for total angular momenta from $J_\mathrm{X} = 1.5$ to 19.5 on the oP_{12ee} branch (see also figure 2.3). The modulation frequency of the chopper wheel was set to 9.8 kHz. The laser powers were 4 mW for the pump and 0.4 mW for the probe laser. To determine the hyperfine constants of the A $^2\Sigma^+$ state it is necessary to resolve at least two of the expected hyperfine transitions, since the frequency splitting between different transitions is required to determine the respective constants.

In figure 6.7 spectra for different total angular momenta J_X between 19.5 and 5.5 are depicted. The data has been offset corrected and fitted with a Voigt profile which will be introduced later in this chapter (see equation 6.1, 6.2 and 6.3). The peak labelled as ③ has been set to zero detuning. However before the the data is analysed quantitatively a qualitative discussion will be given.

It is immediately apparent that the frequency splitting between the three individual transitions, that have been resolved, shrinks with decreasing total angular momentum J_X. For $J_\mathrm{X} = 5.5$ only two individual transitions have been resolved. The peaks labelled ① and ② have moved so close to each other that they cannot be resolved individually anymore.

For lower values of J_X the remaining two lines, labelled ②, ③ move even closer to each other until they merge too, so that for $J_\mathrm{X} = 2.5$ and $J_\mathrm{X} = 1.5$ only a single line is resolvable. This is depicted in figure 6.8. In addition, new spectroscopic features appear in the spectra for $J_\mathrm{X} = 3.5$ detuned to the blue of ③ and for $J_\mathrm{X} = 2.5$ a double-peak occurs red detuned to the only remaining spectroscopic line. Furthermore, a change in relative intensity between the lines is observed. For $J_\mathrm{X} > 5.5$ all lines have been of almost the same amplitude. For $J_\mathrm{X} = 5.5$ peak ② is higher than ③. This may be explained by the lack of resolution, since peak ② consists actually of two peaks.

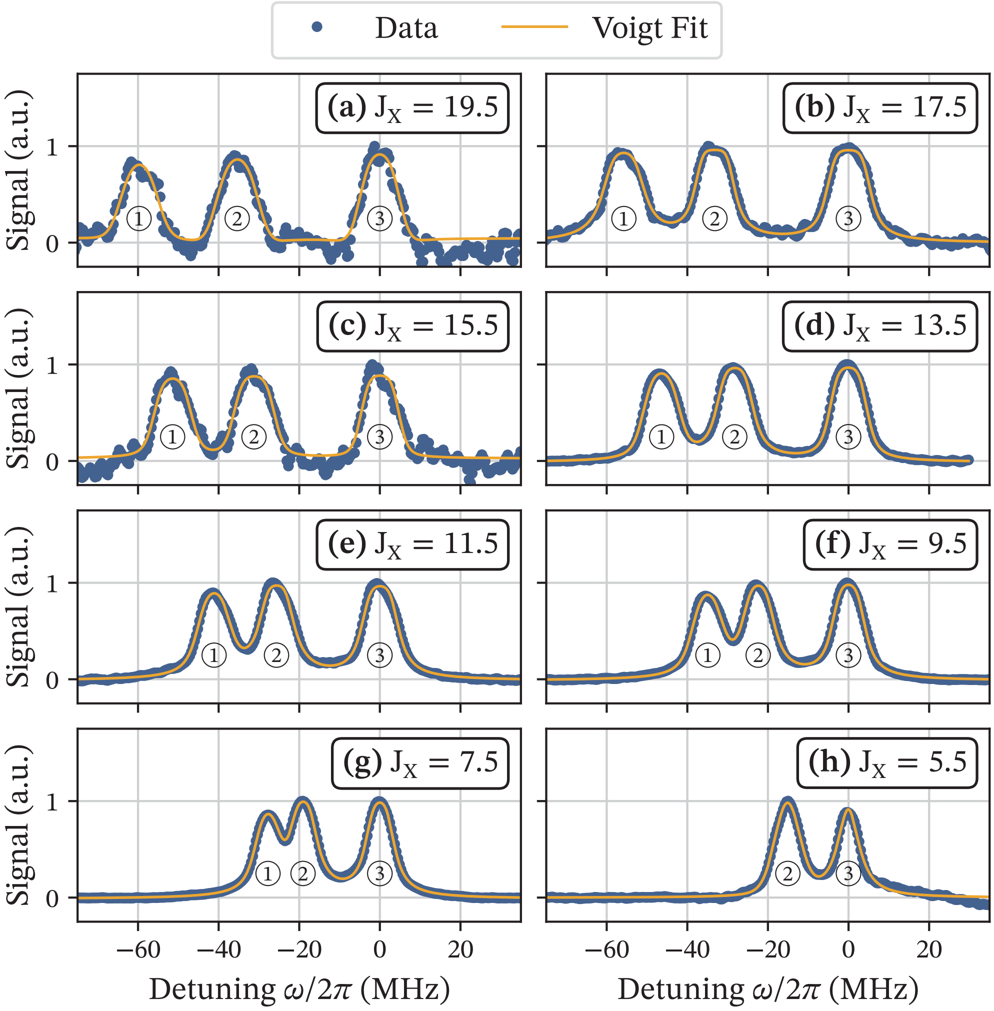

Figure 6.7: Selection of hyperfine spectra for different total angular momenta $J_X = 19.5$ to $J_X = 5.5$. The data is shown in blue and fitted with a Voigt profile which is drawn in orange.

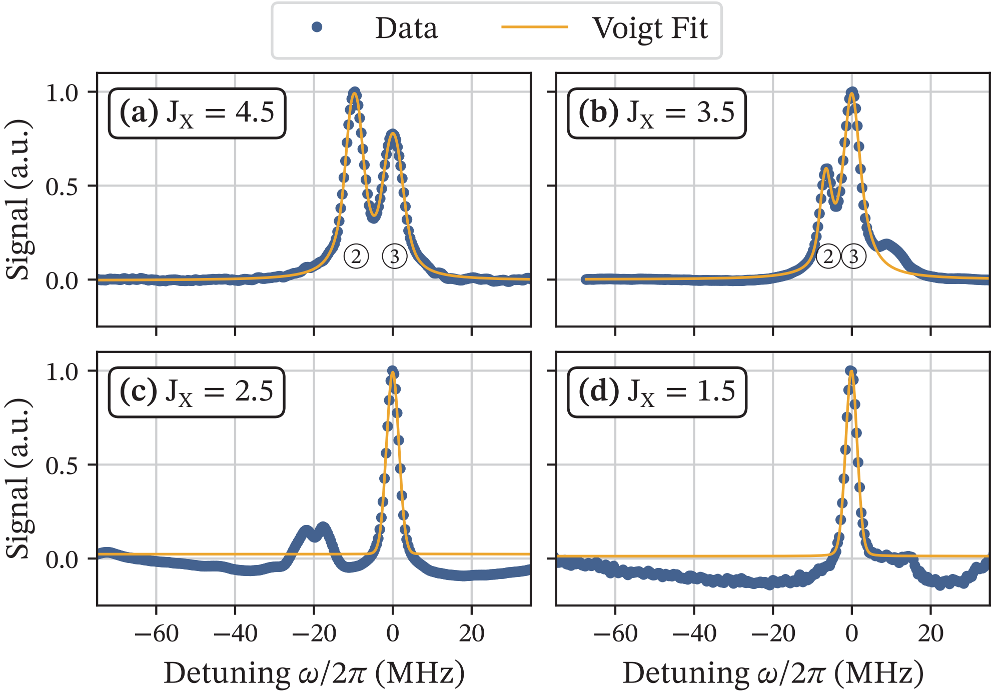

Figure 6.8: Hyperfine spectra for the lowest four values of J_X. Despite the merging of ② and ③ additional smaller peaks occur. The data is shown in blue and fitted with a Voigt profile drawn in orange.

However, the intensity difference increases further for $J_X = 4.5$ and eventually flips for $J_X = 3.5$.

This behaviour is in comparison to the behaviour of the spectra for higher J_X unusual. If only a single peak is visible, the exact assignment of the ΔF transitions is difficult. It would require a very precise absolute frequency reference. The employed frequency reference for tuning the fundamental of the UV-laser to the different J_X transitions was a wavemeter (Burleigh WA-10). A simulation conducted with the program PGOPHER [145] does not show any additional spectroscopic lines in the close vicinity of the main transitions in contradiction to the spectra for $J_X = 3.5$ and $J_X = 2.5$.

As explained in section 2.2.1 the ground state of nitric oxide belongs neither strictly to Hund's case (a) or (b). For low J-values it is best described as a Hund's case (a) which means that the Hund's case changes, when an electron is moved from the $X\,^2\Pi_{3/2}$ state to the $A\,^2\Sigma^+$ state. A possible explanation could than be that a change of the Hund's case may weaken the parity selection rules, so that additional transitions, emerge. However, according to [38] parity selection rules are very strict and hold for both involved Hund's cases (see also section 1.6). Thus, the given explanation is not sufficient. Additionally, if the explanation would be valid, one would expect the simulation to show corresponding peaks in the calculated spectrum, which it does not. To fully understand the behaviour of the spectra for low J-values further investigation is necessary. It would be beneficial to conduct it at a higher resolution, to obtain more clarity and correctly assign the individual transitions.

Since the behaviour of the data for low J is not fully understood and it is clear that from $J_X = 5.5$ downwards two peaks of the spectrum have merged, i.e. the extracted peak position is not exact, those datasets are excluded from further quantitative analysis. Before the quantitative analysis and determination of hyperfine constants is discussed, it is necessary to explain why only three individual transitions have been resolved, since the selection rules $\Delta F = \pm 1, 0$ allow a total of six hyperfine transitions for each total angular momentum J_X. This is illustrated in figure 6.9 for the transition $A\,^2\Sigma^+\ J_A = 5.5 \leftarrow X\,^2\Pi_{3/2}\ J_X = 6.5$. There are three transitions with $\Delta F = -1$ which are indicated by blue arrows, two with $\Delta F = 0$ and a single one with $\Delta F = +1$. The latter two are indicated by black arrows. The simulation with PGOPHER yields exactly the depicted six hyperfine transitions. The reason why

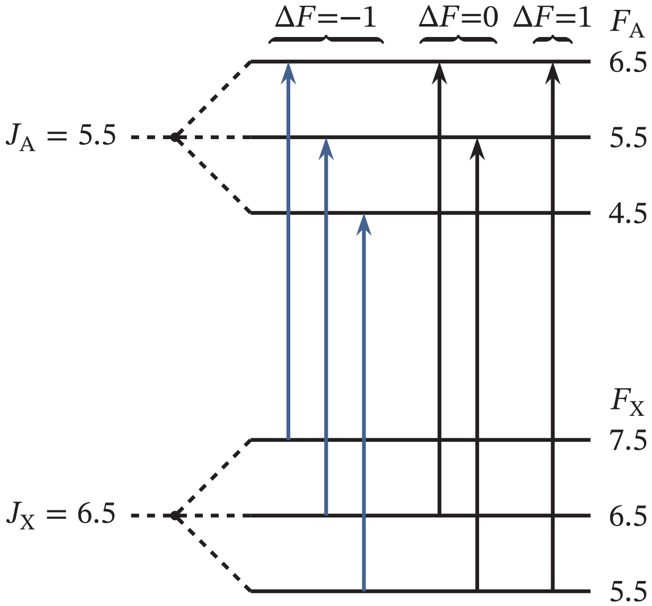

Figure 6.9: Schematic for a exemplary transition from $J_\mathrm{X} = 6.5$ in the X $^2\Pi_{3/2}$ state to $J_\mathrm{A} = 5.5$ for the A $^2\Sigma^+$ state including the hyperfine structure. The six expected hyperfine transitions are indicated as arrows. The blue arrows indicate those transitions with $\Delta F = -1$ which are, according to the simulation, by far the strongest.

only three of the six transitions are visible is their difference in line strength. The $\Delta F = -1$ transitions are for any total angular momentum J_X the strongest three. The other three transitions are usually at least a factor of ten but often, especially for $\Delta F = 1$ a factor of 100 weaker. The calculated intensities include the transition strengths and thermal distribution of the rotational levels. In case of the depicted transition for example, the calculated intensity of the $\Delta F = -1$ lines is on the order of 1×10^{-4}, for the $\Delta F = 0$ it is already on the order of 1×10^{-5} and for the single line with $\Delta F = +1$ it is on the order of 1×10^{-7}. For larger J_X the intensity difference tends to become even stronger. For $J_X = 15.5$ the $\Delta F = -1$ lines are a bit weaker then for lower J_X with intensities around 1×10^{-4} and 1×10^{-5} while the $\Delta F = 0$ lines only show intensities on the order of 1×10^{-7} and the $\Delta F = +1$ has only an intensity on the order of 1×10^{-10}. Since the three observed lines, are of very similar intensity it is most likely the case that only the $\Delta F = -1$ transitions have been resolved, since the other three transitions would require way more laser power to get close enough to saturation with the pump laser to be observed.

One way to check if the assumption that only $\Delta F = -1$ transitions were resolved is correct, is to calculate the splittings between the lines from the data and simulation and compare them to each other. If the assumption is wrong the splittings should not match each other. To determine the line splittings the data has been fitted with a Voigt-profile in an Lambert-Beer envelope, which is depicted as orange line in figure 6.7. The Voigt profile was introduced in 1912 [146] and is a convolution of a Lorentzian and Gaussian function. Thus it cannot be solved analytically. To fit a Voigt profile one can either use a pseudo-Voigt function or a numeric approximation of the respective profile. The later is considered to be more accurate and employs the Faddeeva function $w_k(z)$, which is given by

$$w_k(z) = \exp(-z^2)\left(1 + \frac{2i}{\sqrt{\pi}}\int_0^z \exp(t^2)dt\right). \tag{6.1}$$

The Faddeeva function's argument z is including the fitparameter f_0 which yields the frequency position of the peak. In addition, it includes the measured frequency

f, and the width of the Doppler profile, which is denoted as σ as well as the corresponding Lorentzian linewidth, which is denoted as γ. It is given by

$$z(f) = \frac{f - f_0 + i\gamma}{\sqrt{2}\sigma}. \tag{6.2}$$

The full fit function takes only the real part of the Faddeeva function and is given by

$$V(z) = A_{\mathrm{LB}} \cdot \left(1 - \exp\left(-1 \cdot \sum_{k=1}^{3} \mathrm{Re}[w_k(z(f))]\right)\right). \tag{6.3}$$

With an overall amplitude A_{LB}. The sum takes into account that a total of three peaks has to be fitted. As previously mentioned below $J_{\mathrm{X}} = 6.5$ the three spectroscopic lines are not individually resolved. Therefore, data for $J_{\mathrm{X}} < 6.5$ is not taken into account in the further evaluation. In figure 6.10(a) the measured splittings retrieved from the fit are compared to the values calculated with the constants given in table C.1.1, C.1.2 and C.2 in the appendix. The circled numbers indicate between which of the two peaks the splitting has been determined. The blue and red data points indicate the data. The errorbars contain the frequency error of the laser locks that was estimated in section 3.3 and the fit uncertainty. The main contribution to the error is the estimated frequency uncertainty. The orange squares indicate the splitting determined from the spectrum calculated with PGOPHER. The calculated and measured splittings are in very good agreement with each other. The hyperfine constants of the ground state of nitric oxide are already determined with high accuracy by infrared spectroscopy [35]. They were kept constant at the values given in table C.1.2. Only the hyperfine constants for the excited state were fitted. To fit the data a wrapper program for the command line version of PGOPHER is used. The wrapper optimises the A $^2\Sigma^+$ state hyperfine constants with a Levenberg-Marquardt algorithm. The fitted constants are then c, b and eQq_0. The Fermi-contact constant b_F can be calculated from b and c with the relation $b_F = b + c/3$ [36]. The splittings calculated from the newly fit constants are plotted together with the measured splittings in figure 6.10(b). In table 6.1 the newly fitted constants, which have also been published in [1], are listed together with previously measured constants. The agreement of the newly determined constants is particularly good with the constants from [36], which were also used for the calculated splittings (see table C.2), shown in fig-

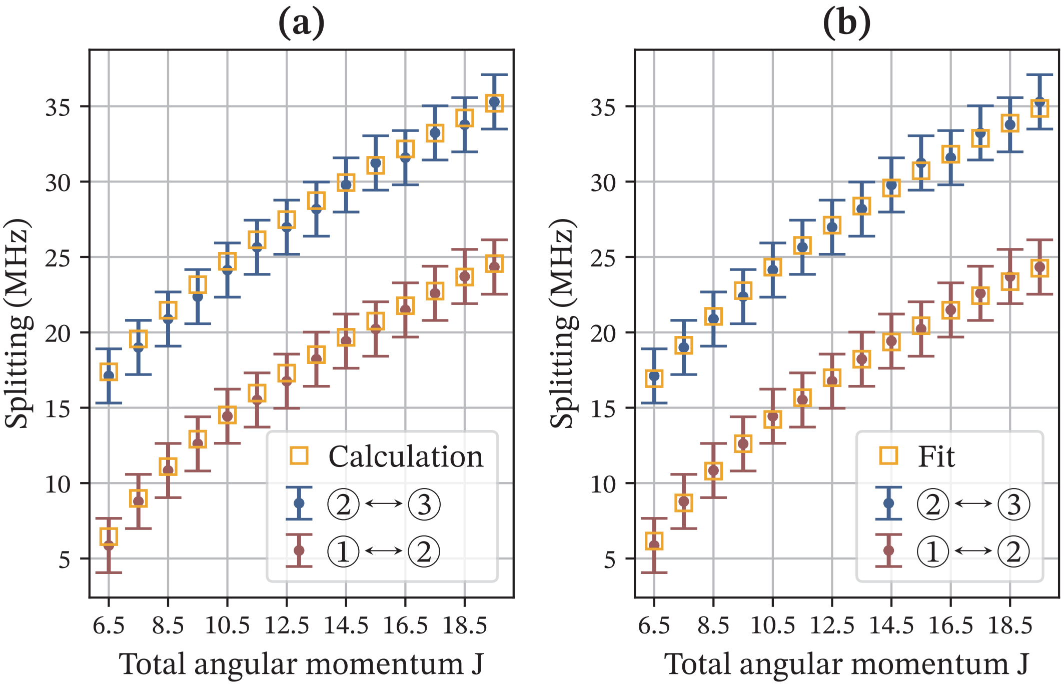

Figure 6.10: (a) Experimentally determined splittings between the different $\Delta F = -1$ hyperfine transitions in red and blue compared to the Calculation plotted as orange squares. (b) Experimentally determined splittings compared to the splittings calculated from newly fitted constants.

Table 6.1: Fitted constants in comparison to other, previously determined constants from experimental and theoretical works. All values are given in MHz.

Constant	Value	Reference	Theor./Exp.
b	41.06(9)	[1], this work	Exp.
	41.66(51)	[36]	Exp.
	41.59(75)	[36]	Exp.
	42.50(8)	[136]	Exp.
c	5.29(53)	[1], this work	Exp.
	5.59(64)	[36]	Exp.
	8.97(107)	[36]	Exp.
	3.01	[136]	Exp.
$\mathbf{b}_\mathrm{F}$	42.82(26)	[1], this work	Exp.
	43.52(30)	[36]	Exp.
	44.56(39)	[36]	Exp.
	53.93	[136]	Exp.
	43.50(8)	[136]	Theor.
$\mathbf{eQq_0}$	−7.31(12)	[1], this work	Exp.
	−7.31(23)	[36]	Exp.
	−7.18(20)	[36]	Exp.
	−4.36	[147]	Theor.
	−6.64	[148]	Theor.
	−5.62	[149]	Theor.
	−4.44(33)	[136]	Exp.
	−6.968	[136]	Theor.

ure 6.10(a). Especially the quadrupole constant eQq_0 agrees perfectly. The newly determined constants fit well into the range of previously determined constants.

6.4 Discussion of crossover resonances

In section 2.4.2 crossover resonances were explained. This phenomenon has not been observed in the measurements presented in the previous section and [1]. For crossover peaks to emerge the two transitions involved in its formation have to be driven close to saturation by one of the two lasers. For the data depicted in figure 6.7 the laser power was supposedly not high enough to drive any of the $\Delta F \neq -1$ transitions close to saturation, so that neither the respective transitions nor the crossover resonances appeared.

First, it shall be discussed where in a measured spectrum crossover peaks are expected to appear. In figure 6.11 the expected hyperfine transitions and crossover peaks for the transition $J_\mathrm{X} = 6.5$ to $J_\mathrm{A} = 5.5$ (see also: figure 6.9) of the $\mathrm{A}\,^2\Sigma^+ \leftarrow \mathrm{X}\,^2\Pi_{3/2}$ transition are depicted. The line spectrum has been calculated with PGOPHER. The blue lines resemble the different hyperfine transitions. The strongest line has been set to zero detuning in accordance with the presentation of the measured data. The intensities have been normalised to the strongest line, so that the relative intensities of the different lines resemble the calculated intensity relations. As previously discussed, the $\Delta F = -1$ transitions are by far the strongest. The $\Delta F = +1$ transition is in this case so weak that it was plotted as a blue dot, since a line resembling its amplitude in contrast to the strongest transition would barely be visible. The red lines indicate the positions were one would expect a crossover peak. The peak positions were calculated from the simulation result of PGOPHER. Their amplitudes were set arbitrarily. The Crossover peaks are separated into two types. The strong crossovers are suspected to appear with larger intensity than the weak crossovers. The reason for that is, that the strong crossovers appear between hyperfine transitions were always one of the $\Delta F = -1$ and $\Delta F = 0$ transitions are involved. The left of the two strong crossover peaks appears between the transitions $\Delta F_\mathrm{A} = 4.5 \leftarrow \Delta F_\mathrm{X} = 5.5$ and $\Delta F_\mathrm{A} = 5.5 \leftarrow \Delta F_\mathrm{X} = 5.5$. The right one appears between the transitions $\Delta F_\mathrm{A} = 5.5 \leftarrow \Delta F_\mathrm{X} = 6.5$ and $\Delta F_\mathrm{A} = 6.5 \leftarrow \Delta F_\mathrm{X} = 6.5$.

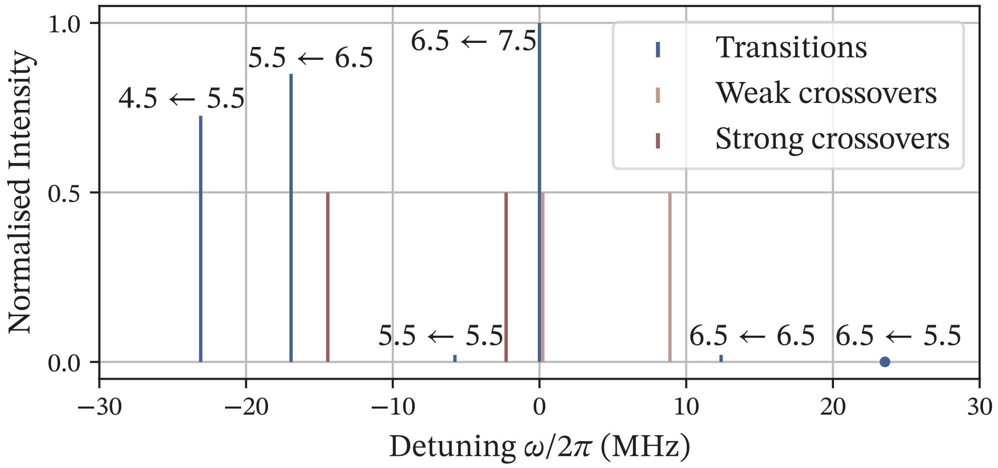

Figure 6.11: Calculated line spectrum for $A\,{}^2\Sigma^+ \leftarrow X\,{}^2\Pi_{3/2}$ for $J_X = 6.5$ to $J_A = 5.5$. The blue lines resemble the different hyperfine transitions. The respective labels indicate this transition in the form $F_A \rightarrow F_X$. The red lines are the expected crossover peaks. A detailed discussion can be found in the text.

The crossovers that are expected to appear with lower intensity are those involving the very weak $\Delta F = +1$ transition. They are depicted in lighter red. One of the two weak crossovers is almost at zero detuning, the involved transitions are $\Delta F_A = 4.5 \leftarrow \Delta F_X = 5.5$ and $\Delta F_A = 6.5 \leftarrow \Delta F_X = 5.5$. The second of the two weaker crossover lines is formed by the transitions $\Delta F_A = 5.5 \leftarrow \Delta F_X = 5.5$ and $\Delta F_A = 6.5 \leftarrow \Delta F_X = 5.5$. It is most likely that this is the weakest of all crossovers since it is the only one that does not involve any of the strong $\Delta F = -1$ transitions. Conclusively, one can expect that the two stronger crossover peaks should appear first, when the spectroscopic resolution is increased, in contrast to the spectra depicted in figure 6.7. Therefore, the weak crossover transitions are from here onwards omitted.

In equation 2.19 the saturation intensity was introduced and it was explained that different broadening effects influence the decay rate Γ. Therefore, one has to consider these effects with an effective decay rate as introduced in equation 2.20 Transit time broadening can be ruled out since the beam diameters have been chosen to avoid large influence of this effect. Therefore, three other broadening effects may be the reason why the missing crossover peaks do not appear. These are residual Doppler broadening, power broadening and pressure broadening.

Residual Doppler broadening is a direct result of an imperfect beam overlap. If the two beams overlap at a slight angle, i.e. the two beams are not perfectly counter-propagating, since pump and probe do not perfectly select the $v = 0$ velocity class. The additional velocity classes then broaden the spectral line slightly. The beam overlap was adjusted by directly observing the spectroscopic signal, i.e. it can be considered to be as well optimised as possible with the employed setup. Further optimisation would require an extension of the setup, including mirrors adjusted by electronic steering and a detection mechanism for the pointing of both laser beams. For practical reasons, it is therefore more feasible to take a look at the other two broadening mechanisms first. Since different powers have been investigated during the process of signal optimisation in the 50 cm cell and the employed pump power of 4 mW is close to the estimated saturation intensity, the limitation is most likely due to pressure broadening. In section 6.2 the limiting influence of this effect was already discussed.

Indeed, it was possible to observe additional spectroscopic features at lower cell pressures. Figure 6.12 shows the result of such a measurement. Effectively, lowering the cell pressure decreases the number of collisions inside the cell which decreases the respective line broadening. The measurement was conducted at the same parameters for the laser power as those depicted in figure 6.7. The modulation frequency was set to 6.5 kHz and the integration time of the lock-in amplifier at 3 s. On the oscilloscope a 5 s running average was performed. These parameters were slightly different but in contrast to the pressure not crucial for the appearance of the additional spectroscopic features. The cell pressure was lowered by two orders of magnitude to 4.86×10^{-4} mbar. Since the strength of the individual transitions decreases with increasing total angular momentum J_X, only lower values of J_X which are also closer to the maximum of the population distribution (see figure 1.4) provide enough signal amplitude for a reasonable measurement. Therefore, a large series of measurements for different values of J_X as presented in section 6.3 could not be conducted at

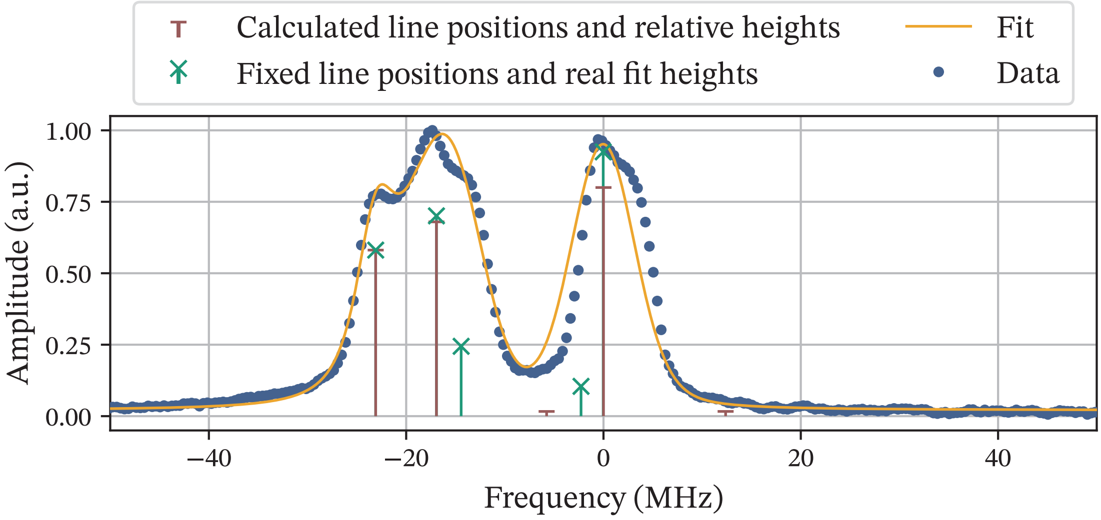

Figure 6.12: Measured hyperfine spectrum for the $\mathrm{A}\,^2\Sigma^+ \leftarrow \mathrm{X}\,^2\Pi_{3/2}$ for $J_\mathrm{X} = 6.5$ to $J_\mathrm{A} = 5.5$. The measurement was conducted at a particularly low pressure. The data was fitted with a Voigt-profile, the line positions of the fit function have been kept fixed to the values predicted from theory, indicated by the green vertical lines. The red lines indicate theoretical line positions of the different hyperfine transitions. More details can be found in the text.

these parameters. In figure 6.12 the data is depicted as blue dots. The measurement was conducted on the same transition as the previously discussed theory spectrum ($\mathrm{A}\,^2\Sigma^+ \leftarrow \mathrm{X}\,^2\Pi_{3/2}$ for $J_\mathrm{X} = 6.5$ to $J_\mathrm{A} = 5.5$). The data was fitted with a Voigt-profile as introduced in equation 6.3, but without the Lambert-Beer envelope. This is justified since at such low pressures the absorption is negligibly small and the exponential function can be ignored. This can be seen by taking a look at the Taylor series of $\exp(-x)$ for $x \to 0$

$$\lim_{x\to 0} \left(\exp(-x) + \Delta x \exp(-x)\right) \approx \Delta x \tag{6.4}$$

However, in contrast to the fit for the datasets discussed in section 6.3, in this case the fit function consisted of five peaks instead of three. The positions of the individual peaks were kept fixed and were not used as free parameters for the fit. The fixed positions for the fit are indicated as green lines in figure 6.12. The fixed positions were retrieved from the simulation with PGOPHER. They are the line positions of the three $\Delta F = -1$ transitions and the line positions of the two stronger crossover peaks. The amplitudes of the green lines resemble the fitted amplitudes. To match the red to the green lines the amplitude of the very left red line was matched to that of the green line. The red lines indicate the theoretical positions of the different hyperfine transitions. The position of the red lines and the measured spectrum were matched at zero detuning. The relative amplitudes between the red lines match the intensity relation given by the calculation.

If one compares the fitted amplitudes (amplitudes of the green lines) with the theoretical amplitudes of the red lines one can see that the relation of the fit amplitudes with each other is similar to the relation between the theory amplitudes. The fit is also describing the data well, even though the line positions were dictated by theory and not free parameters. Especially on the left hand side of the spectrum the agreement is good. It is likely that the triple feature at negative detuning consists of the two $\Delta F = -1$ transitions indicated by the red lines and a crossover peak. In contrast to that the situation on the right hand side, i.e. the double feature set to resonance is contradictory. The amplitude of the second of the two peaks is basically fitted to be zero and the theoretical position of the crossover peak does not fit to the part of the double feature at positive detuning. It was also tried to match theory and experiment by matching the red line at zero detuning to the right peak of the double feature. Then the theory and experiment fit better to each other on the right hand side, but disagree on the left. Overall, the case with the best matching is the one presented here.

The contradiction between theory and experiment clearly indicates that a larger set of data is required. In best case even for a few different transitions. The attempt to reproduce spectra with five instead of three peaks failed. This may be attributed to technical issues, even though during the measurement no issues were noticed. However, an unnoticed miss-calibration of the frequency axis due to problems with the laser lock or mode-hops of the laser could possible have corrupted the data.

6.5 Investigation of the linewidth of the spectra

Apart from the hyperfine constants of the A $^2\Sigma^+$ state the width of the spectroscopic features can be evaluated. However, this dataset has to be interpreted with care. This is the case because the linewidth depends amongst other parameters on the beam overlap between pump and probe. The overlap has been adjusted to obtain an optimal signal before each measurement. Nevertheless, the exact quantification of the beam overlap was not possible in the employed setup. Therefore, beam overlap differences between different sets of data could not be noticed. In figure 6.13 the linewidth is plotted in dependence of the total angular momentum J_X of the ground state. The data was fitted with a semi empirical model, which was introduced in equation 6.3. The Voigt-profile in the Lambert-Beer envelope was estimated numerically (see equation 6.1 and 6.2). The linewidth was determined individually for each peak from the fit parameters of the fitted curves depicted in figure 6.7. This was done by employing Newton's method [150] to determine the two half maxima of each peak and henceforth calculate its full width at half maximum (FWHM). The width was determined for the argument of the Lambert-Beer function, i.e. the pure Voigt profile. The results from the datasets measured at 2.3×10^{-2} mbar are depicted as red and blue points in figure 6.13. For better visibility data points belonging to the same total angular momentum J_X were shifted relative to each other. The colours of the depicted data points indicate this by alternating between different values of J_X. The gray shaded areas additionally group the data belonging to a single value of J_X . The errors were calculated from the fit errors by determining the maximum and minimum possible linewidth from them. For the dataset with $J_\mathrm{X} = 3.5$ the numeric determination of the errorbars failed for one of the two peaks, so that no reliable error could be determined. The corresponding dataset was therefore omitted. The three green datapoints were retrieved from the dataset depicted in figure 6.12. Here the evaluation failed for two of the three peaks, so that only the width of three of the five peaks could be determined with reliable error bars. To evaluate the width of that dataset the data was refitted without keeping the parameters for the peak positions fixed. As already discussed in section 6.4 this is the only dataset that was measured at 4.86×10^{-4} mbar and was later not reproducible. This should be kept in mind when interpreting figure 6.13.

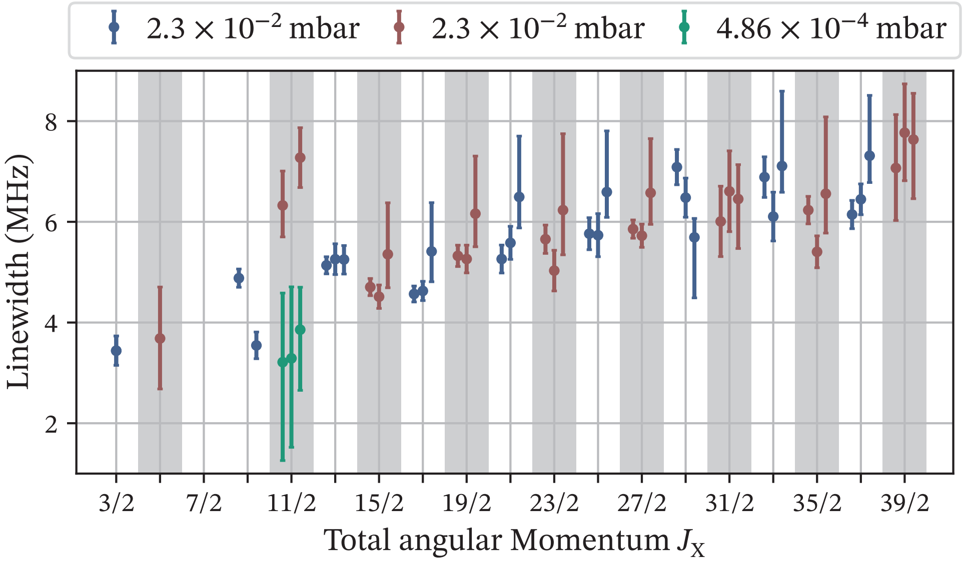

Figure 6.13: Linewidth (FWHM) determined from the fitted curves for the datasets discussed in section 6.3 and [1] in blue and red. Datapoints belonging to the same values of J_X are slightly offset to each other for better visibility. The alternating colours and shaded areas indicate data with the same value of J_X. The green datapoints were obtained from evaluation of the dataset discussed in section 6.4, which was measured at a significantly lower pressure.

The data in figure 6.13 indicates that the linewdith of the resolved lines increases slightly with increasing J_X. From this, one may interpret that those states have a larger natural linewidth. However, this behaviour may also be due to the beam adjustment. For larger J_X the intensity of the lines gets weaker. This was observed during the search for signals at the individual values of J_X and is also confirmed by the simulation conducted with PGOPHER. A weaker signal increases the difficulty of adjusting the beam overlap. For example, if the signal is so weak, that it is only clearly visible after averaging over a few single shot spectra, the response of the system to changes of the beam overlap is very difficult to notice for the experimenter. This can result in a less well adjusted beam overlap and therefore a larger linewidth.

It is remarkable that the linewidth of lines at low J_X is the lowest overall. Since one may expect that the individual peaks moving closer to each other would result in a larger linewidth due to the addition of the individual peaks. Comparison of the datasets for $J_X = 6.5$ and $J_X = 5.5$ shows this effect. The linewidths determined for $J_X = 5.5$ are larger than those for $J_X = 6.5$. That this does not occur for the lower values of J_X is difficult to explain, since it would mean that the individual hyperfine transitions have to be very narrow and very close to each other, so that they effectively hide beneath the linewidth of any additional broadening effects. Comparison to the calculation shows that this is rather unlikely. Thus the interpretation of the data for $J_X < 5.5$ seems to be contradictory too, in terms of the linewidth. To really obtain a better understanding of the data in this range of J_X additional measurements should be conducted. Ideally with a high resolution absolute frequency reference and better controlled beam overlap.

Comparison of the two datasets at $J_X = 5.5$ shows that the data measured at 4.86×10^{-4} mbar (green data points) yields a linewidth which is lower than that of the data measured at a higher pressure (red data points). This is a strong hint that the linewidth is mainly limited by collisional broadening, i.e. the cell pressure. However since the two datasets were measured at different dates the beam overlap may have been different here as well. It still remains unclear why the green dataset could not be reproduced at a later point. Thus, further investigations at low cell pressures and maybe also for different power parameters are necessary to unveil, what is exactly limiting the technique and how to interpret the additional two lines appearing in the spectrum.

The interpretation of the linewidth data yields contradictions and a lot of uncertainty. However, in general it still shows that the current resolution of this particular setup is at least somewhere between 4 MHz and 8 MHz. Additional measurements and an improved control of the spectroscopic parameters especially the beam overlap will be necessary to shrink the errorbars and obtain more reliable and comparable datasets.

6.6 Potential further investigations

In this chapter it has been shown that Doppler-free saturated absorption spectroscopy can be employed to quantitatively determine hyperfine constants of molecular energy levels and directly resolve Lamb-dips [1].

However, especially in section 6.4 and 6.5 the current limitations of the employed spectroscopic setup became clear. Therefore, further investigations need an improved setup. Especially the quantification of the beam overlap would help to compare different datasets with better reliability. For example, this could be achieved by measuring the pointing of each of the two beams with quadrant photodiodes after overlapping them as good as possible. If the overlap changes due to thermal fluctuations or a change in the pointing of the laser, one could use the initial measurement on the quadrant photodiodes to steer the beams back to their original positions. Instead of steering the beam by hand, motorised mirrors or piezo-mirrors could be employed. Furthermore, improvement of the initial beam quality of the UV-laser would allow to achieve a more precise overlap of the laser beams and to determine the spot sizes of the beam with higher accuracy.

Additional accuracy may also be gained by improving the frequency stabilisation setup for the UV-laser system. The measurements indicate that collisions are still the main limitation. To obtain a reasonable signal at even lower pressures the length of the spectroscopy cell should be increased or a multi-pass cell could be used.

With an improved spectroscopic setup and the beam overlap under better control, more precise measurements may be possible. Especially the search for crossover peaks may be easier at lower pressures. It may even be possible to resolve additional Lamb-dips at lower J_X. Finally, with this additional improvements investigations on the behaviour of the signal, especially the linewidth for different pressures and powers may yield information on the collisional processes occurring in the cell and may enable the accurate quantification of the saturation intensity for the different transitions. This is a valuable information for the improvement of the application of optogalvanic spectroscopy for gas sensing.

7 Conclusion and Outlook

In this work the first realisation of Doppler-free saturated absorption spectroscopy in nitric oxide was presented. This allowed the direct observation of Lamb-dips for nitric oxide. This has been realised recently for the hydrogen deuteride (HD) molecule too [151, 152]. In addition, it was possible to determine the hyperfine constants for the A $^2\Sigma^+$ state with slightly improved accuracy in comparison to previous measurements [1, 36]. In the case of nitric oxide the application of Doppler-free saturated absorption spectroscopy was basically enabled by the progress in laser technology. Without a narrowband continuous wave laser system the technique would not have been realisable. In principle, this technique is applicable to other molecules too. This might give insight into the hyperfine structure of other molecules in the future. However, one has to keep in mind that the intrinsic energy structure is not the same for all types of molecules.

In terms of the presented experiment, Doppler-free saturated absorption spectroscopy is not at its limit. Comparison of the datasets presented in section 6.4 and 6.3 shows that a decrease of the cell pressure led to an increase in resolution. A comprehensive measurement series for different pressures was not yet conducted but could yield information on the exact limitations by pressure broadening. However, for even smaller pressures the decrease in signal amplitude, may then require an even longer spectroscopy cell. In addition, to pressure broadening, power broadening may influence the spectroscopic lines. Here, further measurement series may yield information on how power broadening influences the signal and may finally enable the precise determination of the saturation intensity. The analysis of the spectra for lower values of J_X and the data presented in section 6.4 is not satisfying. Additional data may help to unveil what exactly causes the observed behaviour.

The suggested further measurements would all benefit from an improvement of the experimental parameters. Especially, enabling the quantification of the beam overlap, would allow a more reliable comparison of data concerning the amplitude and linewidth of the spectra. Further improvements could be made on the laser frequency stabilisation, to decrease the frequency uncertainty of the determined splittings. An increase in the overall long-term stability of the laser system would allow time consuming measurement series at the same parameters.

Concerning the development of the laboratory prototype for the application of optogalvanic spectroscopy to gas sensing, information about the structure of the involved molecular states, the saturation intensity and the effect of pressure broadening on the transition is valuable. The realisation of the Rydberg excitation of nitric oxide and its detection by optogalvanic spectroscopy is an important step forward to this project. However, the employed excitation scheme is most likely not the most efficient way to generate a large population in the Rydberg state. Thus, the optimisation of the excitation scheme is still to be done. In addition, improvements on the cell design, onboard cell electronics and detection scheme itself are subject to ongoing research. Electric field shielding and the employment of a lock-in amplifier in the optogalvanic detection process may improve the signal to noise ratio further. Eventually testing different concentrations of NO in N_2 and subsequently real breath gas samples may reveal new challenges. It can not be ruled out, that certain gases may have to be filtered out of real breath gas samples, before optogalvanic spectroscopy can be employed for determining the NO content.

In addition, the narrowband continuous wave excitation of nitric oxide Rydberg states opens up new experimental possibilities. Like the investigation of the behaviour of the corresponding Rydberg states in electric fields [81] or the search for ultralong-range Rydberg bimolecules in a thermal regime [153].

Danksagung

Meine Promotion und die vergangenen vier Jahr durchzustehen und erfolgreich abzuschließen, wäre ohne die Unterstützung zahlreicher Menschen nicht möglich gewesen. Diesen möchte ich hier meinen Dank aussprechen.

Zunächst gilt mein Dank Tilman Pfau, für die Möglichkeit an seinem Institut zu promovieren und das damit verbundene Vertrauen, sowie für die Unterstützung und die zahlreichen Kommentare, Hinweise, sowie Diskussionen im Laufe des Projekts. Die Zeit bei Dir, am 5. Physikalischen Institut, war eine hervorragende Schule, bei der ich in den unterschiedlichsten Bereichen viel dazulernen konnte. Vielen Dank dafür!

Ich danke außerdem Herrn Professor Peter Michler, dass er so freundlich war, den Mitbericht für diese Arbeit zu übernehmen und Herrn Professor Hans-Peter Büchler für die Übernahme des Prüfungsvorsitzes.

Des Weiteren danke ich Harald Kübler für die freundschaftliche Zusammenarbeit und dafür, dass er immer, wenn mir die Ideen ausgingen, doch noch einen Einfall hatte, den es auszuprobieren lohnte.

Robert Löw danke ich für clevere Anmerkungen und Erklärungen und für die geschickte Vertretung unseres Projekts gegenüber unseren Geldgebern.

Für das Korrekturlesen dieser Arbeit danke ich Fabian Munkes, Harald Kübler, Matthias Schmidt, Annika Belz und Max Mäusezahl. Eure Anmerkungen waren stets hilfreich, durchdacht und von konstruktiver Natur.

Ein Projekt wie dieses, das für mich vor knapp über vier Jahren mit einem leeren Labor begann, ist nicht möglich ohne zahlreiche Studentinnen und Studenten, die im Rahmen ihrer Arbeiten am Aufbau des Experiments beteiligt waren. Hier möchte ich ganz besonders die Arbeit von Yannick Schellander und Philipp Neufeld hervorheben, die durch ihre hervorragenden Beiträge im Labor und in der Theorie dieses Projekt vorangetrieben haben und uns glücklicherweise als Doktoranden erhalten geblieben sind. Des Weiteren danke ich Lea Ebel, Malte Kasten, Luana Rubino, Joshua Fabian, André Bisquerra, Pascal Pruy und Michael Ilewicz für ihre Beiträge zu unserem Experiment.

Von meinen Kollegen möchte ich allen voran Fabian Munkes danken. Seine Beiträge zum Aufbau unseres Experiments begannen bereits mit seiner Masterarbeit und gingen schon damals über das übliche Maß hinaus. Ohne ihn wären viele hervorragende Systeme, wie unsere Lock- und Steuerungsssoftware oder die durchdachte Messautomatisierung in dieser Form nicht existent. Es war für uns beide eine Leidenszeit, mit sieben Pumplasern in drei Jahren und einem Defekt nach dem anderen. Ich bin froh, hierbei nicht allein gewesen zu sein und danke Dir, für all die gemeinsame Zeit, die Unterstützung, gute Zusammenarbeit und auch für die vielen persönlichen Gespräche, die wir geführt haben. Ich wünsche Dir nichts mehr, als dass Du deine eigene Promotion nun schnell abschließen kannst und dabei vom Fehlerteufel in Frieden gelassen wirst!

Des Weiteren danke ich Artur Skljarow für zahlreiche Gespräche und Diskussionen in unseren gemeinsamen Mittagspausen, sowie dem ganzen ”3rd Floor-Team”für die schöne Zeit mit Euch.

Es bleibt noch die Unterstützung von unserem Glasbläser Frank Schreiber und Marc Oliver Schmid vom Institut für Feuerungs- und Kraftwerkstechnik zu erwähnen, die durch ihre technischen Fertigkeiten die Produktion und Befüllung zahlreicher verschiedener Spektroskopiezellen ermöglicht haben. Des Weiteren wäre eine sichere Lagerung unseres Stickstoffmonoxids ohne Franks unkomplizierte Unterstützung nicht möglich.

Weiterer Dank gilt dem Verwaltungsteam des 5. Physikalischen Instituts. Allen voran danke ich hier Anne-Katrin Kriesch für ihre umfangreiche Unterstützung bei zahlreichen Verwaltungsaufgaben wie zum Beispiel den besonders spaßigen EU-Timesheets, sowie Karin Otter und Astrid Buck.

Weiterhin gilt besonderer Dank meinen Freunden für ihre Unterstützung und dass sie mir hin und wieder gezeigt haben, dass es auch sinnvoll ist, mal eine Pause einzulegen.

Ganz besonders danke ich meinen lieben Eltern. Ohne Euch wäre mein Studium so nicht möglich gewesen und damit auch meine Promotion ausgeschlossen gewesen. Danke, dass Ihr mir immer die Freiheit gelassen habt, selbst und unbeeinflusst zu entscheiden, welchen Weg ich gehen möchte, und mich im Anschluss, egal wie dieser Weg ausgesehen hat, dabei unterstützt habt. Man konnte sich immer uneingeschränkt auf Euren Rat und Eure Hilfe verlassen.

Zu guter Letzt bleibt noch ein ganz besonderer Mensch, dem ich danken muss, meiner Freundin Cornelia Vogel. Ohne Dich wäre diese Promotion vermutlich nicht erfolgreich zu Ende gegangen. Ich bin immer noch davon überzeugt, dass Du über viele Phasen meiner Promotion hinweg mehr davon überzeugt warst, dass das trotz all der Schwierigkeiten doch noch werden wird, als ich selbst. Du hast Dir all die Sorgen und Probleme angehört, meine Selbstzweifel weggewischt, es einfach hingenommen, dass oft auch unsere gemeinsame Zeit oder gemeinsamer Urlaub hinter der Arbeit im Labor zurückstehen musste. Für all das, ja für deine immerwährende Unterstützung, kann ich Dir nicht genug danken!

Bibliography

[1] P. Kaspar et al. *Doppler-free high resolution continuous wave optical UV-spectroscopy on the* $\mathrm{A}\,^2\Sigma^+ \leftarrow \mathrm{X}\,^2\Pi_{3/2}$ *transition in nitric oxide*. Under Review at Physical Review A. 2022. DOI: 10.48550/ARXIV.2206.15243 (cit. on pp. V, 3, 99, 100, 102, 119, 121, 122, 128, 130, 131).

[2] R. Daschner et al. “Fabrication and characterization of an electrically contacted vapor cell”. In: *Opt. Lett.* 37.12 (June 2012), pp. 2271–2273. DOI: 10.1364/OL.37.002271. URL: http://opg.optica.org/ol/abstract.cfm?URI=ol-37-12-2271 (cit. on p. 1).

[3] R. Daschner et al. “Triple stack glass-to-glass anodic bonding for optogalvanic spectroscopy cells with electrical feedthroughs”. In: *Applied Physics Letters* 105.4 (2014), p. 041107. DOI: 10.1063/1.4891534. eprint: https://doi.org/10.1063/1.4891534. URL: https://doi.org/10.1063/1.4891534 (cit. on p. 1).

[4] D. Barredo et al. “Electrical Readout for Coherent Phenomena Involving Rydberg Atoms in Thermal Vapor Cells”. In: *Phys. Rev. Lett.* 110 (12 Mar. 2013), p. 123002. DOI: 10.1103/PhysRevLett.110.123002. URL: https://link.aps.org/doi/10.1103/PhysRevLett.110.123002 (cit. on p. 1).

[5] R. Daschner. “Adressable Rubidium vapor cells for optical and electrical read-out of Rydberg excitations”. PhD thesis. Universität Stuttgart, Apr. 2015. URL: https://www.pi5.uni-stuttgart.de/documents/abgeschlossene-arbeiten/2015-Daschner-Renate-Addressable-Rubidium-vapor-cells-for-optical-and-electrical-read-out-of-Rydberg-excitations-PhD.pdf (cit. on p. 1).

[6] J. Schmidt et al. “An optogalvanic gas sensor based on Rydberg excitations”. In: *Journal of Physics B: Atomic, Molecular and Optical Physics* 53.9 (Mar. 2020), p. 094001. DOI: 10.1088/1361-6455/ab728e. URL: https://doi.org/10.1088/1361-6455/ab728e (cit. on pp. 1, 46, 91).

[7] F. Munkes. “Continuous-wave absorption spectroscopy on the $X^2\,\Pi_{1/2}$ to $A\,\Sigma^+$ transition of nitric oxide”. MA thesis. Universität Stuttgart, Oct. 2019 (cit. on pp. 1, 48, 57).

[8] P. Kaspar et al. “Towards an Optogalvanic Flux Sensor for Nitric Oxide Based on Rydberg Excitation”. In: *OSA Optical Sensors and Sensing Congress 2021 (AIS, FTS, HISE, SENSORS, ES)*. Optica Publishing Group, 2021, STu4G.3. DOI: 10.1364/SENSORS.2021.STu4G.3. URL: http://opg.optica.org/abstract.cfm?URI=Sensors-2021-STu4G.3 (cit. on pp. 1, 3, 46, 91).

[9] J. Schmidt et al. “Proof of concept for an optogalvanic gas sensor for NO based on Rydberg excitations”. In: *Applied Physics Letters* 113.1 (2018), p. 01 1113. DOI: 10.1063/1.5024321. URL: https://doi.org/10.1063/1.5024321 (cit. on pp. 1, 46, 69, 83, 91).

[10] J. Schmidt. “A trace gas sensor based on Rydberg excitations - A proof of concept study”. PhD thesis. Universität Stuttgart, 2019 (cit. on pp. 1, 46, 97).

[11] Press Release. Retrieved 4th October 2022. URL: https://www.nobelprize.org/prizes/medicine/1998/press-release/ (cit. on p. 2).

[12] R. F. Furchgott and J. V. Zawadzki. “The obligatory role of endothelial cells in the relaxation of arterial smooth muscle by acetylcholine”. In: *Nature* 288.5789 (Nov. 1980), pp. 373–376. DOI: 10.1038/288373a0 (cit. on p. 2).

[13] L. J. Ignarro et al. “Endothelium-derived relaxing factor produced and released from artery and vein is nitric oxide.” In: *Proceedings of the National Academy of Sciences* 84.24 (Dec. 1987), pp. 9265–9269. DOI: 10.1073/pnas.84.24.9265 (cit. on p. 2).

[14] S. Moncada and E. A. Higgs. “The discovery of nitric oxide and its role in vascular biology”. In: *British Journal of Pharmacology* 147.S1 (2006), S193–S201. DOI: https://doi.org/10.1038/sj.bjp.0706458. eprint: https://bpspubs.onlinelibrary.wiley.com/doi/pdf/10.1038/sj.bjp.0706458. URL: https:

//bpspubs.onlinelibrary.wiley.com/doi/abs/10.1038/sj.bjp.0706458 (cit. on p. 2).

[15] S. R. Jaffrey and S. H. Snyder. “Nitric Oxide: A Neural Messenger”. In: *Annual Review of Cell and Developmental Biology* 11.1 (Nov. 1995), pp. 417–440. DOI: 10.1146/annurev.cb.11.110195.002221 (cit. on p. 2).

[16] E. M. Palmieri et al. “Nitric Oxide in Macrophage Immunometabolism: Hiding in Plain Sight”. In: *Metabolites* 10.11 (Oct. 2020), p. 429. DOI: 10.3390/metabo10110429 (cit. on p. 2).

[17] J. Lundberg et al. “Elevated nitric oxide in the urinary bladder in infectious and noninfectious cystitis”. In: *Urology* 48.5 (Nov. 1996), pp. 700–702. DOI: 10.1016/s0090-4295(96)00423-2 (cit. on p. 2).

[18] S. T. Connelly et al. “Increased nitric oxide levels and iNOS over-expression in oral squamous cell carcinoma”. In: *Oral Oncology* 41.3 (2005), pp. 261–267. ISSN: 1368-8375. DOI: https://doi.org/10.1016/j.oraloncology.2004.09.007. URL: https://www.sciencedirect.com/science/article/pii/S1368837504002209 (cit. on p. 2).

[19] L. J. M. Alving K. Weitzberg E. “Increased amount of nitric oxide in exhaled air of asthmatics”. In: *Eur Respir J* (1993). eprint: https://erj.ersjournals.com/content/6/9/1368.full.pdf. URL: https://erj.ersjournals.com/content/6/9/1368 (cit. on p. 2).

[20] A. Mazzatenta, C. Di Giulio, and M. Pokorski. “Pathologies currently identified by exhaled biomarkers”. In: *Respiratory Physiology & Neurobiology* 187.1 (2013). Immunopathology of the Respiratory System, pp. 128–134. ISSN: 1569-9048. DOI: https://doi.org/10.1016/j.resp.2013.02.016. URL: https://www.sciencedirect.com/science/article/pii/S1569904813000475 (cit. on p. 2).

[21] J. O. Lundberg and E. Weitzberg. “Nitric oxide signaling in health and disease”. In: *Cell* 185.16 (2022), pp. 2853–2878. ISSN: 0092-8674. DOI: https://doi.org/10.1016/j.cell.2022.06.010. URL: https://www.sciencedirect.com/science/article/pii/S0092867422007152 (cit. on p. 2).

[22] R. T. Hall and J. M. Dowling. “Pure Rotational Spectrum of Nitric Oxide”. In: *The Journal of Chemical Physics* 45.6 (Sept. 1966), pp. 1899–1903. DOI: 10.1063/1.1727868 (cit. on p. 2).

[23] R. Engleman et al. *BETA AND GAMMA BAND SYSTEMS OF NITRIC OXIDE.* Tech. rep. Jan. 1969. DOI: 10.2172/4128104 (cit. on p. 2).

[24] T. Tajime, T. Saheki, and K. Ito. “Absorption characteristics of the γ-0 bandof nitric oxide”. In: *Appl. Opt.* 17.8 (Apr. 1978), pp. 1290–1294. DOI: 10.1364/AO.17.001290. URL: http://opg.optica.org/ao/abstract.cfm?URI=ao-17-8-1290 (cit. on p. 2).

[25] J. Ishii et al. “Observation of the A 2Σ+ ← X 2Π32 transition of nitric oxide with two-photon degenerate four-wave mixing”. In: *Chemical Physics Letters* 220.1 (1994), pp. 29–34. ISSN: 0009-2614. DOI: https://doi.org/10.1016/0009-2614(94)00130-8. URL: https://www.sciencedirect.com/science/article/pii/0009261494001308 (cit. on p. 2).

[26] A. V. Zobnin and A. N. Korotkov. “Absorption spectrum of NO in the gamma (O, O) band”. In: *Journal of Applied Spectroscopy* 61.5-6 (May 1995). URL: https://www.osti.gov/biblio/161866 (cit. on p. 2).

[27] D. X. Wang, C. Haridass, and S. Reddy. “The Gamma (A2Σ+–X2Πr) System of the Nitric Oxide Isotopomers”. In: *Journal of Molecular Spectroscopy* 175.1 (1996), pp. 73–84. ISSN: 0022-2852. DOI: https://doi.org/10.1006/jmsp.1996.0011. URL: https://www.sciencedirect.com/science/article/pii/S0022285296900119 (cit. on pp. 2, 15, 35, 39).

[28] J. Danielak et al. “Reinvestigation of the Emission γ-Band System ($A^2\Sigma^+$–$X^2\Pi$) of the NO Molecule”. In: *Journal of Molecular Spectroscopy* 181.2 (1997), pp. 394–402. ISSN: 0022-2852. DOI: https://doi.org/10.1006/jmsp.1996.7181. URL: https://www.sciencedirect.com/science/article/pii/S0022285296971817 (cit. on pp. 2, 157, 159, 161).

[29] P. G. Favero, A. M. Mirri, and W. Gordy. “Millimeter-Wave Rotational Spectrum of NO in the $^2\pi_{\frac{3}{2}}$ State”. In: *Phys. Rev.* 114 (6 June 1959), pp. 1534–1537. DOI: 10.1103/PhysRev.114.1534. URL: https://link.aps.org/doi/10.1103/PhysRev.114.1534 (cit. on pp. 2, 99).

[30] T. Bergeman and R. N. Zare. *Fine structure, hyperfine structure, and Stark effect in the NO A 2Σ+ state by optical radio-frequency double resonance*. Vol. 61. 11. 1974, pp. 4500–4514. DOI: 10.1063/1.1681767. eprint: https://doi.org/10.1063/1.1681767. URL: https://doi.org/10.1063/1.1681767 (cit. on pp. 2, 99).

[31] K. L. Reid, S. P. Duxon, and M. Towrie. “Observation of time- and angle-resolved photoelectron flux from an optically prepared state of a molecule. Hyperfine depolarization in NO (A 2Σ+)”. In: *Chemical Physics Letters* 228.4 (1994), pp. 351–356. ISSN: 0009-2614. DOI: https://doi.org/10.1016/0009-2614(94)00963-5. URL: https://www.sciencedirect.com/science/article/pii/0009261494009635 (cit. on pp. 2, 99).

[32] E. McCormack et al. “Observation of hyperfine quantum beats in two-color laser-induced grating spectroscopy of nitric oxide”. In: *Chemical Physics Letters* 227.6 (1994), pp. 656–662. ISSN: 0009-2614. DOI: https://doi.org/10.1016/0009-2614(94)00875-2. URL: https://www.sciencedirect.com/science/article/pii/0009261494008752 (cit. on pp. 2, 99).

[33] S. Saupe et al. “Sub-Doppler Heterodyne Frequency Measurements and Calibration Tables for the Nitric Oxide Fundamental Band”. In: *Journal of Molecular Spectroscopy* 179.1 (1996), pp. 13–21. ISSN: 0022-2852. DOI: https://doi.org/10.1006/jmsp.1996.0179. URL: https://www.sciencedirect.com/science/article/pii/S0022285296901794 (cit. on pp. 2, 99).

[34] E. F. McCormack and E. Sarajlic. “Polarization effects in quantum coherences probed by two-color, resonant four-wave mixing in the time domain”. In: *Phys. Rev. A* 63 (2 Jan. 2001), p. 023406. DOI: 10.1103/PhysRevA.63.023406. URL: https://link.aps.org/doi/10.1103/PhysRevA.63.023406 (cit. on pp. 2, 99).

[35] T. D. Varberg, F. Stroh, and K. M. Evenson. “Far-Infrared Rotational and Fine-Structure Transition Frequencies and Molecular Constants of 14NO and 15NO in the X2Π (v = 0) State”. In: *Journal of Molecular Spectroscopy* 196.1 (1999), pp. 5–13. ISSN: 0022-2852. DOI: https://doi.org/10.1006/jmsp.1999.7850. URL: https://www.sciencedirect.com/science/article/pii/S0022285299978505 (cit. on pp. 2, 14, 35, 37, 99, 119, 159, 160).

[36] M. Brouard et al. “The hyperfine structure of NO(A2Σ+)”. In: *Journal of Molecular Spectroscopy* 282 (2012), pp. 42–49. ISSN: 0022-2852. DOI: https://doi.org/10.1016/j.jms.2012.11.003. URL: https://www.sciencedirect.com/science/article/pii/S0022285212002172 (cit. on pp. 2, 29, 99, 119, 121, 131, 161).

[37] C. J. Foot. *Atomic Physics*. 1st ed. Great Clarendon Street, Oxford OX2 6DP: Oxford University Press, 2005. ISBN: 0198506951 (cit. on pp. 5, 14, 31, 47–49, 51–53).

[38] G. Herzberg. *Spectra of Diatomic Molecules*. 2nd ed. Vol. 1. Molecular Spectra and Molecular Structure. D. Van Nostrand Company Inc., 1950 (cit. on pp. 6, 8, 9, 11–14, 16, 21, 22, 25, 116).

[39] M. Born and R. Oppenheimer. “Zur Quantentheorie der Molekeln”. In: *Annalen der Physik* 389.20 (1927), pp. 457–484. DOI: https://doi.org/10.1002/andp.19273892002. eprint: https://onlinelibrary.wiley.com/doi/pdf/10.1002/andp.19273892002. URL: https://onlinelibrary.wiley.com/doi/abs/10.1002/andp.19273892002 (cit. on p. 7).

[40] H. Haken and H. C. Wolf. *Molekülphysik und Quantenchemie*. 4th ed. Springer-Verlag, 2006. ISBN: 13 9783540303145 (cit. on pp. 7–9, 157).

[41] L. Hvozdara et al. “Quantum cascade lasers for mid-infrared spectroscopy”. In: *Vibrational Spectroscopy* 30.1 (2002). Papers Presented at the 1st International Conference on Advanced Vibrational Spectroscopy, Turku, Finland, August 19-24, 2001, pp. 53–58. ISSN: 0924-2031. DOI: https://doi.org/10.1016/S0924-2031(02)00038-3. URL: https://www.sciencedirect.com/science/article/pii/S0924203102000383 (cit. on p. 7).

[42] F. A. Jenkins, H. A. Barton, and R. S. Mulliken. “The Beta Bands of Nitric Oxide. I. Measurements and Quantum Analysis”. In: *Phys. Rev.* 30 (2 Aug. 1927), pp. 150–174. DOI: 10.1103/PhysRev.30.150. URL: https://link.aps.org/doi/10.1103/PhysRev.30.150 (cit. on p. 8).

[43] R. H. Gillette and E. H. Eyster. “The Fundamental Rotation-Vibration Band of Nitric Oxide”. In: *Phys. Rev.* 56 (11 Dec. 1939), pp. 1113–1119. DOI: 10.1103/PhysRev.56.1113. URL: https://link.aps.org/doi/10.1103/PhysRev.56.1113 (cit. on p. 8).

[44] C. C. LIN and J. D. SWALEN. “Internal Rotation and Microwave Spectroscopy”. In: *Rev. Mod. Phys.* 31 (4 Oct. 1959), pp. 841–892. DOI: 10.1103/RevModPhys.31.841. URL: https://link.aps.org/doi/10.1103/RevModPhys.31.841 (cit. on p. 9).

[45] J. M. Brown and A. Carrington. *Rotational Spectroscopy of Diatomic Molecules*. Ed. by R. J. Saykally, A. H. Zewail, and D. A. King. 1st ed. Cambridge University Press, 2003. ISBN: 978-0-511-07266-6 6 (cit. on pp. 9, 11, 12, 15–20, 24, 26–28, 30, 34, 160).

[46] F. Reiche. “Die Quantelung des symmetrischen Kreisels nach Schrödinger Undulationsmechanik”. In: *Zeitschrift für Physik* 39.5 (Aug. 1926), pp. 444–464. DOI: https://doi.org/10.1007/BF01322053 (cit. on p. 11).

[47] R. d. L. Kronig and I. I. Rabi. “The Symmetrical Top in the Undulatory Mechanics”. In: *Phys. Rev.* 29 (2 Feb. 1927), pp. 262–269. DOI: 10.1103/PhysRev.29.262. URL: https://link.aps.org/doi/10.1103/PhysRev.29.262 (cit. on p. 11).

[48] H. Rademacher and F. Reiche. “Die Quantelung des symmetrischen Kreisels nach Schrödingers Undulationsmechanik”. In: *Zeitschrift für Physik A Hadrons and nuclei* 41.6 (1927), pp. 453–492. DOI: https://doi.org/10.1007/BF01400207 (cit. on p. 11).

[49] J. L. Dunham. “The Energy Levels of a Rotating Vibrator”. In: *Phys. Rev.* 41 (6 Sept. 1932), pp. 721–731. DOI: 10.1103/PhysRev.41.721. URL: https://link.aps.org/doi/10.1103/PhysRev.41.721 (cit. on p. 12).

[50] C. L. Pekeris. “The Rotation-Vibration Coupling in Diatomic Molecules”. In: *Phys. Rev.* 45 (2 Jan. 1934), pp. 98–103. DOI: 10.1103/PhysRev.45.98. URL: https://link.aps.org/doi/10.1103/PhysRev.45.98 (cit. on p. 12).

[51] S. N. Dixit et al. “Rotational branching ratios in (1+1) resonant-enhanced multiphoton ionization of NO via the $A^2\Sigma^+$ state”. In: *Phys. Rev. A* 32 (2 Aug. 1985), pp. 1267–1270. DOI: 10.1103/PhysRevA.32.1267. URL: https://link.aps.org/doi/10.1103/PhysRevA.32.1267 (cit. on pp. 15, 35).

[52] J. Brown et al. “The labeling of parity doublet levels in linear molecules”. In: *Journal of Molecular Spectroscopy* 55.1 (1975), pp. 500–503. ISSN: 0022-2852. DOI: https://doi.org/10.1016/0022-2852(75)90291-X. URL: https://www.sciencedirect.com/science/article/pii/002228527590291X (cit. on pp. 21, 23).

[53] W. Nolting. *Grundkurs Theoretische Physik 5/2 Quantenmechanik - Methoden und Anwendungen. Quantenmechanik - Methoden und Anwendungen*. Springer Spektrum, 2015, p. 647. ISBN: 9783662442296 (cit. on p. 23).

[54] F. Kogel. “Modeling laser cooling of diatomic molecules”. MA thesis. Universität Stuttgart, June 2021 (cit. on pp. 24, 26, 29).

[55] J. Brown and A. Merer. “Lambda-type doubling parameters for molecules in Π electronic states of triplet and higher multiplicity”. In: *Journal of Molecular Spectroscopy* 74.3 (1979), pp. 488–494. ISSN: 0022-2852. DOI: https://doi.org/10.1016/0022-2852(79)90172-3. URL: https://www.sciencedirect.com/science/article/pii/0022285279901723 (cit. on p. 25).

[56] T. F. Gallagher. *Rydberg atoms*. Cambridge University Press, 1994, p. 495. ISBN: 0521385318 (cit. on p. 31).

[57] M. J. Seaton. “Quantum defect theory”. In: *Reports on Progress in Physics* 46.2 (Feb. 1983), pp. 167–257. DOI: 10.1088/0034-4885/46/2/002. URL: https://iopscience.iop.org/article/10.1088/0034-4885/46/2/002 (cit. on p. 31).

[58] G. Herzberg. “Rydberg Molecules”. In: *Annual Review of Physical Chemistry* 38.1 (1987). PMID: 18393686, pp. 27–56. DOI: 10.1146/annurev.pc.38.100187.000331. eprint: https://doi.org/10.1146/annurev.pc.38.100187.000331. URL: https://doi.org/10.1146/annurev.pc.38.100187.000331 (cit. on p. 31).

[59] M. A. Baig et al. “Rydberg transitions in the H_2S molecule”. In: *Journal of Physics B: Atomic and Molecular Physics* 14.22 (Nov. 1981), pp. L725–L730. DOI: 10.1088/0022-3700/14/22/002. URL: https://doi.org/10.1088/0022-3700/14/22/002 (cit. on p. 31).

[60] H. Wang, W. S. Felps, and S. P. McGlynn. "Molecular Rydberg states. VII. Water". In: *The Journal of Chemical Physics* 67.6 (1977), pp. 2614–2628. DOI: 10.1063/1.435173. eprint: https://aip.scitation.org/doi/pdf/10.1063/1.435173. URL: https://aip.scitation.org/doi/abs/10.1063/1.435173 (cit. on p. 31).

[61] S. R. Langford et al. "The spectroscopy of high Rydberg states of ammonia". In: *The Journal of Chemical Physics* 108.16 (1998), pp. 6667–6680. DOI: 10.1063/1.476082. eprint: https://doi.org/10.1063/1.476082. URL: https://doi.org/10.1063/1.476082 (cit. on p. 31).

[62] U. Even, M. Ben-Nun, and R. Levine. "Time evolution of very high Rydberg states of large aromatic molecules. A kinetic analysis". In: *Chemical Physics Letters* 210.4 (1993), pp. 416–422. ISSN: 0009-2614. DOI: https://doi.org/10.1016/0009-2614(93)87047-7. URL: https://www.sciencedirect.com/science/article/pii/0009261493870477 (cit. on p. 31).

[63] R. GREENBAUM et al. "EFFECTS OF HIGHER OXIDES OF NITROGEN ON THE ANAESTHETIZED DOG". In: *British Journal of Anaesthesia* 39.5 (1967), pp. 393–404. ISSN: 0007-0912. DOI: https://doi.org/10.1093/bja/39.5.393. URL: https://www.sciencedirect.com/science/article/pii/S0007091217519509 (cit. on p. 33).

[64] E. Miescher and K. P. Huber. In: *Spectroscopy*. Ed. by A. D. Buckingham and D. A. Ramsay. Vol. 3. International Review of Science: Physical Chemistry Series Two. Butterworth & Co Ltd, 1976. Chap. Electronic Spectrum of the NO molecule. ISBN: 0-40870-602-3 (cit. on p. 34).

[65] P. De Biévre and P. Taylor. "Table of the isotopic compositions of the elements". In: *International Journal of Mass Spectrometry and Ion Processes* 123.2 (1993), pp. 149–166. ISSN: 0168-1176. DOI: https://doi.org/10.1016/0168-1176(93)87009-H. URL: https://www.sciencedirect.com/science/article/pii/016811769387009H (cit. on p. 34).

[66] W. M. Haynes. *CRC Handbook of Chemistry and Physics, 95th Edition*. Taylor & Francis Group, 2014, p. 2704. ISBN: 9781482208689 (cit. on pp. 34, 48, 72, 164).

[67] A. Liu. “Electron Paramagnetic Resonance (EPR) in Enzymology”. In: *Wiley Encyclopedia of Chemical Biology*. John Wiley & Sons, Ltd, 2008, pp. 1–36. ISBN: 9780470048672. DOI: https://doi.org/10.1002/9780470048672.wecb668. eprint: https://onlinelibrary.wiley.com/doi/pdf/10.1002/9780470048672.wecb668. URL: https://onlinelibrary.wiley.com/doi/abs/10.1002/9780470048672.wecb668 (cit. on p. 34).

[68] S. Mollet. “Rydberg states and photoionisaion dynamics of NO and Cl_2”. PhD thesis. Eidgenössisch Technische Hochschule Zürich, 2013 (cit. on pp. 34, 38, 40–42, 91, 94).

[69] K. Dressler and E. Miescher. “Absorption Spectrum of the NO Molecule. V. Survey of Excited States and Their Interactions”. In: *Astrophys. J.* 141 (1965), pp. 1266–1283. URL: https://articles.adsabs.harvard.edu/full/1965ApJ...141.1266D (cit. on p. 34).

[70] R. A. Young and R. L. Sharpless. “Excitation of the β, γ, δ, and Ogawa bands of nitric oxide in the association of atomic nitrogen and oxygen”. In: *Discuss. Faraday Soc.* 33 (0 1962), pp. 228–256. DOI: 10.1039/DF9623300228. URL: http://dx.doi.org/10.1039/DF9623300228 (cit. on p. 34).

[71] Y. Schellander. “Ionization current measurements of Ryberg states in nitric oxide created by continous-wave three-photon excitation”. MA thesis. Universität Stuttgart, 2020 (cit. on pp. 34, 46, 91, 95, 97).

[72] K. Kaufmann, C. Nager, and M. Jungen. “Rydberg states and quantum defects of the NO molecule”. In: *Chemical Physics* 95.3 (1985), pp. 385–390. ISSN: 0301-0104. DOI: https://doi.org/10.1016/0301-0104(85)80161-0. URL: https://www.sciencedirect.com/science/article/pii/0301010485801610 (cit. on p. 35).

[73] K. Huber, M. Huber, and E. Miescher. “Rydberg-series of the no-molecule in the visible and infrared emission spectrum”. In: *Physics Letters* 3.7 (1963), pp. 315–316. ISSN: 0031-9163. DOI: https://doi.org/10.1016/0031-9163(63)90171-9 (cit. on p. 35).

[74] E. Grant. *Private Communication*. 2018 (cit. on p. 35).

[75] E. KLISCH et al. “Transitions between Hund’s coupling cases for the X 2Π state of NO”. In: *Molecular Physics* 97.1-2 (1999), pp. 65–79. DOI: 10.1080/00268979909482810. eprint: https://doi.org/10.1080/00268979909482810. URL: https://doi.org/10.1080/00268979909482810 (cit. on pp. 35, 41).

[76] Y. Ogi et al. “Laser-induced amplified spontaneous emission from the 3d and nf Rydberg states of NO”. In: *Chemical Physics* 255.2 (2000), pp. 379–395. ISSN: 0301-0104. DOI: https://doi.org/10.1016/S0301-0104(00)00043-4. URL: https://www.sciencedirect.com/science/article/pii/S0301010400000434 (cit. on pp. 38, 94).

[77] A. Bernard et al. “On the 3d Rydberg states of the NO molecule”. In: *Molecular Physics* 73.1 (1991), pp. 221–234. DOI: 10.1080/00268979100101161. eprint: https://doi.org/10.1080/00268979100101161. URL: https://doi.org/10.1080/00268979100101161 (cit. on pp. 38, 41, 42, 162, 163).

[78] K. Huber and E. Miescher. “Absorption spectrum of the NO molecule”. In: *Helvetica Physica Acta* 36.3 (1963), pp. 257–268. URL: https://www.e-periodica.ch/digbib/view?pid=hpa-001:1963:36::261#261 (cit. on pp. 41–43).

[79] K. I. “On the $H\,^2\Sigma^+$ - $H'\,\Pi^2$ perturbation of the NO-molecule”. In: *Helvetica Physica Acta* 36.VI (1963), pp. 699–706. URL: https://www.e-periodica.ch/digbib/volumes?UID=hpa-001 (cit. on p. 41).

[80] A. Bernard et al. “The 5d states of barium hydride; BaH and BaD”. In: *Molecular Physics* 67.1 (1989), pp. 1–18. DOI: 10.1080/00268978900100891. eprint: https://doi.org/10.1080/00268978900100891. URL: https://doi.org/10.1080/00268978900100891 (cit. on p. 41).

[81] P. Neufeld. “Collisional ionization of Rydberg states in nitric oxide”. MA thesis. Universität Stuttgart, 2022 (cit. on pp. 44, 98, 132).

[82] J. Fabian. *Design einer elektrisch kontaktierten Durchflusszelle zur Detektion von Ionisierungsströmen von Rydbergzuständen Stickstoffmonoxids*. Bachelor Thesis. Sept. 2020 (cit. on pp. 44, 93).

[83] J. Schmidt et al. “A transimpedance amplifier based on an LTPS process operated in alkali vapor for the measurement of an ionization current”. In: *Quantum Technologies 2018*. Ed. by J. Stuhler, A. J. Shields, and M. J. Padgett. Vol. 10674. International Society for Optics and Photonics. SPIE, 2018, pp. 50–57. DOI: 10.1117/12.2309655. URL: https://doi.org/10.1117/12.2309655 (cit. on pp. 46, 97).

[84] A. Castrillo et al. “Doppler-free saturated-absorption spectroscopy of CO2 at 4.3 μm by means of a distributed feedback quantum cascade laser”. In: *Opt. Lett.* 31.20 (Oct. 2006), pp. 3040–3042. DOI: 10.1364/OL.31.003040. URL: http://opg.optica.org/ol/abstract.cfm?URI=ol-31-20-3040 (cit. on p. 51).

[85] S. Svanberg et al. “High-contrast Doppler-free transmission spectroscopy”. In: *Opt. Lett.* 11.3 (Mar. 1986), pp. 138–140. DOI: 10.1364/OL.11.000138. URL: http://opg.optica.org/ol/abstract.cfm?URI=ol-11-3-138 (cit. on p. 51).

[86] K.-m. Chen et al. “Doppler-free two-photon absorption spectroscopy of naphthalene”. In: *Optics Communications* 23.1 (1977), pp. 90–94. ISSN: 0030-4018. DOI: https://doi.org/10.1016/0030-4018(77)90133-X. URL: https://www.sciencedirect.com/science/article/pii/003040187790133X (cit. on p. 51).

[87] J. Bowie, J. Boyce, and R. Chiao. “Saturated-absorption spectroscopy of weak-field Zeeman splittings in rubidium”. In: *J. Opt. Soc. Am. B* 12.10 (Oct. 1995), pp. 1839–1842. DOI: 10.1364/JOSAB.12.001839. URL: http://opg.optica.org/josab/abstract.cfm?URI=josab-12-10-1839 (cit. on p. 51).

[88] W. Demtröder. *Experimentalphysik 3*. Springer-Verlag GmbH, June 2016. ISBN: 978-3-662-49094-5. URL: https://www.ebook.de/de/product/27952543/wolfgang_demtroeder_experimentalphysik_3.html (cit. on p. 52).

[89] W. Demtröder. *Laserspektroskopie 1*. Springer-Verlag GmbH, Sept. 2011. ISBN: 9783642213069. URL: https://www.ebook.de/de/product/16844064/wolfgang_demtroeder_laserspektroskopie_1.html (cit. on p. 52).

[90] J. A. Myers, I. Irving, and K. E. “Dye Lasers in the Ultraviolet”. In: *Nature* 225.5232 (1970), pp. 544–545. DOI: https://doi.org/10.1038/225544a0 (cit. on p. 56).

[91] G. A. Abakumov et al. “Generation of ultraviolet radiation tunable in the 216–226 nm range”. In: *Soviet Journal of Quantum Electronics* 4.11 (1975), pp. 1404–1405. DOI: 10.1070/qe1975v004n11abeh011979. URL: https://doi.org/10.1070/qe1975v004n11abeh011979 (cit. on p. 56).

[92] J. P. Morrison, C. J. Rennick, and E. R. Grant. “Very slow expansion of an ultracold plasma formed in a seeded supersonic molecular beam of NO”. In: *Phys. Rev. A* 79 (6 June 2009), p. 062706. DOI: 10.1103/PhysRevA.79.062706. URL: https://link.aps.org/doi/10.1103/PhysRevA.79.062706 (cit. on p. 56).

[93] A. Deller, M. H. Rayment, and S. D. Hogan. “Slow Decay Processes of Electrostatically Trapped Rydberg NO Molecules”. In: *Phys. Rev. Lett.* 125 (7 Aug. 2020), p. 073201. DOI: 10.1103/PhysRevLett.125.073201. URL: https://link.aps.org/doi/10.1103/PhysRevLett.125.073201 (cit. on p. 56).

[94] R. Wang et al. “Radio frequency field-induced electron mobility in an ultracold plasma state of arrested relaxation”. In: *Phys. Rev. A* 102 (6 Dec. 2020), p. 063122. DOI: 10.1103/PhysRevA.102.063122. URL: https://link.aps.org/doi/10.1103/PhysRevA.102.063122 (cit. on p. 56).

[95] M. H. Rayment and S. D. Hogan. “Quantum-state-dependent decay rates of electrostatically trapped Rydberg NO molecules”. In: *Phys. Chem. Chem. Phys.* 23 (34 2021), pp. 18806–18822. DOI: 10.1039/D1CP01930A. URL: http://dx.doi.org/10.1039/D1CP01930A (cit. on p. 56).

[96] P. Zorabedian. “Tunable external-cavity semiconductor lasers”. In: F. J. Duarte. *Tunable lasers handbook*. Ed. by D. F. J. Academic Press, 1995. Chap. 8, pp. 349–442. ISBN: 012222695X (cit. on p. 57).

[97] F. J. Duarte. *Tunable lasers handbook*. Ed. by F. J. Duarte. Academic Press, 1995, p. 476. ISBN: 012222695X (cit. on p. 57).

[98] A. Bisquerra. *Setup and Characterisation of a Frequency-Doubled Lasersystem for Spectroscopy of the* $\mathrm{A}\,^2\Sigma^+$ *to* $\mathrm{H}\,^2\Sigma^+$ *Transition in Nitric Oxide*. Bachelor thesis. Oct. 2019 (cit. on p. 58).

[99] R. W. Boyd. *Nonlinear optics*. 3rd ed. Academic Press, 2008, p. 613. ISBN: 9780123694706 (cit. on p. 58).

[100] G. D. Boyd and D. A. Kleinman. “Parametric Interaction of Focused Gaussian Light Beams”. In: *Journal of Applied Physics* 39.8 (July 1968), pp. 3597–3639. DOI: 10.1063/1.1656831. eprint: https://doi.org/10.1063/1.1656831. URL: https://doi.org/10.1063/1.1656831 (cit. on p. 58).

[101] N. Šibalić et al. “ARC: An open-source library for calculating properties of alkali Rydberg atoms”. In: *Computer Physics Communications* 220 (2017), pp. 319–331. ISSN: 0010-4655. DOI: https://doi.org/10.1016/j.cpc.2017.06.015. URL: https://www.sciencedirect.com/science/article/pii/S0010465517301972 (cit. on p. 59).

[102] M. Ilewicz. *Setup of a laser system fo the excitation of nitric oxide from the* H $^2\Sigma^+$, H′ $^2\Pi$ *state to Rydberg states*. Bachelor thesis. Mar. 2020 (cit. on p. 60).

[103] J. C. B. Kangara et al. “Design and construction of cost-effective tapered amplifier systems for laser cooling and trapping experiments”. In: *American Journal of Physics* 82.8 (2014), pp. 805–817. DOI: 10.1119/1.4867376. eprint: https://doi.org/10.1119/1.4867376. URL: https://doi.org/10.1119/1.4867376 (cit. on p. 60).

[104] R. V. Pound. “Electronic Frequency Stabilization of Microwave Oscillators”. In: *Review of Scientific Instruments* 17.11 (1946), pp. 490–505. DOI: 10.1063/1.1770414. eprint: https://doi.org/10.1063/1.1770414. URL: https://doi.org/10.1063/1.1770414 (cit. on p. 61).

[105] R. W. P. Drever et al. “Laser phase and frequency stabilization using an optical resonator”. In: *Applied Physics B Photophysics and Laser Chemistry* 31.2 (June 1983), pp. 97–105. DOI: 10.1007/bf00702605. URL: https://doi.org/10.1007/BF00702605 (cit. on p. 61).

[106] G. C. Bjorklund. “Frequency-modulation spectroscopy: a new method for measuring weak absorptions and dispersions”. In: *Opt. Lett.* 5.1 (Jan. 1980), pp. 15–17. DOI: 10.1364/OL.5.000015. URL: http://opg.optica.org/ol/abstract.cfm?URI=ol-5-1-15 (cit. on p. 61).

[107] G. C. Bjorklund et al. “Frequency modulation (FM) spectroscopy”. In: *Applied Physics B Photophysics and Laser Chemistry* 32.3 (Nov. 1983), pp. 145–152. DOI: 10.1007/BF00688820. URL: https://doi.org/10.1007/BF00688820 (cit. on p. 61).

[108] E. D. Black. "An introduction to Pound–Drever–Hall laser frequency stabilization". In: *American Journal of Physics* 69.1 (2001), pp. 79–87. DOI: 10.1119/1.1286663. eprint: https://doi.org/10.1119/1.1286663. URL: https://doi.org/10.1119/1.1286663 (cit. on pp. 61, 62).

[109] C. Tomschitz. "A photoionization scheme to create cold ionic impurities from Rydberg atoms". MA thesis. Universität Stuttgart, Oct. 2018. URL: https://www.pi5.uni-stuttgart.de/documents/abgeschlossene-arbeiten/2018-Tomschitz-Christian-A-photoionization-scheme-to-create-cold-ionic-impurities-from-Rydberg-atoms-MSC.pdf (cit. on p. 64).

[110] F. Moumtsilis. *Aufbau und Charakterisierung eines Fabry-Pérot-Interferometers zur Frequenzstabilisierung von Rydberg Lasern*. Bachelor Thesis. Nov. 2018 (cit. on p. 64).

[111] M. Seltenreich. *Eigenschaften eines digitalen, vielseitigen und erweiterbaren Systems zur Laserfrequenzstabilisierung*. Bachelor thesis. July 2021 (cit. on p. 65).

[112] T. Risby and S. Solga. "Current status of clinical breath analysis". In: *Applied Physics B* 85.2-3 (May 2006), pp. 421–426. DOI: 10.1007/s00340-006-2280-4. URL: https://doi.org/10.1007/s00340-006-2280-4 (cit. on p. 69).

[113] W. Demtröder. *Experimentalphysik 1*. Springer Berlin Heidelberg, July 2021. ISBN: 978-3-662-62728-0. URL: https://www.ebook.de/de/product/41288492/wolfgang_demtroeder_experimentalphysik_1.html (cit. on pp. 70–72, 76).

[114] M. Kaushik. *Fundamentals of Gas Dynamics*. Springer Nature Singapore, Mar. 2022. 583 pp. ISBN: 978-981-16-9085-3. URL: https://www.ebook.de/de/product/42291836/mrinal_kaushik_fundamentals_of_gas_dynamics.html (cit. on p. 71).

[115] K. Jousten, ed. *Handbuch Vakuumtechnik*. Gabler, Betriebswirt.-Vlg, Nov. 2018. 1129 pp. ISBN: 9783658133863. URL: https://www.ebook.de/de/product/34871827/handbuch_vakuumtechnik.html (cit. on pp. 72–75, 79).

[116] D. Hänel. *Molekulare Gasdynamik*. Springer Berlin Heidelberg, Apr. 2004. 236 pp. ISBN: 3540442472. URL: https://www.ebook.de/de/product/2181461/dieter_haenel_molekulare_gasdynamik.html (cit. on p. 74).

[117] H. Gobrecht. *Mechanik, Akustik, Wärme*. 9. verbesserte Auflage. De Gruyter, Apr. 1975. 872 pp. ISBN: 3110048612. URL: https://www.ebook.de/de/product/17406943/heinrich_gobrecht_mechanik_akustik_waerme.html (cit. on p. 76).

[118] C. E. Mortimer and U. Müller. *Chemie das Basiswissen der Chemie. das Basiswissen der Chemie*. Thieme, 2007. ISBN: 9783134843095 (cit. on p. 77).

[119] P. Morrow. "An evaluation of recent NOx toxicity data and an attempt to derive an ambient air standard for NOx by established toxicological procedures". In: *Environmental Research* 10.1 (1975), pp. 92–112. ISSN: 0013-9351. DOI: https://doi.org/10.1016/0013-9351(75)90076-6. URL: https://www.sciencedirect.com/science/article/pii/0013935175900766 (cit. on p. 77).

[120] *Beständigkeitstabelle - Bürkert Fluid Control Systems*. Retrieved 17th October 2022. Bürkert Fluid Control Systems. Christian-Bürkert Straße, Jan. 2019. URL: https://www.buerkert.de/de/content/download/9318/335016/file/Chemische-Bestaendigkeitstabelle.pdf?id=49 (cit. on p. 77).

[121] L. Rubino. *Setup and characterisation of a gas mixing unit for the dilution of* CO_2 *with* N_2. Bachelor Thesis. Nov. 2020 (cit. on p. 83).

[122] R. Eisenberg and C. D. Meyer. "Coordination chemistry of nitric oxide". In: *Accounts of Chemical Research* 8.1 (Jan. 1975), pp. 26–34. DOI: 10.1021/ar50085a004 (cit. on p. 83).

[123] J. A. McCleverty. "Reactions of nitric oxide coordinated to transition metals". In: *Chemical Reviews* 79.1 (Feb. 1979), pp. 53–76. DOI: 10.1021/cr60317a005 (cit. on p. 83).

[124] P. C. Ford and I. M. Lorkovic. "Mechanistic Aspects of the Reactions of Nitric Oxide with Transition-Metal Complexes". In: *Chemical Reviews* 102.4 (Mar. 2002), pp. 993–1018. DOI: 10.1021/cr0000271 (cit. on p. 83).

[125] W. A. Brown and D. A. King. "NO Chemisorption and Reactions on Metal Surfaces: A New Perspective". In: *The Journal of Physical Chemistry B* 104.12 (Feb. 2000), pp. 2578–2595. DOI: 10.1021/jp9930907 (cit. on p. 83).

[126] C. England and W. H. Corcoran. “Kinetics and Mechanisms of the Gas-Phase Reaction of Water Vapor and Nitrogen Dioxide”. In: *Ind. Eng. Chem. Fund.* 13.4 (Jan. 1974), pp. 373–384. DOI: 10.1021/i160052a014. URL: https://doi.org/10.1021/i160052a014 (cit. on p. 86).

[127] K. Langeheinecke. *Thermodynamik für Ingenieure*. 8th ed. Vieweg+Teubner, 2008. ISBN: 9783834804181 (cit. on p. 89).

[128] T. Ebata et al. “High Rydberg states of nitric oxide studied by two-color multiphoton spectroscopy”. In: *The Journal of Physical Chemistry* 87.24 (Nov. 1983), pp. 4773–4776. DOI: 10.1021/j150642a001 (cit. on p. 91).

[129] A. Deller and S. D. Hogan. “Excitation and characterization of long-lived hydrogenic Rydberg states of nitric oxide”. In: *The Journal of Chemical Physics* 152.14 (2020), p. 144305. DOI: 10.1063/5.0003092. eprint: https://doi.org/10.1063/5.0003092. URL: https://doi.org/10.1063/5.0003092 (cit. on p. 91).

[130] Y. Schellander. *Laserstabilisierung für ein Quantengasexperiment*. Bachelor Thesis. Sept. 2018. URL: https://www.pi5.uni-stuttgart.de/documents/abgeschlossene-arbeiten/2018-Schellander-Yannick-Laserstabilisierung-fuer-ein-Quantengasexperiment-BSC.pdf (cit. on pp. 94, 100).

[131] D. Djekic et al. “A 440-kOhm to 150-GOhm Tunable Transimpedance Amplifier based on Multi-Element Pseudo-Resistors”. In: *ESSCIRC 2021 - IEEE 47th European Solid State Circuits Conference (ESSCIRC)*. 2021, pp. 403–406. DOI: 10.1109/ESSCIRC53450.2021.9567831 (cit. on p. 97).

[132] R. Beringer, E. B. Rawson, and A. F. Henry. “Microwave Resonance in Nitric Oxide: Lambda Doubling and Hyperfine Structure”. In: *Phys. Rev.* 94 (2 Apr. 1954), pp. 343–349. DOI: 10.1103/PhysRev.94.343. URL: https://link.aps.org/doi/10.1103/PhysRev.94.343 (cit. on p. 99).

[133] J. J. Gallagher and C. M. Johnson. “Uncoupling Effects in the Microwave Spectrum of Nitric Oxide”. In: *Phys. Rev.* 103 (6 Sept. 1956), pp. 1727–1737. DOI: 10.1103/PhysRev.103.1727. URL: https://link.aps.org/doi/10.1103/PhysRev.103.1727 (cit. on p. 99).

[134] R. L. Brown and H. E. Radford. “*L*-Uncoupling Effects on the Electron-Paramagnetic-Resonance Spectra of $N^{14}O^{16}$ and $N^{15}O^{16}$”. In: *Phys. Rev.* 147 (1 July 1966), pp. 6–12. DOI: 10.1103/PhysRev.147.6. URL: https://link.aps.org/doi/10.1103/PhysRev.147.6 (cit. on p. 99).

[135] W. Meerts and A. Dymanus. “The hyperfine Λ-doubling spectrum of 14N16O and 15N16O”. In: *Journal of Molecular Spectroscopy* 44.2 (1972), pp. 320–346. ISSN: 0022-2852. DOI: https://doi.org/10.1016/0022-2852(72)90109-9. URL: https://www.sciencedirect.com/science/article/pii/0022285272901099 (cit. on p. 99).

[136] J. A. Gray et al. “The electric dipole moment of NO A 2Σ+ v’=0 measured using Stark quantum-beat spectroscopy”. In: *The Journal of Chemical Physics* 99.6 (1993), pp. 4327–4333. DOI: 10.1063/1.466086. eprint: https://doi.org/10.1063/1.466086. URL: https://doi.org/10.1063/1.466086 (cit. on pp. 99, 121).

[137] L. Ebel. *Determination of the Energy Structure of Nitric Oxide using an Effective Hailtonian Approach*. Bachelor Thesis. Aug. 2021 (cit. on pp. 99, 102, 107).

[138] D. P. Blair and P. H. Sydenham. “Phase sensitive detection as a means to recover signals buried in noise”. In: *Journal of Physics E: Scientific Instruments* 8.8 (Aug. 1975), pp. 621–627. DOI: 10.1088/0022-3735/8/8/001 (cit. on p. 102).

[139] P. Horowitz and W. Hill. *The art of electronics*. Cambridge University Press, 2015, p. 1224. ISBN: 9780521809269 (cit. on p. 102).

[140] P. A. Temple. “An introduction to phase-sensitive amplifiers: An inexpensive student instrument”. In: *American Journal of Physics* 43.9 (1975), pp. 801–807. DOI: 10.1119/1.9690. eprint: https://doi.org/10.1119/1.9690. URL: https://doi.org/10.1119/1.9690 (cit. on p. 102).

[141] A. B. Callear and I. W. M. Smith. “Fluorescence of nitric oxide. Part 1.—Determination of the mean lifetime of the A2Σ+ state”. In: *Trans. Faraday Soc.* 59 (0 1963), pp. 1720–1734. DOI: 10.1039/TF9635901720. URL: http://dx.doi.org/10.1039/TF9635901720 (cit. on p. 104).

[142] L. G. Piper and L. M. Cowles. “Einstein coefficients and transition moment variation for the NO(A 2Σ+–X 2Π) transition”. In: *The Journal of Chemical Physics* 85.5 (1986), pp. 2419–2422. DOI: 10.1063/1.451098. eprint: https://doi.org/10.1063/1.451098. URL: https://doi.org/10.1063/1.451098 (cit. on p. 104).

[143] R. de Vivie and S. D. Peyerimhoff. “Theoretical spectroscopy of the NO radical. I. Potential curves and lifetimes of excited states”. In: *The Journal of Chemical Physics* 89.5 (1988), pp. 3028–3043. DOI: 10.1063/1.454958. eprint: https://doi.org/10.1063/1.454958. URL: https://doi.org/10.1063/1.454958 (cit. on p. 104).

[144] J. Luque and D. R. Crosley. “Transition probabilities and electronic transition moments of the A 2Σ+–X 2Π and D 2Σ+–X 2Π systems of nitric oxide”. In: *The Journal of Chemical Physics* 111.16 (1999), pp. 7405–7415. DOI: 10.1063/1.480064. eprint: https://doi.org/10.1063/1.480064. URL: https://doi.org/10.1063/1.480064 (cit. on p. 104).

[145] C. M. Western. “PGOPHER: A program for simulating rotational, vibrational and electronic spectra”. In: *Journal of Quantitative Spectroscopy and Radiative Transfer* 186 (2017). Satellite Remote Sensing and Spectroscopy: Joint ACE-Odin Meeting, October 2015, pp. 221–242. ISSN: 0022-4073. DOI: https://doi.org/10.1016/j.jqsrt.2016.04.010. URL: https://www.sciencedirect.com/science/article/pii/S0022407316300437 (cit. on p. 116).

[146] W. Voigt. *Über das Gesetz der Intensitätsverteilung innerhalb der Linien eines Gasspektrums*. München, 1912. URL: https://publikationen.badw.de/de/003395768 (cit. on p. 118).

[147] S. P. Walch and W. A. Goddard. “Dipole moments and electric field gradients for correlated wavefunctions of NO: The X 2Π, A 2Σ+, and D 2Σ+ states”. In: *Chemical Physics Letters* 33 (1975), pp. 18–24. DOI: https://doi.org/10.1016/0009-2614(75)85444-3. URL: https://www.sciencedirect.com/science/article/pii/0009261475854443 (cit. on p. 121).

[148] S. Green. “Calculated properties for no X2Π and A2Σ+”. In: *Chemical Physics Letters* 13.6 (1972), pp. 552–556. ISSN: 0009-2614. DOI: https://doi.org/10.1016/0009-2614(72)85009-7. URL: https://www.sciencedirect.com/science/article/pii/0009261472850097 (cit. on p. 121).

[149] S. Green. “Calculated properties for No X2 Π and A 2Σ+. II. Configuration interaction”. In: *Chemical Physics Letters* 23.1 (1973), pp. 115–119. ISSN: 0009-2614. DOI: https://doi.org/10.1016/0009-2614(73)89577-6. URL: https://www.sciencedirect.com/science/article/pii/0009261473895776 (cit. on p. 121).

[150] W. H. PRESS. *Numerical recipes the art of scientific computing*. Cambridge University Press, 2007, p. 1235. ISBN: 9780511335556 (cit. on p. 127).

[151] L.-G. Tao et al. “Toward a Determination of the Proton-Electron Mass Ratio from the Lamb-Dip Measurement of HD”. In: *Phys. Rev. Lett.* 120 (15 Apr. 2018), p. 153001. DOI: 10.1103/PhysRevLett.120.153001. URL: https://link.aps.org/doi/10.1103/PhysRevLett.120.153001 (cit. on p. 131).

[152] M. L. Diouf et al. “Lamb-dips and Lamb-peaks in the saturation spectrum of HD”. In: *Optics Letters* 44.19 (Sept. 2019), p. 4733. DOI: 10.1364/ol.44.004733 (cit. on p. 131).

[153] R. González-Férez, J. Shertzer, and H. R. Sadeghpour. “Ultralong-Range Rydberg Bimolecules”. In: *Phys. Rev. Lett.* 126 (4 Jan. 2021), p. 043401. DOI: 10.1103/PhysRevLett.126.043401. URL: https://link.aps.org/doi/10.1103/PhysRevLett.126.043401 (cit. on p. 132).

Appendix

A: Vibrational constants for the ground state of nitric oxide

Table A.1: Equilibrium vibrational constants in cm^{-1} for the ground state of nitric oxide $\mathrm{X}\,^2\Pi$ [28]

Constant	Value
ω_e	1904.085(15)
$\omega_e x_e$	14.066(51)
$\omega_e y_e$	$0.619(48) \times 10^{-2}$

B: Molecular term symbols

The notation of molecular term symbols may confuse someone new to the field of molecular physics. Therefore, they are briefly explained here.

Molecular term symbols are usually of the form [40]

$$\mathrm{X}\,^{2S+1}\Lambda^{+/-}_{\Omega/\mathrm{g,u}}. \tag{B.1}$$

The meaning of the individual signs of the term symbol are:

- X: The letter up in front in the term symbol denotes the electronic state. The ground state is always denoted as X. Then all states are labelled alphabetical, i.e. the energetically lowest excited state is denoted A, the next higher B and so on. Exceptions occur due to historic reasons: assume that the molecular states A and B are already labelled and somebody discovers a molecular state which is energetically between A and B. It would be extremely inconvenient to rename all of the already known states. Therefore, that intermediate state is then labelled with a prime. Thus, in the example it would be labelled A'.
- S: total spin of the electron. The term $2S + 1$ is named multiplicity like in atomic physics.
- Λ: The projection of the total electron orbital momentum L on the nuclear axis is denoted Λ and added to the term symbol by capital greek letters. This means $\Lambda = 0, 1, 2, ...$ corresponds to $\Sigma, \Pi, \Delta, ...$ This is analogue to the naming scheme for atoms were the l-character is denoted with letters of the latin alphabet.
- $^{+/-}$: The exponent of Λ is giving the overall parity of the molecular state. It is often neglected.
- Ω: If the state is spin-orbit split the subscript Ω gives the value the of quantum number $\Omega = \Lambda + \Sigma$, which gives the total projection of the electronic angular momentum on the internuclear axis. Since Ω is only defined in Hund's case (a), it will usually not be given if the described state belongs to a different Hund's case.
- g, u: The label g for *gerade* (even) and the label u for *ungerade* (odd) denotes the symmetry of the total wave-function with reference to molecule fixed coordinates.

C: Molecular constants for nitric oxide

C.1: X $^2\Pi$

Table C.1.1: List of finestructure constants for the groundstate X $^2\Pi$ of nitric oxide. All values in MHz.

Constant	Value	Reference
B	50 848.130 72(18)	Varberg et al. [35]
D	0.164 141 19(31)	.
H	3.774(15) $\times 10^{-8}$	.
A	3 691 813.855(12)	Varberg et al. [35]
A_D	5.372(38)	Danielak et al. [28]
γ	-193.987 9(77)	Varberg et al. [35]
γ_D	0.001 582 2(70)	.
p	350.405 443(91)	.
p_D	3.78(18) $\times 10^{-5}$	.
q	2.822 100(51)	.
q_D	4.370(38) $\times 10^{-5}$	.
q_H	-8.6(25) $\times 10^{-10}$	Varberg et al. [35]

Table C.1.2: List of hyperfine constants for the groundstate X $^2\Pi$ of nitric oxide. All values in MHz.

Constant	Value	Reference
a	84.203 78(76)	Varberg et al. [35]
b_F	22.379 2(28)	.
b	42.006 5(38)	.
c	-58.882 0(32)	.
d	112.597 18(13)	.
d_D	1.10(23) $\times 10^{-4}$	Varberg et al. [35]
t_0	-19.627 3	Brown and Carrington [45]
t_2	75.064 79	Brown and Carrington [45]
C_I	0.012347(52)	Varberg et al. [35]
C_I'	0.007 37(36)	.
eQq_0	-1.856 71(26)	.
eQq_2	23.114 7(83)	Varberg et al. [35]

C.2: A $^2\Sigma^+$

Table C.2: List of constants for the A $^2\Sigma^+$ state of nitric oxide. All values in MHz.

Constant	Value	Reference
$T_0^A - T_0^X$	1 323 308 163(60)	Danielak et al. [28]
B	59 545.297(239)	[28, 36]
D	0.169572(236)	[28, 36]
γ	-80.34(16)	[28, 36]
b_F	43.52(30)	Brouard et al. [36]
b	41.66(51)	.
c	5.59(64)	.
eQq_0	-7.31(23)	Brouard et al. [36]

C.3: H $^2\Sigma^+$, H′ $^2\Pi$ and F $^2\Delta$ state and interaction parameters within the 3d-Rydberg complex

Table C.3.1: List of constants for the H $^2\Sigma^+$ state of nitric oxide. All values in MHz.

Constant	Value	Reference
$T_{\mathrm{H}} = T_0^H - T_0^X$	1 879 856 313(180)	Bernard et al. [77]
B_{H}	59 672.6(16)	.
D_{H}	0.189 4(36)	Bernard et al. [77]

Table C.3.2: List of constants for the H′ $^2\Pi$ state of nitric oxide. All values in MHz.

Constant	Value	Reference
$T_{\mathrm{H}'} = T_0^{H'} - T_0^X$	1 880 271 855(120)	Bernard et al. [77]
$A_{\mathrm{H}'}$	43 230(300)	.
$B_{\mathrm{H}'}$	59 254.88(420)	.
$D_{\mathrm{H}'}$	0.185 3(30)	Bernard et al. [77]

Table C.3.3: List of constants for the F $^2\Delta$ state of nitric oxide. All values in MHz.

Constant	Value	Reference
$T_\mathrm{F} = T_0^F - T_0^X$	1 860 139 712(300)	Bernard et al. [77]
A_F	-1 259(120)	.
B_F	59 834.37(450)	.
D_F	0.121(10)	Bernard et al. [77]

Table C.3.4: List of interaction parameters within the 3d-Rydberg complex (v=0). Values in MHz

Constant	Value	Reference
α	1 019(390)	Bernard et al. [77]
β	135 326(300)	.
ξ	27 823(39)	.
η	115 025(4)	Bernard et al. [77]

D: Viscosities of nitric oxide and nitrogen

Table D.1: Viscosities of NO and N_2 at $T = 300\,\mathrm{K}$ in µPa s [66]

Gas	Viscosity
NO	19.2
N_2	17.9